

**A STUDY OF AERODYNAMIC DEAGGREGATION
MECHANISMS AND THE SIZE CONTROL OF
NANOACTIVE™ AEROSOL PARTICLES**

by

JOSHUA ALLEN HUBBARD

B.S., Kansas State University, 2005

A THESIS

submitted in partial fulfillment of the requirements for the degree

MASTER OF SCIENCE

Department of Mechanical and Nuclear Engineering

College of Engineering

KANSAS STATE UNIVERSITY

Manhattan, Kansas

2006

Approved by:

Co-Major Professor

Dr. Steven J. Eckels

Co-Major Professor

Dr. Christopher M. Sorensen

ABSTRACT

Large specific surface areas and high concentrations of reactive edge and defect sites make NanoActive™ metal oxide powders ideal chemical adsorbents. These powders are dispersed in aerosol form to remediate toxic wastes and neutralize chemical and biological warfare agents.

In the destructive adsorption of toxic chemicals, effective application requires particles be as small as possible, thus, maximizing surface area and number of edge and defect sites. Other applications, e.g. smoke clearing, require particles be large so they will settle in a timely manner. Ideally, particle size control could be engineered into powder dispersion devices. The purpose of this study was to explore particle cohesion and aerodynamic deaggregation mechanisms to enhance the design of powder dispersion devices.

An aerosol generator and four experimental nozzles were designed to explore the most commonly referenced deaggregation mechanisms: particle acceleration, particles in shear and turbulent flows, and particle impaction. The powders were then dispersed through the nozzles with increasing flow rates. A small angle light scattering device was used to make in situ particle size measurements. The nozzle designed for impaction deaggregated the NanoActive™ MgO particles to a lesser degree than the other three nozzles, which deaggregated the particles to a similar degree.

Flows in three of the four nozzles were simulated in a commercial computational fluid dynamics package. Theoretical particle and aggregate stresses from the literature were

calculated using simulated data. These calculations suggest particle acceleration causes internal stresses roughly three orders of magnitude larger than shear and turbulent flows. These calculations, coupled with experimental data, lead to the conclusion that acceleration was the most significant cause of particle deaggregation in these experiments.

Experimental data also identified the dependence of deaggregation on primary particle size and agglomerate structure. NanoActive™ powders with smaller primary particles exhibited higher resistance to deaggregation. Small primary particle size was thought to increase the magnitude of van der Waals interactions. These interactions were modeled and compared to theoretical deaggregation stresses previously mentioned.

In conclusion, deaggregation is possible. However, the ideas of particle size control and a universal dispersion device seem elusive considering the material dependent nature of deaggregation.

TABLE OF CONTENTS

LIST OF FIGURES	x
LIST OF TABLES	xiv
ACKNOWLEDGMENTS	xv
DEDICATION	xvi
1 INTRODUCTION	1
2 MATERIALS.....	3
2.1 Magnesium Oxide.....	3
2.1.1 Commercially Prepared MgO.....	3
2.1.2 NanoActive™ MgO.....	3
2.1.3 NanoActive™ MgO Plus.....	3
2.1.4 Comparison of NanoActive™ MgO and MgO Plus.....	5
2.2 TSI Hollow Glass Spheres.....	6
2.3 Arizona Road Dust.....	7
2.4 Fire Extinguisher Grade Sodium Bicarbonate	8
2.5 Transmission Electron Microscopy	8
2.5.1 TEM Laboratory	8
2.5.2 Sample Preparation	8
2.5.3 NanoActive™ MgO.....	9
2.5.4 NanoActive™ MgO Plus	10
2.5.5 TSI Hollow Glass Spheres.....	10
2.5.6 Arizona Road Dust.....	11
2.5.7 Sodium Bicarbonate.....	12
3 ADHESION AND COHESION REVIEW.....	13
3.1 Introduction.....	13
3.2 Interparticle Forces	13
3.2.1 van der Waals Forces	13
3.2.2 Electrostatic Forces.....	14
3.2.3 Capillary Forces	16

3.2.4	Comparison of Interparticle Forces	16
3.2.5	Measurement of Adhesive Forces.....	17
3.3	Intermolecular and Surface Forces	17
3.3.1	Energy of Interaction for an Atom and an Infinite Planar Surface	18
3.3.2	Energy of Interaction for a Sphere and an Infinite Surface	19
3.3.3	Energy of Interaction of a Plane of Unit Area and an Infinite Plane	20
3.3.4	Conclusions from Energies of Interactions.....	20
3.3.5	Derjaguin Approximation	21
4	DEAGGREGATION REVIEW	22
4.1	Introduction.....	22
4.2	Stresses in a Single Spherical Particle in Viscous Flow	22
4.3	Fundamental Work on Particle Deaggregation.....	23
4.3.1	Stress Induced in a Spherical Particle Due to Impact	23
4.3.2	Stresses Induced in Aggregates in Uniform Flow	23
4.3.3	Stresses Induced in Aggregates in Simple Shear Flow.....	25
4.3.4	Stresses Induced in a Single Spherical Particle in Turbulent Flow	25
4.3.5	Experimental Validation of Deaggregation Theory.....	26
4.3.6	Conclusions from Fundamental Work on Deaggregation	28
4.4	Recent Experimental Studies on Particle Deaggregation	28
4.4.1	Shear Experiments	29
4.4.2	Impaction Experiments	30
4.4.3	Turbulence Experiments	32
4.4.4	Conclusions Drawn from Experimental Work	33
5	AEROSOL GENERATOR AND NOZZLE DESIGN	35
5.1	Introduction.....	35
5.2	Powder Dispersion Devices	35
5.3	Aerosol Generator.....	36
5.3.1	Air Inlet Tube.....	37
5.3.2	Mechanical Agitation.....	38
5.3.3	Deaggregation	38
5.4	Deaggregation Nozzles	39

5.4.1	Abrupt Orifice.....	39
5.4.2	Converging-Diverging Nozzle.....	39
5.4.3	Converging Nozzle	40
5.4.4	Mesh Nozzle	40
5.5	Evaluating the Electrostatic Effects of Mechanical Agitation.....	41
5.5.1	Experimental Setup.....	42
5.5.2	Charge-to-Mass Ratio Data.....	45
5.5.3	Conclusion	47
6	PARTICLE IMAGE VELOCIMETRY	49
6.1	Introduction.....	49
6.1.1	Seeding the Flow.....	49
6.1.2	Illuminating the Seed Particles	50
6.1.3	Imaging the Seed Particles.....	50
6.1.4	Post Processing	50
6.2	Experimental Setup.....	51
6.2.1	Seed Particles	52
6.2.2	Imaging	52
6.2.3	Post Processing	52
6.3	Data.....	53
6.3.1	Velocity.....	53
6.3.2	Turbulent Kinetic Energy	54
6.3.3	Shear Stress.....	55
6.4	PIV Data Summary for Abrupt Orifice.....	56
7	CFD SIMULATIONS.....	57
7.1	Nozzle Model Data	57
7.2	Simulation Setup.....	58
7.2.1	Operating Conditions	58
7.2.2	Boundary Conditions	59
7.2.3	Initial Conditions	59
7.2.4	Convergence Criteria	59
7.2.5	Incompressible Flow.....	59

7.3	Simulation Model Data.....	60
7.3.1	Velocity.....	60
7.3.2	Verification.....	61
7.3.3	Acceleration.....	61
7.3.4	Scale Invariance.....	63
7.3.5	Shear Stress.....	63
7.3.6	Strain Rate.....	66
7.3.7	Turbulent Energy Dissipation Rate.....	66
7.4	Conclusions.....	67
8	LIGHT SCATTERING REVIEW.....	68
8.1	Review of Electromagnetic Waves.....	68
8.2	Light Scattering.....	68
8.2.1	Polarization.....	69
8.2.2	Relative Particle Size.....	70
8.3	Scattering Cross Section.....	70
8.3.1	Measurement of Particle Size.....	71
8.3.2	Differential Scattering Cross Section.....	72
8.3.3	Rayleigh Scattering.....	73
8.3.4	Rayleigh-Debye-Gans Scattering.....	74
8.3.5	Mie Scattering.....	74
8.3.6	Polydisperse and Nonspherical Scatterers.....	77
9	LIGHT SCATTERING EXPERIMENTAL SETUP.....	79
9.1	Equipment.....	79
9.2	Laboratory Setup.....	79
9.2.1	Light Scattering.....	79
9.2.2	Aerosol Generation.....	81
9.3	Calibration.....	84
10	LIGHT SCATTERING DATA.....	85
10.1	Data Normalization.....	85
10.2	Bimodal Modeling of Small Angle Light Scattering Data.....	86

10.3	Abrupt Orifice.....	89
10.3.1	NanoActive™ MgO.....	89
10.3.1.1	High Pressure Data	89
10.3.1.2	Low Pressure Data	90
10.3.2	NanoActive™ MgO Plus	93
10.3.3	TSI Hollow Glass Spheres	94
10.3.4	Arizona Road Dust.....	96
10.3.5	Sodium Bicarbonate.....	97
10.4	Converging-Diverging Nozzle.....	98
10.5	Converging Nozzle	100
10.6	Mesh Nozzle	102
10.7	Open Nipple	104
10.8	Light Scattering Contribution Analysis	105
11	DISCUSSION.....	108
11.1	Degrees of Polydispersity	108
11.2	Entrainment.....	108
11.3	Deaggregation due to Impaction.....	109
11.3.1	Other Research.....	109
11.3.2	Impaction Theory.....	110
11.3.3	Mesh Nozzle	110
11.3.4	Abrupt Orifice.....	112
11.4	Deaggregation Stresses within a Single Spherical Particle.....	115
11.4.1	Stresses within a Single Spherical Particle in Uniform Flow	116
11.4.2	Stresses within a Single Spherical Particle in Shear Flow.....	116
11.4.3	Stresses within a Single Spherical Particle in Accelerating Flow	117
11.4.4	Stresses within a Single Spherical Particle in Turbulent Flow	118
11.4.5	Comparison of Stresses within a Single Spherical Particle	118
11.5	Deaggregation Stresses in an Aggregate.....	119
11.5.1	Stresses within an Aggregate in Uniform Flow	119
11.5.2	Stresses within an Aggregate in Shear Flow.....	121
11.5.3	Comparison of Stresses in an Aggregate	121

11.6	Surface Interaction Energies and Forces.....	122
11.6.1	Calculation of London Dispersion Coefficient.....	122
11.6.2	Energy and Force Calculations	123
11.6.2.1	Spherical Particle Interacting with an Infinite Plane	123
11.6.2.2	Planar Area Interacting with an Infinite Plane.....	124
11.6.2.3	Derjaguin Approximation for Force Between Two Spheres	124
11.7	Comparison of Deaggregation and Cohesive Forces.....	124
11.8	Deaggregation as a Function of Particle Size and Structure.....	125
11.8.1	Deaggregation.....	126
11.8.2	Cohesion	127
12	CONCLUSION.....	129
	REFERENCES	133
APPENDIX A:	Aerosol Generator Drawings	137
APPENDIX B:	PIV Contour plots	141
APPENDIX C:	Theoretical Stress and Force Calculations.....	150

LIST OF FIGURES

Figure 2.1: High Resolution TEM image of NanoActive™ MgO Plus (Richards et al. 2000)	4
Figure 2.2: SEM Images of NanoActive™ MgO (Left) and MgO Plus (Right) (Utamapanya et al. 1991)	5
Figure 2.3: Size Distribution of Glass Spheres (Adapted from Velander 2005)	6
Figure 2.4: Arizona Road Dust Particle Size Distribution (Adapted from Powder Technology Inc. 2006)	7
Figure 2.5: TEM Images of NanoActive™ MgO Particles	9
Figure 2.6: TEM Images of NanoActive™ MgO Plus Particles	10
Figure 2.7: TEM Images of TSI Hollow Glass Spheres	11
Figure 2.8: TEM Images of Arizona Road Dust Particles	11
Figure 2.9: TEM Images of Sodium Bicarbonate Particles	12
Figure 4.1: Aggregate in Uniform Flow (Adapted from Kousaka et al. 1979)	23
Figure 4.2: Aggregate in Shear Flow (Adapted from Kousaka et al. 1979)	25
Figure 4.3: Aggregate in Turbulent Flow (Modified from Finlay 2001).....	33
Figure 5.1: Aerosol Generator	36
Figure 5.2: Aerosol Generator Air Inlet Tube	37
Figure 5.3: Aerosol Generator Aluminum Wipers	38
Figure 5.4: Converging-Diverging Nozzle	39
Figure 5.5: Converging Nozzle.....	40
Figure 5.6: Mesh Nozzle.....	41
Figure 5.7: Aerosol Generator Buildup (Without Mechanical Wipers)	42
Figure 5.8: Dynamic Faraday Cage Sampler Schematic (Taken from AML Handout).....	42
Figure 5.9: Dynamic Faraday Cage Sampler Components.....	43
Figure 5.10: Aerosol Sampling Chamber	43
Figure 5.11: Aerosol Generator and Pressure Control Apparatus	44
Figure 5.12: NanoActive™ MgO Charge vs. Time: Trial 1, Mixed	45
Figure 5.13: NanoActive™ MgO Charge vs. Time: Trial 2, Mixed	46
Figure 5.14: NanoActive™ MgO Charge vs. Time: Unmixed.....	47

Figure 6.1: PIV Schematic.....	49
Figure 6.2: Successive PIV Images	50
Figure 6.3: PIV Laboratory Setup.....	51
Figure 6.4: PIV Velocity Plot for Abrupt Orifice at 3.5 psi	53
Figure 6.5: PIV Turbulent Kinetic Energy Plot for Abrupt Orifice at 3.5 psi	54
Figure 6.6: Shear Stress for Abrupt Orifice at 3.5 psi	55
Figure 7.1: Model Geometries Created in Gambit.....	57
Figure 7.2: CFD Velocity Contour Plots	60
Figure 7.3: CFD Verification through Comparison with PIV Velocity.....	61
Figure 7.4: Acceleration Contour Plots	62
Figure 7.5: Shear Stress Contour Plots for Abrupt Orifice.....	64
Figure 7.6: Shear Stress Contour Plots for the Converging-Diverging Nozzle.....	65
Figure 7.7: Shear Stress Contour Plots for Converging Nozzle	65
Figure 7.8: Strain Rate Contour Plots.....	66
Figure 7.9: Turbulent Energy Dissipation Rate Contour Plots	67
Figure 8.1: EM Wave Diagram (Taken from Giancoli 1998)	68
Figure 8.2: Light Scattering Diagram	69
Figure 8.3: Scattering Cross Section Diagram.....	70
Figure 8.4: Scattering Cross Section in the Forward Direction.....	72
Figure 8.5: Patterns In Rayleigh, RDG, and Mie Scattering	75
Figure 9.1: Laser Schematic	80
Figure 9.2: Scattered Light Measurement Apparatus	80
Figure 9.3: Aerosol Generation Equipment Schematic	81
Figure 9.4: Position of Aerosol Generator.....	82
Figure 9.5: Picture of Experimental Setup.....	83
Figure 9.6: SALS Calibration Curve	84
Figure 10.1: NanoActive™ MgO SALS Data as a Function of Distance from the Orifice.....	85
Figure 10.2: Normalized NanoActive™ MgO SALS Data as a Function of Distance from the Orifice	86
Figure 10.3: Bimodal Modeling of NanoActive™ MgO SALS Data	87

Figure 10.4: NanoActive™ MgO SALS Data at Low Pressures for Abrupt Orifice.....	90
Figure 10.5: NanoActive™ MgO SALS Data for Abrupt Orifice.....	91
Figure 10.6: NanoActive™ MgO SALS Data for Abrupt Orifice Fitted with Bimodal Distribution.....	92
Figure 10.7: NanoActive™ MgO Plus SALS Data for Abrupt Orifice.....	93
Figure 10.8: TSI Hollow Glass Spheres Guinier Analysis for Abrupt Orifice.....	94
Figure 10.9: Glass Sphere Weighted Distribution to Reflect Scattering Intensity	95
Figure 10.10: Arizona Road Dust SALS Data for Abrupt Orifice	96
Figure 10.11: Sodium Bicarbonate SALS Data for Abrupt Orifice.....	97
Figure 10.12: NanoActive™ MgO SALS Data for Converging-diverging Nozzle.....	98
Figure 10.13: NanoActive™ MgO SALS Data for Converging-diverging Nozzle.....	99
Figure 10.14: NanoActive™ MgO SALS Data for Converging Nozzle	100
Figure 10.15: NanoActive™ MgO SALS for Converging Nozzle.....	101
Figure 10.16: NanoActive™ MgO SALS Data for Mesh Nozzle	102
Figure 10.17: NanoActive™ MgO SALS Data for Mesh Nozzle	103
Figure 10.18: NanoActive™ MgO SALS Data for Open Nipple.....	104
Figure 10.19: Scattering Contribution Analysis	107
Figure 11.1: Model of Compressible Flow in Abrupt Orifice Nozzle.....	113
Figure 11.2: Aggregate for which the Adhesion Constant is Unity.....	120
Figure 11.3: Spherical Particle Interacting with an Infinite Plane.....	123
Figure 11.4: Plane of Unit Area Interacting with an Infinite Plane.....	124
Figure A. 1: Aerosol Generator Assembly Drawing	137
Figure A. 2: Aerosol Generator Bearing Plate.....	138
Figure A. 3: Aerosol Generator Motor Plate	138
Figure A. 4: Aerosol Generator Orifice Plate	139
Figure A. 5: Aerosol Generator Leg Plate	139
Figure A. 6: Aerosol Generator Aluminum Tube.....	140

Figure A. 7: Aerosol Generator Propeller.....	140
Figure B. 1: PIV Velocity Plot for Abrupt Orifice 0.5 psi.....	141
Figure B. 2: PIV Velocity Plot for Abrupt Orifice 1.0 psi.....	141
Figure B. 3: PIV Velocity Plot for Abrupt Orifice 1.5 psi.....	142
Figure B. 4: PIV Velocity Plot for Abrupt Orifice 2.0 psi.....	142
Figure B. 5: PIV Velocity Plot for Abrupt Orifice 2.5 psi.....	143
Figure B. 6: PIV Velocity Plot for Abrupt Orifice 3.0 psi.....	143
Figure B. 7: PIV Shear Stress Plot for Abrupt Orifice 0.5 psi.....	144
Figure B. 8: PIV Shear Stress Plot for Abrupt Orifice 1.0 psi.....	144
Figure B. 9: PIV Shear Stress Plot for Abrupt Orifice 1.5 psi.....	145
Figure B. 10: PIV Shear Stress Plot for Abrupt Orifice 2.0 psi.....	145
Figure B. 11: PIV Shear Stress Plot for Abrupt Orifice 2.5 psi.....	146
Figure B. 12: PIV Shear Stress Plot for Abrupt Orifice 3.0 psi.....	146
Figure B. 13: PIV Turbulent Kinetic Energy Plot for Abrupt Orifice 0.5 psi	147
Figure B. 14: PIV Turbulent Kinetic Energy Plot for Abrupt Orifice 1.0 psi	147
Figure B. 15: PIV Turbulent Kinetic Energy Plot for Abrupt Orifice 1.5 psi	148
Figure B. 16: PIV Turbulent Kinetic Energy Plot for Abrupt Orifice 2.0 psi	148
Figure B. 17: PIV Turbulent Kinetic Energy Plot for Abrupt Orifice 2.5 psi	149
Figure B. 18: PIV Turbulent Kinetic Energy Plot for Abrupt Orifice 3.0 psi	149

LIST OF TABLES

Table 2.1: NanoActive™ MgO and MgO Plus Properties (Adapted from NanoScale Materials 2005)	5
Table 2.2: TSI Model 10089 Hollow Glass Spheres (Adapted from Velander 2005).....	6
Table 6.1: Summary of PIV Data for Abrupt Orifice	56
Table 7.1: Gambit Mesh Description.....	58
Table 7.2: Dependence of Velocity and Acceleration Based on Mesh Size.....	63
Table 9.1: Additional Experimental Settings.....	83
Table 10.1: Scattering Contribution Ratio	105
Table 11.1: Mid-Plane Stresses in a Single Spherical Particle in Uniform Flow	116
Table 11.2: Mid-Plane Stresses in a Single Spherical Particle in Shear Flow.....	117
Table 11.3: Mid-Plane Stress in a Single Spherical Particle due to Acceleration	117
Table 11.4: Mid-Plane Stresses in a Spherical Particle in Turbulent Flow	118
Table 11.5: Comparison of Stresses within a Single Spherical Particle	118
Table 11.6: Stresses within an Aggregate in Uniform Flow.....	120
Table 11.7: Bending Stress Produced in an Aggregate in Simple Shear Flow.....	121
Table 11.8: Comparison of Deaggregation Stresses in an Aggregate of Two Particles	121

ACKNOWLEDGMENTS

Most of all, I would like to thank my family for supporting my tireless efforts to get to this point of my academic career. Without their love and influence none of this would have been possible.

Secondly, I would like to thank Distinguished Professor Christopher Sorensen of the Physics Department and Professor Steven Eckels of the Mechanical Engineering Department. As my Co-Major Professors, they taught me to be a better scientist, researcher, and student. Their passion for science has encouraged me to pursue a career in teaching and research.

Distinguished Professor Christopher Sorensen's Graduate Research Group also deserves a great deal of thanks. Rajan Dhaubhadel, Tahereh Mokhtari, Matt Berg, and Flint Pierce adopted me as one of their own, sharing their laboratories and knowledge of light scattering. Their patience and technical support was always appreciated.

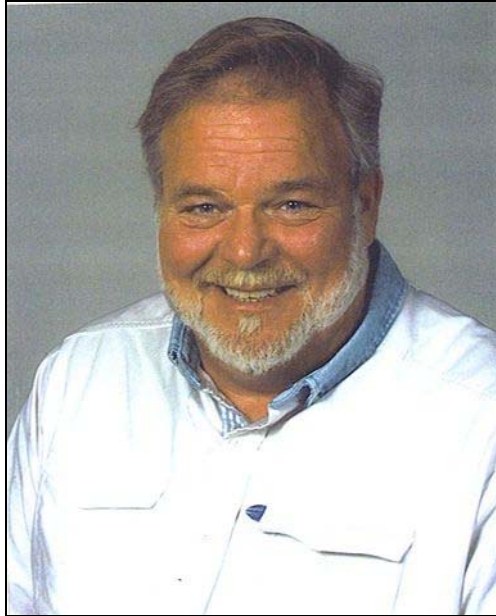
I would also like to express my gratitude to Dr. Steven O'Halloran of the Mechanical Engineering Department for introducing me to particle image velocimetry and computational fluid dynamics. Without his knowledge, time, and effort, I would not have been able to complete this thesis.

Susan Castro of the Biological and Agricultural Engineering Department also deserves special thanks for helping me with particle charge measurements.

Lastly, I would like to thank Professor Dan Boyle of the Biology Department for lending his expertise and performing all transmission electron microscopy utilized in this thesis.

DEDICATION

This thesis is dedicated to my late Father F. Allen Hubbard Jr. It was his knowledge and understanding of all things mechanical that inspired me to become an engineer. He cultivated my curiosities and always encouraged me to strive for my personal best.



1 INTRODUCTION

Past research efforts at Kansas State University have led to advanced chemical preparation methods that yield highly reactive metal oxide powders. These compounds are termed nanoscale materials because they are comprised of primary particles less than 400 nm in size. NanoScale Materials Incorporated, a company founded to commercially supply these materials, produces a wide variety of NanoActive™ metal oxides. The powders possess unique and unusual properties due to their nanocrystalline structures. The inherently large specific surface areas of these materials, along with high concentrations of reactive edge and corner defect sites, give them higher surface reactivity than normal polycrystalline materials. This makes them ideal chemical adsorbents.

NanoActive™ materials have highly effective chemical neutralization characteristics. The target adsorbate is irreversibly destroyed when it comes into contact with the material through a process called destructive chemisorption. Some of the following are applicable areas of interest for such materials: destruction of chemical warfare agents (VX, GD, and mustard gas), other acid gases and polar organic compounds, remediation of toxic waste, and smoke reduction in military applications.

Aerosolization of these powders allows for the reactions to occur throughout a large volume of gas. Dispersing the powders in an aerosol also allows for more effective chemical neutralization due to increased particle concentration which provides more locations for the chemical reactions to occur. The size of the particles is vital to effective neutralization and application. For instance, NanoActive™ MgO is used as a smoke clearant in various military applications. On a submarine, in the case of a fire, the smoke can be as detrimental as the fire itself. Dispersing the NanoActive™ MgO to clear the smoke from the air requires the particles be large enough for gravitational settling to occur. At the primary particle size, NanoActive™ MgO particles would react with, hence collect, the smoke particles and diffuse over long periods of time rather than settle out, thus making the NanoActive™ MgO ineffective. In this application it is crucial to

maintain some minimum particle size. On the other end of the spectrum, some applications are more aptly suited by the smallest of particles.

In the Spring of 1995, a domestic terrorist group in Japan deployed Sarin gas in multiple subway lines, killing twelve, and injuring nearly six thousand more. NanoActive™ MgO could have been deployed automatically, neutralizing the Sarin, reducing the number of casualties and injured. In this particular example, the time the NanoActive™ MgO aerosol remains airborne is of little importance. The critical occurrence is chemical neutralization which is facilitated by high number concentrations. High number concentration is analogous to complete breakdown of the NanoActive™ MgO powder into primary particles.

As the two preceding examples suggest, controlling the size of aerosol particles is essential to engineering their use in different applications. Ideally, one dispersion device with accurate size control could be developed for use in all applications. The purpose of this study is to explore particle cohesion and aerodynamic deaggregation mechanisms to enhance the design of powder dispersion devices.

The first few chapters of this thesis will be devoted to understanding what is already known about particle cohesive interactions and aerodynamic deaggregation mechanisms. These fundamentals will then be explored experimentally through the design of aerosol deaggregation nozzles, small angle light scattering, and computational fluid dynamics. Lastly, theoretical developments presented in past literature will be coupled with the experimental and simulated results from this study to draw conclusions about controlling aerosol particle size and designing aerosol dispersion devices.

2 MATERIALS

2.1 Magnesium Oxide

Magnesium Oxide is the metal oxide of interest in this study. There are three types of magnesium oxide commercially available: NanoScale Materials' NanoActive™ MgO and NanoActive™ MgO Plus, and what NanoScale terms commercially prepared MgO. The structure of these materials is crucial for understanding how they break apart when subjected to fluid dynamic forces.

2.1.1 Commercially Prepared MgO

Commercially prepared MgO refers to Magnesium Oxide powder that can be purchased through companies like Sigma-Aldrich. It has a cubic structure and a specific surface area in the range of 10 to 70 m²/g.

2.1.2 NanoActive™ MgO

NanoActive™ MgO is the trade name for one of the metal oxide powders produced by NanoScale Materials. It is also called Technical Grade MgO or Conventionally prepared MgO in chemistry literature, but will be referred to as NanoActive™ MgO from this point forward. To produce NanoActive™ MgO, commercially available MgO is boiled in water to make Mg(OH)₂. It is then dried at 120°C to get Mg(OH)₂ crystals. Finally, the crystals are heat treated at 500°C, under a vacuum, for 12 hours. The end result is NanoScale Materials' NanoActive™ MgO. The chemistry of NanoActive™ MgO is distinctly different from commercially prepared MgO. The primary particles in NanoActive™ MgO are platelets 100 to 400 nm in diameter and about 10 nm thick. These platelets come together to form loosely aggregated structures that will be shown in later sections. Some chemical and physical properties of NanoActive™ MgO are shown in Table 2.1.

2.1.3 NanoActive™ MgO Plus

It has been seen that less than 30% of NanoActive™ MgO reacts with various hazardous compounds (Mel'gunov 2003). Thus, production processes were developed to find more

efficient structures for destructive chemisorption reactions. Aerogel Preparation methods are used to manufacture NanoActive™ MgO Plus. Sometimes it is referred to as Premium Grade MgO or Aerogel Prepared MgO. It is known commercially as NanoActive™ MgO Plus and will be referred to as such from this point forward.

Aerogel Preparation begins with magnesium metal shavings reacting with methanol under argon gas. The solution is added drop wise to toluene and then water is added. The solution gels into $Mg(OH)_2$ and is heat treated in the same manner as NanoActive™ MgO to remove the H_2O and any residual organic impurities. The resulting powder is NanoActive™ MgO Plus and has a specific surface area greater than $600\text{ m}^2/\text{g}$. The reason for the significant increase in specific surface area is the decrease in primary particle size. The individual MgO crystallites are in the 3 to 5 nm range. Figure 2.1 is a high resolution TEM image showing the cube-like primary particles that form an aggregate. This image has essentially atomic resolution. The atomic lattice structure of the individual crystallites is apparent in the high resolution TEM image. The polyhedral crystallites possess numerous edge and corner sites. These sites are the most reactive and account for the significant adsorptive properties of NanoActive™ MgO Plus.

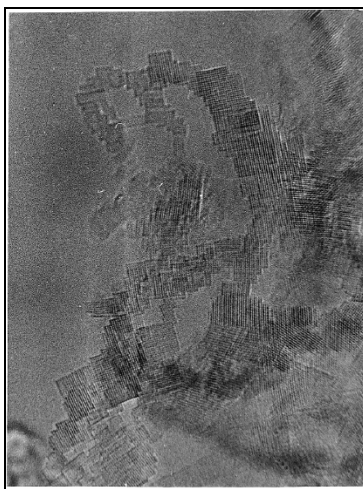


Figure 2.1: High Resolution TEM image of NanoActive™ MgO Plus (Richards et al. 2000)

These aggregates form agglomerates that are similar in structure to a cotton ball. The aggregates are analogous to the individual cotton fibers which are woven into a sphere-like structure which is called an agglomerate. Some chemical and physical properties of NanoActive™ MgO Plus are given in Table 2.1.

2.1.4 Comparison of NanoActive™ MgO and MgO Plus

Table 2.1 shows the chemical and physical properties of NanoActive™ MgO and MgO Plus. The specific surface area of NanoActive™ MgO is greater than 230 m²/g. This is a significant improvement from commercially prepared MgO and provides more area over which chemical reactions can occur. Furthermore, NanoActive™ MgO Plus has a specific surface area greater than 600 m²/g. This increase is due to the nanocrystalline structure created by the aerogel preparation process.

Table 2.1: NanoActive™ MgO and MgO Plus Properties (Adapted from NanoScale Materials 2005)

NanoScale Materials Inc. NanoActive™ MgO and MgO Plus		
Property	MgO	MgO Plus
Specific Surface Area - BET (m ² /g)	> 230	>600
Crystallite Size (nm)	<8	<4
Average Pore Diameter (Angstrom)	50	30
Total Pore Volume (cc/g)	>0.2	>0.4
Bulk Density (g/cc)	0.6	0.4
True Density (g/cc)	3.2	2.4
Mean Aggregate Size - d _{0.5} (micrometer)	3.3	12
Loss on Ignition (%)	<8	<15
Moisture Content (%)	<1	<3
Mg Content - Based on Metal (%)	>95	>99.2

Figure 2.2 shows SEM images of NanoActive™ MgO (left) and MgO Plus (Right). The platelet structure of NanoActive™ MgO can be seen comparative to the agglomerated “cotton ball-like” structure of NanoActive™ MgO Plus.

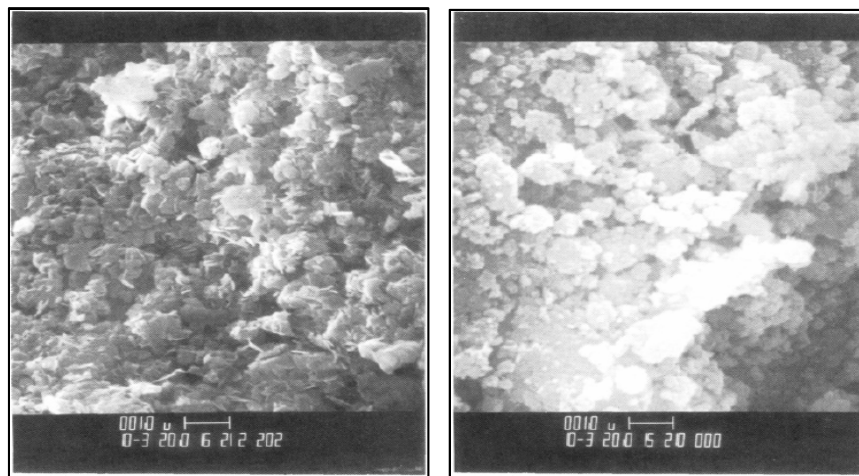


Figure 2.2: SEM Images of NanoActive™ MgO (Left) and MgO Plus (Right) (Utamapanya et al. 1991)

2.2 TSI Hollow Glass Spheres

TSI model 10089 Hollow Glass Spheres are used in this thesis, as well as many other aerosol measurement and sampling experiments, due to their relatively low cost, hollow spherical shape, i.e. neutral buoyancy in air, and low chemical reactivity. The glass spheres are polydisperse. Table 2.2 shows manufacturer data from a material data sheet for the hollow glass spheres.

Table 2.2: TSI Model 10089 Hollow Glass Spheres (Adapted from Velander 2005)

TSI Model 10089 Hollow Glass Spheres	
Manufacturer: Potter's Industries	
Nominal Mean Diameter (μm)	8 to 12
Density (g/cc)	1.05 to 1.15
Refractive Index	1.5
% less than 3-5 μm	10
% less than 14-17 μm	90

More detailed information was requested from the manufacturer regarding the size distribution. A TSI model 3063 particle size distribution analyzer was used by TSI to provide the number based size distribution shown in Figure 2.3. Two distinct modes can be seen in the sample of hollow glass spheres. The most common particle sizes are about 0.6 μm and 3 μm .

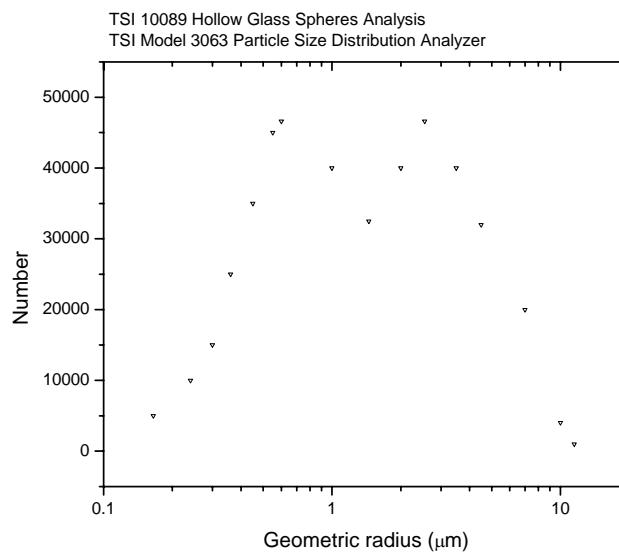


Figure 2.3: Size Distribution of Glass Spheres (Adapted from Velander 2005)

2.3 Arizona Road Dust

Arizona road dust is the common name for a set of powders originally used for testing filtration systems in automobiles. Initially, the dust was collected in Arizona along side the road, hence the name. The largest components of the dust are silicon and aluminum oxide.

Arizona Road Dust's industrial name is ISO 12103-1 Test Dust. This name refers to the standard established by the International Organization for Standardization for automotive filter testing. It will be referred to as Arizona Road Dust in this thesis.

Arizona Road Dust comes in four different grades: ultrafine, fine, medium, and coarse. These grades refer to the particle sizes within the powder. Fine grade Arizona Road Dust was used in this study. The particle size distribution by volume was obtained through the manufacturer, Powder Technology Inc., shown in Figure 2.4. This powder will be termed super-polydisperse because the particle size range is so large.

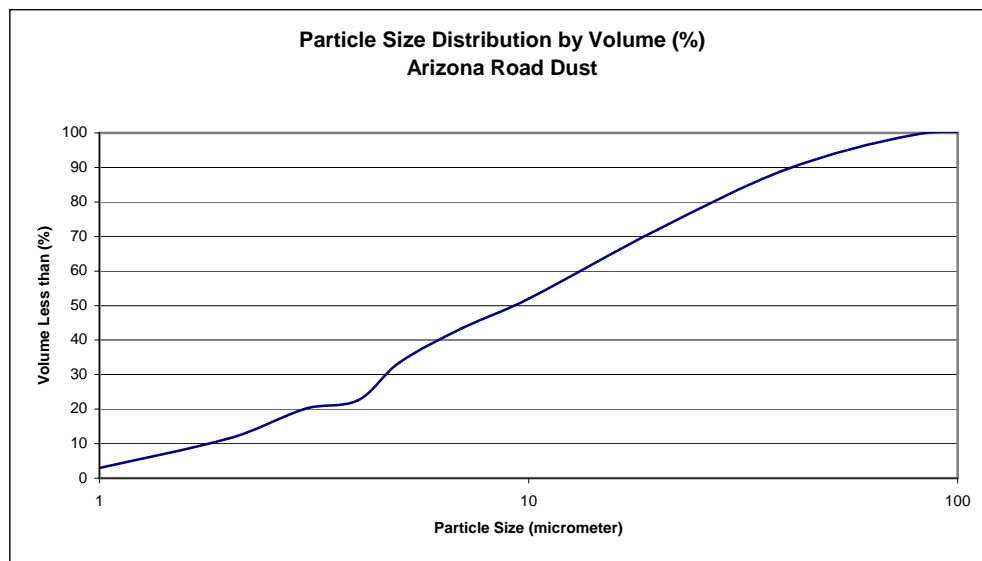


Figure 2.4: Arizona Road Dust Particle Size Distribution (Adapted from Powder Technology Inc. 2006)

2.4 Fire Extinguisher Grade Sodium Bicarbonate

Class BC fire extinguishers are used to combat grease, liquid, and electrical fires. Sodium bicarbonate powder is typically used as the fire suppressing agent and is propelled by compressed gas. The sodium bicarbonate acts as a thermal ballast agent, reducing the heat within the flames to levels that do not support further chemical reactions.

The sodium bicarbonate used in this experiment is marketed by Amerex Corporation. The model number is CH 512 and it comes in a fifty pound container. TEM images of sodium bicarbonate particles will be shown in the next section but no size distribution information was available through the manufacturer.

2.5 Transmission Electron Microscopy

2.5.1 TEM Laboratory

Transmission Electron Microscopy (TEM) was used to look at all the powders listed in the Materials Section. Imaging was performed by Dr. Dan Boyle of the Kansas State University Biology Department in the Microscopy Laboratory. The images were collected on an FEI CM100 Transmission Electron Microscope.

2.5.2 Sample Preparation

All samples were placed on 200 mesh copper grids purchased from Electron Microscopy Sciences (www.emsdiasum.com). The EMS part number for the grids is CF200-Cu. The grids provide structural support to a thin film of carbon on which the samples are placed. The carbon film is very delicate and must be preserved during the sampling process. A pair of fine point tweezers (EMS 3C) were used to hold the grid on the exterior portion, away from the central viewing region. The grids were dipped into the powder containers to obtain a sample. The tweezers were then tapped on the rim of the powder container to reduce the number of particles on the grid. Individual particle boundaries cannot be seen if the number density is too high.

This sampling technique could present a size bias in the TEM images. If the TEM grids are tapped to remove excess particles, the large particles would most likely experience the greatest separation force due to their mass. Size distribution information will not be gathered from TEM images due to this possible source of error. However, much information can be obtained concerning other physical characteristics of the particles.

2.5.3 NanoActive™ MgO

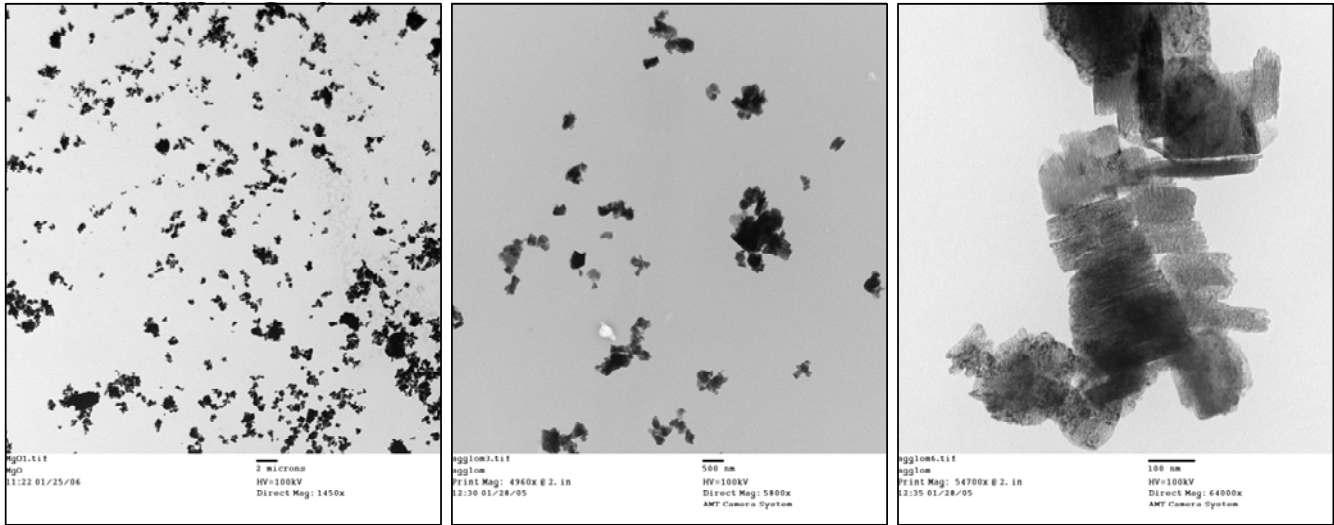


Figure 2.5: TEM Images of NanoActive™ MgO Particles

The three images shown in Figure 2.5 are of NanoActive™ MgO Particles. The image on the far left shows a view of the overall population. The pictures in the middle and on the right are images at higher resolution. The platelet-like structure of these particles can be seen in the image on the far right. The primary particles appear to be roughly 100 to 300 nm in size. Those primary particles form aggregates like the one shown in the image on the far right. The aggregates then come together to form agglomerates like those seen in the image on the far left. Particles in the 2 to 5 μm range can be seen in this image. The platelets in the image on the far right appear to be translucent. This implies the particles are very thin. TEM images an object by the electrons that pass through that object. If the object is too thick, no electrons pass through it, and no significant level of detail is captured.

2.5.4 NanoActive™ MgO Plus

Figure 2.6 shows NanoActive™ MgO Plus particles imaged with a TEM. The particles are not translucent like the NanoActive™ MgO particles. These images imply some depth into the viewing plane. Unlike the NanoActive™ MgO particles the NanoActive™ MgO Plus particles are comprised of primary units on the order of 5-10 nm. It seems the primary particle size influences the overall structure of aggregates and agglomerates. Each dark section in the image on the far right is an agglomerate of 5-10 nm particles. The agglomerates appear to fall within a range of 0.5-4 μm . This can be seen in the overall population view in the image on the far left.

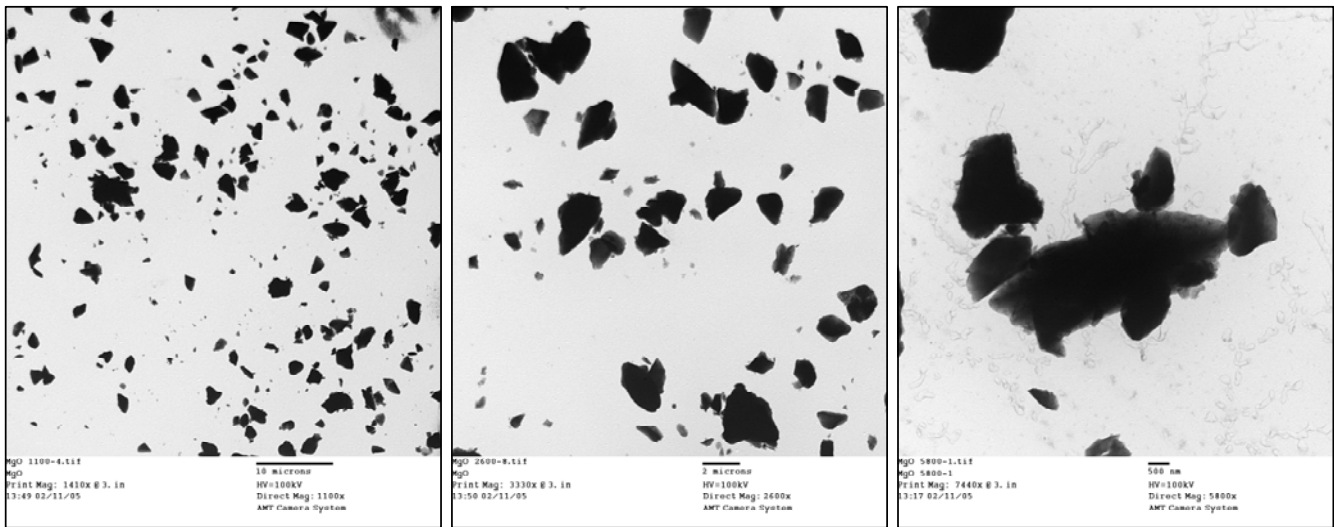


Figure 2.6: TEM Images of NanoActive™ MgO Plus Particles

2.5.5 TSI Hollow Glass Spheres

TSI Hollow Glass Spheres were imaged and are shown in Figure 2.7. The image on the left shows a single sphere with a diameter approximately 15-20 μm . The image on the right shows an aggregate of hollow glass spheres, which was unexpected. The aggregation seen in Figure 2.7 is most likely due to some electrostatic charge induced during the sampling process.

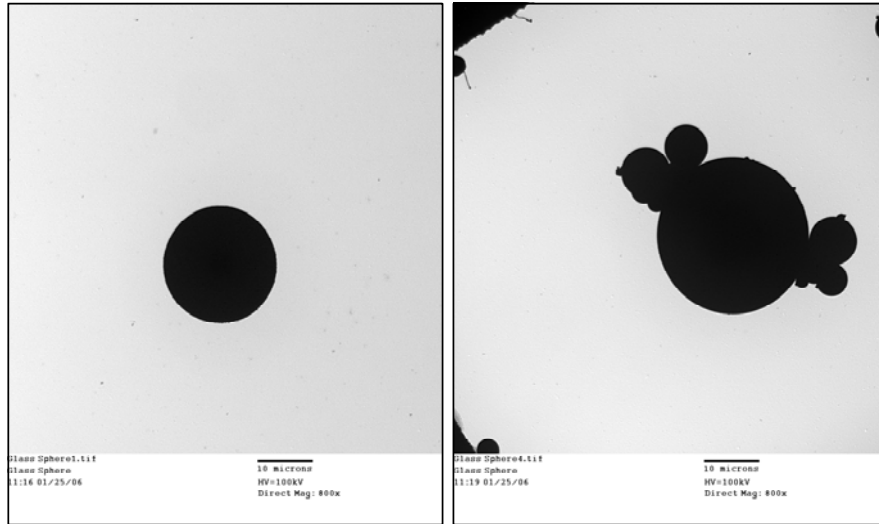


Figure 2.7: TEM Images of TSI Hollow Glass Spheres

2.5.6 Arizona Road Dust

Figure 2.8 shows TEM images of Arizona Road Dust particles. The particles imaged in the overall population (far left) appear to be in the 0.5 to 10 μm range. The manufacturer provided data suggests there are larger particles in the population. The absence of large particles in the TEM images may be attributed to the sampling technique. As the TEM grids were tapped on the side of the container, the larger particles may have been more likely to come off the grid. The particles appear opaque which suggests substantial depth into the viewing plane. The particles are also observed to be rougher on the edges than the NanoActive™ MgO and MgO Plus particles.

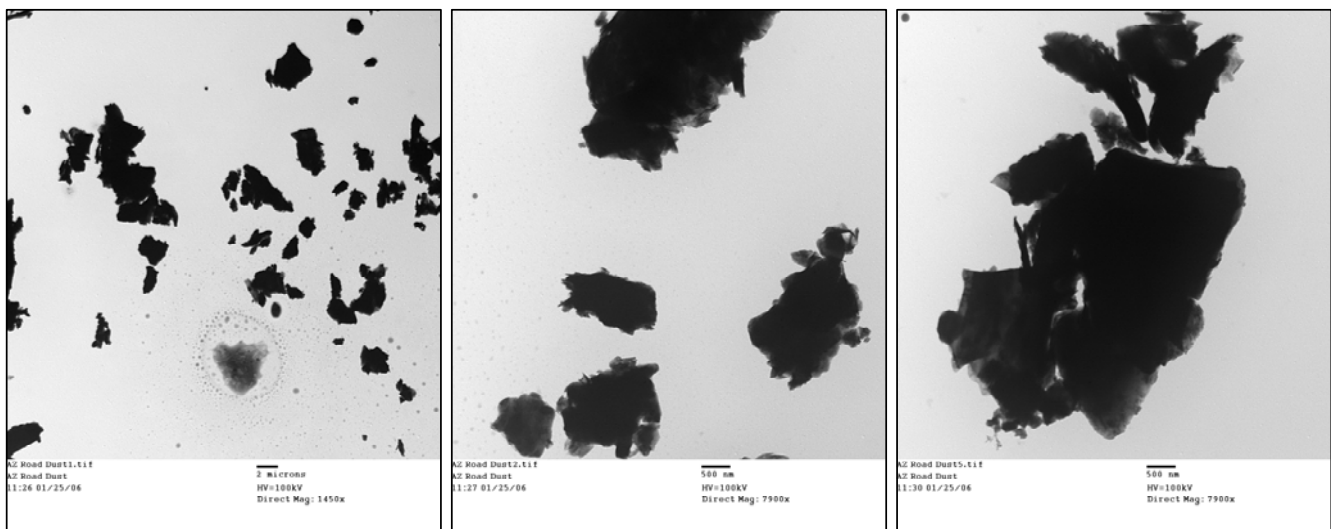


Figure 2.8: TEM Images of Arizona Road Dust Particles

2.5.7 Sodium Bicarbonate

Figure 2.9 shows the images taken of Sodium Bicarbonate particles. The image on the far left shows an overall population view. Particles as large as 10 μm can be seen in this image. The particle on the far right is one of the smallest particles observed. The diameter of this particle is approximately 0.5 μm . The particles appear to have a somewhat fibrous structure. The middle image shows this well. On the edges of each particle appear sharp protrusions.

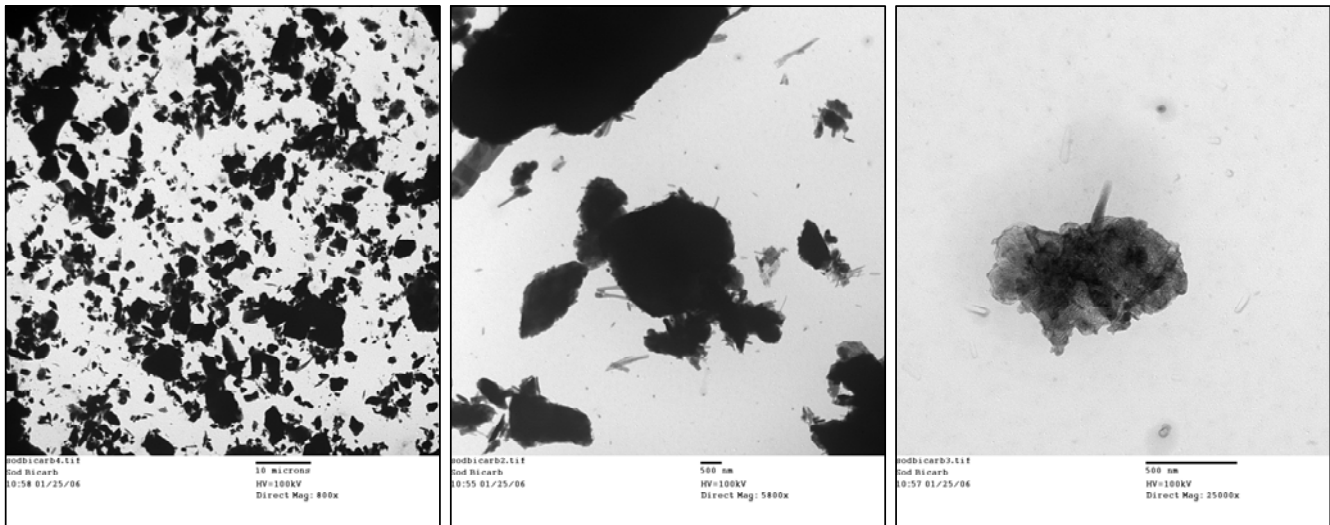


Figure 2.9: TEM Images of Sodium Bicarbonate Particles

3 ADHESION AND COHESION REVIEW

3.1 Introduction

The study of cohesive and adhesive forces is important in aerosol science because they are almost always present to some degree. Cohesion is when two objects of the same material stick together. Adhesion is when objects of dissimilar materials stick together. Aerosol particles are subject to both cohesion and adhesion. These attractive forces determine the size of aggregate and agglomerate particles as well as the forces required to break them apart. These attractive forces must be understood to control the size of particles within an aerosol.

3.2 Interparticle Forces

Interparticle forces are often attractive in nature and cause particle adhesion and cohesion. Adhesive and cohesive forces are highly dependent on the physical and chemical properties of the particles. The size, shape, surface texture, and porosity are all physical characteristics that could influence the magnitude of interparticle forces. Hydrophobicity, hydrophilicity, and ionizability are chemical properties that may also influence forces between particles. Interparticle interactions should be evaluated on a case by case basis. The dependence of cohesive and adhesive forces on the physical and chemical properties of the particles makes exact quantification difficult. However, generalizations can be made concerning the three major forces that cause cohesion and adhesion: van der Waals, electrostatic, and capillary forces.

3.2.1 van der Waals Forces

The van der Waals (vdW) force acts between all molecules and atoms regardless of charge. The van der Waals force is also known as the dispersion force, London force, and induced-dipole force in the literature, but will be referred to as the van der Waals force from this point forward. The random movement of electrons can create conditions where the center of mass of the electron cloud does not coincide with the center of mass of the nucleus. This condition is called a momentary dipole. The momentary dipole of one particle then induces complementary dipoles in neighboring particles. The dipoles

are then attracted to each other and form a force which can be as large as two or three times the weight of the particle (Hickey 1994). Although vdW forces can be very large in certain instances, the distance between the two particles is the limiting factor for the magnitude of the force. The attractive energy varies inversely with the sixth power of the distance between two particles. Therefore, the particles must be very close for vdW forces to cause cohesion. Any method in which the interparticle distance can be increased will ease the deaggregation process. Approximations for vdW forces between particles have been developed and are presented in Section 3.3.

3.2.2 Electrostatic Forces

The occurrence of electrostatic phenomena in powder handling operations is common and presents various advantages and disadvantages depending on the application. Electrostatic effects can be put to good use in operations where a mixture of materials needs to be separated. Forces created by electrostatic charge can also be deleterious to an operation by causing particle adhesion, negatively influencing particle flow dynamics, and in the worst case, explosions seen in grain silos.

Electrostatic forces are created when two charged particles interact. Coulomb's law,

$$F_E = K_E \frac{q \cdot q'}{R^2}, \quad (3.1)$$

is the fundamental equation of electrostatics. This law relates the force of interaction, F_E , between two point charges. The separation distance between the charges is denoted R . This force can be either repulsive or attractive depending on the sign of the charge on each particle, q and q' . K_E is a constant of proportionality and is given by

$$K_E = \frac{1}{4\pi\epsilon_0} \quad (3.2)$$

where ϵ_0 is the permittivity of free space.

When two dissimilar solid materials come into contact, and then separate, electrical charges are often exchanged through the contact area. This process is called contact electrification, also known as triboelectrification. Triboelectrification is a largely unexplained phenomena but many theories have been proposed to explain the transfer of

charge between materials. The force behind the transfer of electrons is often related to the difference in the work function between the two materials. The work function of a material can be described as the minimum energy required to pull the weakest bound electron from the surface to an infinite distance. Often times the triboelectrification process between two materials can be described by a set of empirical results arranged into a table called the triboelectric series.

The triboelectric series is a list of materials arranged according to the polarity of charge acquired by bringing them into contact with another material. It is simply a set of materials organized into tabular format to help in the selection of materials considering electrostatic charge effects. These lists are difficult to reproduce and are largely dependent upon the conditions under which the experiments are carried out. Correlations have been made between the triboelectric series and the permittivity of material. Materials with low permittivities tend to accept electrons, becoming negatively charged when contacted by materials higher in the series. Materials with high permittivities give up electrons, becoming positively charged, and are located higher on the triboelectric series. Factors like particle size, shape, and relative humidity all have an effect on the triboelectrification of materials.

The shape can affect the way triboelectrically charged particles behave as well. In a spherical particle, the equilibrium surface charge density would be uniform over the surface. However, in an irregularly shaped particle, the charge density tends to be higher at regions of greater curvature (Bailey 1983).

Generally speaking, the smaller the particle, the greater the potential for electrostatic effects on that particle. This can be explained by the relationship of particle diameter to particle mass and surface area. Since the particle's mass decreases with the third power of diameter and the surface area decreases with the diameter squared, the net surface charge to mass ratio is higher for smaller particles (Bailey 1983).

The adhesion of particles to surfaces in material transport operations presents a large problem. In manufacturing plants, the adhesion of materials creates the need for more cleaning of system components, the loss of material, and inefficiencies in operational speed. The triboelectric charge induced by material contact can lead to adhesion, which then causes particle distortion. Particle distortion allows for van der Waals forces to become effective and in most cases dominant by bringing the particles closer together (Bailey 1983).

3.2.3 Capillary Forces

Cohesion tends to increase as the relative humidity of the air increases. At humidity above 65%, fluid begins to condense in the porous regions of the particles (Hickey 1994). A “liquid bridge” can form between neighboring particles and the surface tension of the liquid leads to an attractive force between the two. The capillary force between two smooth spherical particles of same size is given by $F_H = 2\pi\gamma R$, where γ is the surface tension of the fluid and R is the radii of the particles (Hickey 1994). When the vapor pressure of the surrounding air approaches the saturation pressure, the capillary force between two particles can be as high as twice the weight of one of particles.

3.2.4 Comparison of Interparticle Forces

Electrostatic, van der Waals, and capillary forces may each be the dominant interparticle force depending on particle characteristics and ambient conditions. Capillary forces can be very large depending on the humidity. The force is proportional to the particle size at humidity greater than 65%. High humidity also reduces the effects of electrostatic forces, increasing the likelihood that capillary forces are dominant for this case. However, the humidity is usually not this high. Capillary forces are assumed negligible for dry powders without substantial humidity levels. This reduces the possible causes of cohesion and adhesion to van der Waals and electrostatic forces.

The attractive vdW energy varies inversely as the sixth power of the particle separation. The electrostatic force varies as the inverse square of the separation distance and can be repulsive or attractive. The vdW forces are clearly dominant when the separation

distance is on the order of a few nanometers. At larger separation distances the vdW forces have little effect while the electrostatic forces are dominant. These two forces are also determined by material properties. If two particles are uncharged or have little difference in electron work function, electrostatic forces can be neglected and vdW forces are assumed dominant. These examples illustrate the difficulty in generalizing which interparticle forces are dominant. Each case should be evaluated independently to determine which forces are significant and which may be neglected.

3.2.5 Measurement of Adhesive Forces

There are three traditional methods used to measure the magnitude of adhesive forces in particles within the 0.5-50 μm range: centrifugal, aerodynamic and hydrodynamic, and vibrational. By allowing particles to adhere to a surface, then placing that surface in a centrifuge, the separation force can be measured by noting the speed at which the centrifuge is rotating when the particle separates from the surface. The required force to separate the particle may also be measured by blowing on the surface and measuring the velocity of air or liquid required for separation. Vibrating apparatus have been used to measure the force required to separate carbon black from cellophane surfaces (Hickey 1994). Newer methods for measuring particle adhesion and cohesion have been developed as well. Atomic Force Microscopy (AFM) can be used to measure the cohesive and adhesive forces between particles and other materials. The particles are attached to probes with force measurement equipment and the forces required to break cohesive and adhesive bonds are measured (Bogat 2004).

3.3 Intermolecular and Surface Forces

The van der Waals forces of interaction are believed to be the most significant cohesive and adhesive forces in aerosol particles of negligible electrostatic charge and moisture. Israelachvili quantitatively describes the intermolecular and surface forces caused by van der Waals interactions (Israelachvili 1985).

The London approximation is an expression for the attractive energy between two identical atoms or molecules and is given by

$$U(r) = \frac{\alpha_o^2 h\nu}{(4\pi\epsilon_o)^2 r^6}. \quad (3.3)$$

This equation was presented in 1937 and shows the dependence of energy on the distance between the two atoms. The energy varies as the inverse of the particle separation to the sixth power. For this reason, these forces are considered short range forces. The atoms must be very close for the energy to be significant.

The expected molar lattice energy or cohesive energy of a van der Waals solid with a coordination number of 12 is given by

$$U \approx 7.22N_o \left[\frac{3\alpha_o^2 h\nu}{4(4\pi\epsilon_o)^2 \sigma^6} \right]. \quad (3.4)$$

The equilibrium interatomic distance in the solid is represented by σ , the first ionization potential is represented by $h\nu$, ϵ_o is the permittivity of free space, N_o is Avagadro's constant, and α_o is the electronic polarizability.

This may be compared with the latent heat of melting plus vaporization, $L_m + L_v$, which is approximately equal to the latent heat of sublimation, or the cohesive energy. Thus, U is the energy required to transform the solid phase of the material to the gaseous phase.

When the particles become large, as in the case of molecules and particles, the vdW forces no longer act through the centers of the molecules, they act through the centers of electronic polarization for each molecule (Israelachvili 1985). This makes the results for Equation 3.4 smaller than the actual value for the cohesive energy. The interaction energies of all the atoms must be considered to find the interatomic and surface forces present in larger molecules and particles.

3.3.1 Energy of Interaction for an Atom and an Infinite Planar Surface

The first step in quantifying the interactions of large particles and surfaces is to develop the interaction between one atom with an infinite planar surface. Using the London approximation, Equation 3.3, all of the individual interactions between the one atom and each atom in the infinite surface are summed. This interaction energy is given by

$$W(D) = \frac{-\pi C \rho}{6D^3}. \quad (3.5)$$

$W(D)$ is the energy of interaction and D represents the distance from the center of the single atom to the center of an atom at the surface of the infinite plane. The number density of atoms or molecules in the solid is given by ρ . C is the London dispersion force coefficient and is given by

$$C = \frac{3}{4} \frac{\alpha_o^2 h\nu}{(4\pi\epsilon_o)^2}. \quad (3.6)$$

From the previous result, Equation 3.5, Israelachvili derives expressions for the energy of interaction of a spherical particle with an infinite plane as well as the energy of interaction for a planar surface with unit area with an infinite surface.

3.3.2 Energy of Interaction for a Sphere and an Infinite Surface

The energy of interaction for a sphere with an infinite plane is given by

$$W(D) = \frac{-\pi^2 C \rho^2 R}{6D} \quad (3.7)$$

where R is the sphere radius and D is the separation distance between the sphere and plane. This relation holds when the separation distance is much less than the radius of the sphere, $D \ll R$.

The individual interactions of each atom in the sphere with the infinite plane are summed over the sphere. The stipulation on the relative size to the separation distance is important because only those atoms of the sphere within about $2D$ of the plane contribute to the overall interaction energy (Israelachvili 1985).

For two spheres of equal radii R , and separation distance D , $D \ll R$, the energy of interaction is found to be $1/2$ the result of Equation 3.7. If the sphere radii are much less than the separation distance, $D \gg R$, the energy of interaction varies as $1/D^6$, as for two molecules. This case is approximated by the London equation.

3.3.3 Energy of Interaction of a Plane of Unit Area and an Infinite Plane

For two planar surfaces at the same separation distance, D , apart, the energy of interaction is given by

$$W(D) = \frac{-\pi C \rho^2}{12D^2} \text{ per unit area .} \quad (3.8)$$

This result is achieved by summing all of the interaction energies of each molecule in the plane of unit area with respect to the infinite plane. For real planar surfaces, this result is only applicable when the separation distance is much less than the lateral dimensions of the plane.

For more rigorous derivations of Equations 3.5, 3.7, and 3.8, the reader is referred to *Intermolecular and Surface Forces* (Israelachvili 1985).

3.3.4 Conclusions from Energies of Interactions

Several important conclusions should be drawn for the three interaction energies described in previous sections. To arrive at Equations 3.7, and 3.8, the interaction energy of one atom with an infinite planar surface was summed for a particular geometry. This summation accounts for all interactions between molecules of surface 1 and surface 2. However, it does not account for the cohesive interactions between the molecules in either single surface, i.e. surface 1 molecules interacting with other surface 1 molecules. This would affect the results of the derivations but is difficult to consider computationally, therefore it will be neglected. For further detail see *Intermolecular and Surface Forces* (Israelachvili 1985).

Other conclusions regarding the behaviors of intermolecular forces are drawn by Israelachvili. Van der Waals interaction energies between large condensed bodies decay slower, $1/D$ and $1/D^2$, for spheres and planar surfaces, respectively, than it does for molecules and atoms, $1/r^6$. This makes the energies of interaction of macroscopic bodies more effective at longer ranges. Israelachvili also notes that no matter how large a sphere becomes it never approaches the behavior of a planar surface.

3.3.5 Derjaguin Approximation

All of the previously listed results were in terms of interaction energies. In application it makes sense to look at the forces created by these interaction energies. Forces are more easily measured and can be readily applied to engineering calculations.

The force of interaction between two spheres is given by

$$F(D) = 2\pi \left(\frac{R_1 R_2}{R_1 + R_2} \right) W(D). \quad (3.9)$$

This equation is called the Derjaguin Approximation. The force between two spherical bodies is related through the derived expression for the interaction energy between a planar surface of unit area with an infinite surface, Equation 3.8.

In the special case of $R_1 = R_2$,

$$F(D) = \pi R W(D). \quad (3.10)$$

When the separation distance approaches the interatomic spacing, $D = \sigma$, $W(\sigma) = 2\gamma$, where γ is the conventional surface energy per unit area of a surface. The Derjaguin approximation then becomes

$$F(\sigma) = F_{ad} = 4\pi \left(\frac{R_1 R_2}{R_1 + R_2} \right) \gamma. \quad (3.11)$$

This equation relates the cohesive force between two spheres to the surface energy of the material. The surface energy, γ , is defined as the free energy change when the surface area of a medium is increased by unit area.

4 DEAGGREGATION REVIEW

4.1 Introduction

The dispersion of powders as aerosols has many commercial, industrial, and military applications. Powder coating equipment, fire extinguishers, and devices used to neutralize hazardous substances all disperse powders in aerosol form. The particles being entrained and aerosolized are often subject to many different fluid flows such as shear, turbulence, and accelerating air streams. The particles can also hit obstacles in the flow. These situations create forces on and within the particles, tending to break the particles apart. The deaggregation of particles in aerosols due to fluid dynamic and other forces has been studied rather extensively. Some fundamental theories of deaggregation and experimental studies of these theories are presented in this chapter.

4.2 Stresses in a Single Spherical Particle in Viscous Flow

Bagster and Tomi (1974) analyzed the stresses within a single spherical particle due to viscous flow. The first case analyzed by Bagster and Tomi was for a single spherical particle in uniform flow. The maximum tensile and shear stresses in N/m^2 , σ_{\max} and τ_{\max} , are present when the particle is initially put into the flow and are given by,

$$\sigma_{\max} = \tau_{\max} = \frac{3\mu u_r}{d_{ps}}. \quad (4.1)$$

The mean velocity of the flow field is denoted u_r and d_{ps} is the particle diameter.

The second case Bagster and Tomi analyzed was simple shear flow. The maximum tensile and shear stresses, σ_{\max} and τ_{\max} , are present when the particle is initially put into the flow and are given by

$$\sigma_{\max} = 5\mu\gamma, \quad (4.2)$$

$$\text{and } \tau_{\max} = 8.5\mu\gamma, \quad (4.3)$$

where the velocity gradient is denoted γ and μ is the viscosity.

4.3 Fundamental Work on Particle Deaggregation

Kousaka, Okuyama, and Shimizu developed a theoretical and experimental basis for most current research in the field of particle deaggregation (Kousaka et al. 1979). The authors develop a hierarchy of deaggregation mechanisms from a theoretical standpoint and then validated those theories experimentally.

4.3.1 Stress Induced in a Spherical Particle Due to Impact

Stresses within a particle are created when it collides with an obstacle in the flow. The mid-plane compressive stress, σ_{impact} , in a spherical particle is given by

$$\sigma_{impact} = \frac{2}{3} \rho_p d_p \left(\frac{v_i}{\Delta t} \right). \quad (4.4)$$

The density and size of the particle are represented by ρ_p and d_p , respectively, and the velocity at impact is v_i . The duration of impact is denoted Δt and is often difficult to quantify.

The compressive stress at smaller portions of the particle would be much higher and an additional bending moment would contribute to this stress in the case of irregularly shaped particles. This calculation is further complicated by difficulties in finding the probability of impact occurring, which must be factored in when considering the deaggregation of aerosol particles.

4.3.2 Stresses Induced in Aggregates in Uniform Flow

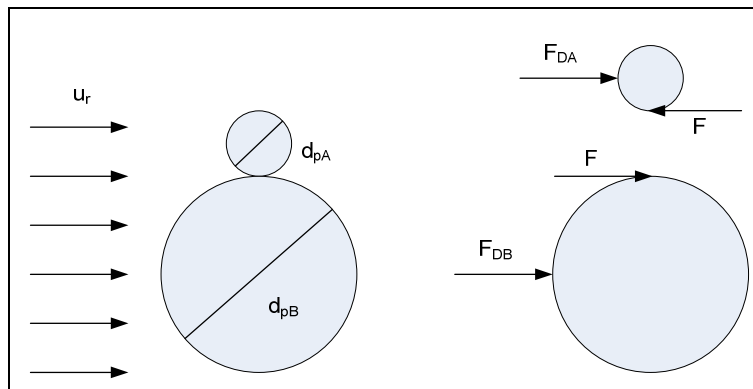


Figure 4.1: Aggregate in Uniform Flow (Adapted from Kousaka et al. 1979)

The stress at the contact point between particles A and B is analyzed as the aggregate is introduced into a uniform flow field. Figure 4.1 depicts this scenario. Initially the velocities of each particle are the same. If the two particles are separated and the free body diagrams are drawn for each, there is a reaction force, F , and a drag force, F_D , acting on each particle. Newton's second law for each particle can be written using Stokes law for drag force. Assuming both particles' accelerations are equal at that instant, there are two equations and two unknowns. Further assuming the density of each particle is the same, the interaction force can be calculated by

$$F = 3\pi\mu u_r d_{pA} d_{pB} \frac{(d_{pB} - d_{pA})}{(d_{pA}^2 - d_{pA}d_{pB} + d_{pB}^2)}. \quad (4.5)$$

Kousaka et al. give the shear and tensile stresses at the point of contact for an aggregate in uniform flow as

$$\tau_{uniform} = \sigma_{uniform,tensile} = \frac{4F}{\pi(c_1 d_{pA})^2}, \quad (4.6)$$

where c_1 is a constant between 0 and 1. This constant accounts for the manner of adhesion between the particles. The shearing stress becomes larger as the constant is reduced. The bending stress at the contact point is given by

$$\sigma_{uniform,bending} = \frac{16F}{\pi c_1 (c_1 d_{pA})^2}. \quad (4.7)$$

From this theory, Kousaka, Okuyama, and Shimizu concluded that as the particle sizes become similar, the aggregates are harder to break apart. The authors also claim that small aggregates are much easier to break apart than large aggregates. If the sizes of the particles are known, the force between them can be calculated. The authors note that these stresses are much larger than those of Equation 4.1 for a sphere in uniform flow. For a size ratio of 2:1, the bending stress induced in an aggregate given by Equation 4.7 is at least 21 times that of the maximum stress given by Equation 4.1 for a spherical particle in uniform viscous flow. The bending stress is even larger if c_1 is set less than unity.

4.3.3 Stresses Induced in Aggregates in Simple Shear Flow

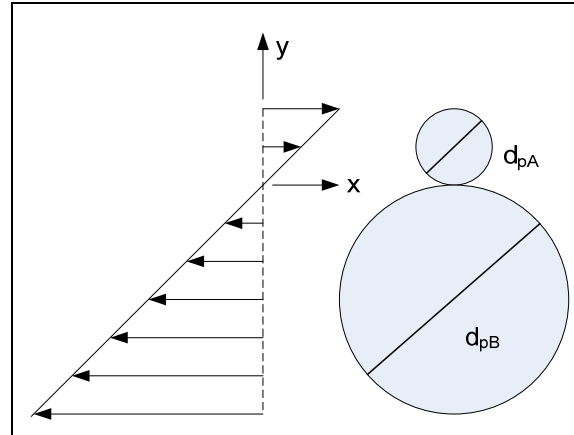


Figure 4.2: Aggregate in Shear Flow (Adapted from Kousaka et al. 1979)

Kousaka et al. (1979) claim the bending stress is much larger than the shearing stress when the same aggregate is introduced into a simple shear field. When particle b is assumed larger than particle a, and the moment of the drag force is summed from $y=0$ to $y=d_{pA}$. The bending stress at the area of contact is given by

$$\sigma_{bending, shear} = \frac{\int_0^{d_{pa}} y \cdot dR_f}{\frac{\pi}{32} (c_1 d_{pa})^3} \approx \frac{93\mu\gamma}{\pi c_1^3}. \quad (4.8)$$

The ratio of bending stress caused by uniform versus shear flow is given by

$$\frac{\sigma_{bending, uniform}}{\sigma_{bending, shear}} \approx \frac{2.16u_r}{\gamma d_{pb}}. \quad (4.9)$$

A particle size ratio of 2:1 is assumed in this case. Kousaka et al. (1979) states that for small particles in most realistic cases, the term on the right hand side of Equation 4.9 will be greater than 1. Thus, the acceleration of a particle in a uniform flow causes a larger bending stress than that caused by a velocity gradient in the flow.

4.3.4 Stresses Induced in a Single Spherical Particle in Turbulent Flow

The derivations of stresses within a single spherical particle in turbulent flow rely heavily on Kolmogorov's Turbulence Theory and other turbulent relations, therefore, only results are presented here. For further explanation the reader is referred to the article written by Kousaka et al. (1979) or the book written by Finlay (2001).

The shearing stress within a spherical particle, in the mid-plane, induced by a locally isotropic turbulent flow is given by

$$\tau_{turbulent, large\ particle} \approx \frac{\rho_f \varepsilon^{2/3}}{10} d_{ps}^{2/3}. \quad (4.10)$$

The average energy dissipation rate is represented by the symbol ε and ρ_f is the density of the fluid. This equation is true for particles much larger than the turbulence scale. On this scale the inertial force exerted by the fluid on the particle is most significant. When the length scale of the particle is of the same magnitude as the turbulence scale the viscous shear forces become important and the equation becomes

$$\tau_{turbulent, small\ particle} \approx 3.1 \rho_f \sqrt{\varepsilon \nu} \quad (4.11)$$

where ν is the kinematic viscosity of the fluid. The bending stress at the mid-plane is given by

$$\sigma_{turbulent, bending, small\ particle} \approx \frac{10.8 \rho_f \sqrt{\varepsilon \nu}}{c_1^3} \quad (4.12)$$

for particle sizes similar to the turbulence scale.

Compared to the stresses calculated for other types of flow discussed in previous sections, the stresses induced in turbulent flow are small, even assuming large γ and ε , (Kousaka et al. 1979).

4.3.5 Experimental Validation of Deaggregation Theory

Kousaka, Okuyama, and Shimizu used five different dispersion devices to test the theoretically developed deaggregation mechanisms. Calcium carbonate and iron oxide particles were used for the test particles. The diameters of the calcium carbonate and iron oxide were 0.64 μm and 0.31 μm , respectively.

To test deaggregation via impaction, a device was used where the particles impacted 8 wire screens with wire diameters of 100 μm and 60 μm . Experimental results showed excellent agreement with theoretical considerations. The authors concluded the particles were impacting the wire meshes and the impaction forces were large enough to overcome

the cohesive forces of interaction. A large increase in the fine particle fraction was seen with an increase in inlet velocity.

A venturi device was used to determine the effects of acceleration and deceleration on deaggregation. The flow accelerates in the converging section of the nozzle. This acceleration creates an internal force within the particle. It was found that particle size decreased with an increase of venturi convergent angle. The convergent angle is a measure of how quickly the venturi reaches its minimum area. Increasing venturi convergent angle is synonymous with increasing the acceleration of the flow. The resulting data suggested acceleration was a less effective deaggregation mechanism than impaction.

An orifice in the flow was used as the third device. The deaggregation mechanisms in this flow were thought to be numerous and could include the sudden contraction of flow at the orifice (acceleration), particle impaction at the orifice face, or the velocity gradient and turbulence of the flow at the exit. The fourth device was similar to the orifice. It was a capillary tube of same diameter as the orifice, but with an elongated contracted area. The experimental results for the orifice and capillary tube were very similar, suggesting the same controlling deaggregation mechanism, which the authors attributed to impaction at the orifice face. The capillary tube length was increased by a factor of ten and no significant changes in deaggregation occurred. This led to the conclusion that the velocity gradient of the capillary tube had little effect, which agrees with the Kousaka's theory presented in section 4.3.3.

The last experimental deaggregation device used in this study was a chamber equipped with a stirring blade. The stirring blade was operated at 9,000 and 14,500 rpm. Violent turbulence was induced in this experimental device, however, it did not seem to deaggregate the particles as well as the mesh and venturi nozzles.

4.3.6 Conclusions from Fundamental Work on Deaggregation

Based on their theoretical and experimental work, Kousaka, Okuyama, and Shimizu concluded that impact is the most effective deaggregation mechanism. They also concluded that deaggregation can be a result of acceleration, including that in turbulence, when the relative velocity between the particle and the fluid is large. For this case, irregularly shaped particles are even easier to deaggregate. Lastly, it was concluded that a shear flow is less effective at deaggregating particles than impact and acceleration.

4.4 Recent Experimental Studies on Particle Deaggregation

Even though Kousaka, Okuyama, and Shimizu developed a fundamental basis for understanding the deaggregation of aggregates in a flow, the results cannot be used to quantitatively predict the deaggregate of actual powders (Endo 1996). Real powders are composed of polydisperse, non-spherical particles, making calculation of deaggregate forces difficult. Most recent developments involving particle deaggregation are empirical for this reason.

The pharmaceutical industry is perhaps one of the largest groups studying the deaggregation of aerosol particles. Dry Powder Inhalers (DPI's) are medical devices that rely on deaggregation extensively to break down inhaled aerosols into respirable particles that can reach the deep lung. Most inhaler medications are 1-2 μm particles that are attached to larger carrier particles. These carrier particles, often lactose monohydrate, are roughly 70 μm in size. The purpose of the carrier particles is to help entrain the medicine particles into the air stream. Once the agglomerated particles are entrained, the medicine particles must be separated from the carrier particles. After deaggregation the carrier particles impact the back of the throat due to their inertia whereas the medicine particles continue to follow the air stream until they are deposited in the deep lung. The effectiveness of the medicine is therefore dependent upon the degree of deaggregation and is studied to improve delivery methods. In these studies the particle size distribution is measured after deaggregation to determine the effectiveness of such devices.

There are various ways to measure the size distribution of aerosols. Cascade impactors rely on stopping distance to separate large particles from small particles. Another class of particle size analyzers use successive laser beams to measure the time-of-flight of a particle through a small distance. The time-of-flight is then used to calculate the aerodynamic diameter of the particle. One commercially available time-of-flight analyzer is called the Aerosizer. The Aerodisperser, also commercially available, is used to aerosolize the powder by injecting a small pulse of air through the powder reservoir. For a diagram of the Aerosizer and Aerodisperser, the reader is referred to the article written by Laitinen and Juppo (2003).

The Aerodisperser has multiple controls to aid in the dispersion process. Different settings are appropriate for dispersing different powders. One control is an annular gap region that is increased or decreased to create a shear force on the aerosol particles. A dispersing pin is also placed in the inlet region of the Aerodisperser to induce impaction based deaggregation. Increasing the velocity of the pulse jet increases the velocity of the aerosol through the Aerodisperser, making impaction more likely at the impaction pin. This setting on the Aerodisperser is called deagglomeration control and can be set to normal or high.

4.4.1 Shear Experiments

Many pharmaceutical studies have analyzed the effects of changing the two previously discussed settings on the size distributions of drug particles measured by the Aerosizer. Laitinen and Juppo (2003) found the effects of increasing shear were material dependent. Some drug particles, e.g. PVP, showed clear evidence of deaggregation with increasing shear. When the lactose carrier particles were dispersed, the size distribution shifted toward larger particle sizes with increasing shear. This could have been representative of shear induced agglomeration commonly seen in colloidal systems. The velocity gradient allows for particles to come into close contact, and at that point, cohesive forces cause aggregation. This study showed aggregation and deaggregation as a result of varying shear forces on aerosol particles.

Several other research groups have also found that increasing shear in the Aerodisperser shifted the particle size distributions of powder inhaler formulations to smaller sizes (Mendes et al. 2004 and Begat et al. 2004). These studies suggest increasing shear increases deaggregation.

Begat et al. (2004) sought to correlate the cohesive-adhesive forces in particles to the aerodynamic forces associated with dispersion. To measure the cohesive-adhesive forces on particles, atomic force microscopy was employed. Three materials were used in this study, salbutamol sulfate (drug), budesonide (drug), and lactose monohydrate (carrier). Both the lactose particles and the budesonide particles showed significant decreases in median particle size when high shear force was used. The salbutamol sulfate particles were small for both levels of shear, suggesting the particles deaggregated at small shear forces. When these results were coupled with the data from atomic force microscopy, it was found that the degree of deaggregation decreased exponentially as a function of agglomerate cohesive strength (Begat et al. 2004).

4.4.2 Impaction Experiments

Particle impact is another deaggregation mechanism that has been studied extensively. When a particle is large, having sufficient inertia, the particle trajectory deviates from the path of the flow. This is the principal behind cascade impactors. The aerosol is accelerated through small holes with the flow normal to the impaction plate. The air must flow around the impaction plate. If the particles' inertia are large they will move along the straight path toward the plate rather than move with the flow. The large particles hit the impaction plate and stick. The smaller particles follow the flow around the plate onto the next stage in the impactor. This sequential arrangement of impaction plates and nozzles separates the particles into several size classes of particles.

Theoretically, impaction is the most effective particle deaggregation mechanism (Kousaka et al. 1979). The sudden deceleration of the particle is said to create large internal forces which are usually much greater than the cohesive properties of the particles. Many studies have explored impaction as a deaggregation mechanism.

The other control on the Aerodisperser discussed previously is called deagglomeration control. It varies the velocity of the particles through the device, leading to more particle impact at the impaction pin. The study by Mendes et al. (2004) suggests no significant effects in the size distribution of drug particles with respect to changes in this variable. The particles in this study were in the 1-10 μm range. The likelihood of impaction is dependent upon both particle size and velocity. It is difficult to determine if particles should have hit the impaction pin without knowledge of the air velocity and particle density.

Other researchers have developed their own dispersion devices to deaggregate pharmaceutical aerosols (Voss and Finlay 2002). Voss and Finlay claim turbulence and impaction were the deaggregation mechanisms of greatest importance. Turbulence will be discussed in a later section. To subject the pharmaceutical aerosols to impaction the researchers put wire meshes in their dispersion device. They used an Anderson inertial impactor for particle size measurement. They found no significant difference between experiments without a mesh and with meshes having obstruction coverages of 54% and 84%. With lactose carrier particles having a mean diameter around 60 μm , this result was quite curious. Large particles are theoretically more susceptible to impaction. Impaction was ruled out as a significant deaggregation mechanism since there was no decrease in particle size with the presence of wire meshes.

Froeshke et al. (2003) studied the impaction deaggregation of silver, nickel, and titanium dioxide aerosols. The silver and nickel aerosols were generated by a spark discharge generator. The particles formed fractal aggregates with primary particles of diameters less than 10 nm. The titanium dioxide aerosol was produced by a flame synthesis technique. These were also fractal aggregates. The aerosols were impacted onto an impaction plate with a TEM grid on it. The TEM grids were then analyzed with respect to other particles that had been allowed to diffuse onto other TEM grids in separate experiments. The comparison of the two groups was used to determine the degree of

fragmentation. They found the degree of fragmentation as a function of impact velocity to be dependent on structure, material, and primary particle size (Froeshke et al. 2003).

The silver aggregates were more tenuous structures with fractal dimensions around 1.7. The researchers produced silver aggregates with a range of primary particle sizes from 3-9 nm. The silver aggregates with the largest primary particles, 9 nm, were almost completely fragmented at an impact velocity of 75 m/s. The aggregates composed of 3 nm particles showed only 10% fragmentation at an impact velocity of 120 m/s. This result suggested that aggregates and agglomerates with smaller primary particles can withstand greater impact forces.

The nickel aggregates had a fractal dimension around 2.5. No fragmentation was observed for the maximum impact velocity of 120 m/s. The primary particle size of 4 nm was thought to contribute to their ability to withstand impact. The higher fractal dimension also implies a higher coordination number, which could have led to higher cohesive strength.

The titanium dioxide particles had a structure very different from the other two materials. They formed agglomerated structures similar to blackberries. The subunits of the aggregate were round structures comprised of many primary particles. These subunits formed clusters. The bonds between the clusters could be broken, but the individual “blackberry-like” subunits maintained their form regardless of impact velocity.

4.4.3 Turbulence Experiments

The deaggregation of particles in turbulent flow is complicated due to the complex nature of turbulence and the irregular particle shapes of naturally occurring particles. Figure 4.3 is a schematic representation of turbulent eddies acting on an aggregate.

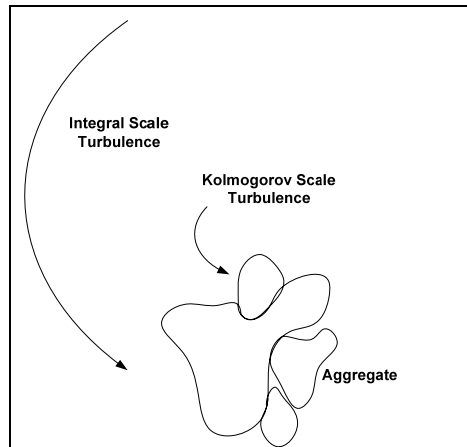


Figure 4.3: Aggregate in Turbulent Flow (Modified from Finlay 2001)

There are two scales involved in turbulence. If the turbulent length scale is much larger than the particle, on the order of millimeters, it is called integral scale turbulence. On this scale, eddies in the flow cause the entire particle to accelerate in one direction then another. These accelerations cause internal forces within the particle. The particle will deaggregate if the cohesive forces are less than the internal forces caused by the acceleration. On the other end of the spectrum, Kolmogorov scale turbulence has length scales on the order of the particle. This type of turbulent eddy would create a drag force on one of the aggregate's primary particles, causing it to separate from the aggregate. Integral scale turbulence has greater energy than Kolmogorov scales, therefore it is assumed to be the largest contributor to deaggregation (Finlay 2001).

Voss and Finlay (2002) tested the effects of turbulence on deaggregation in the same study as the wire meshes. Turbulence was induced in the flow by a ring of impinging jets. The fine particle fraction was found to increase as the flow through the impinging jets increased. The authors then used Laser Doppler Velocimetry to characterize the turbulence in their device. They concluded that deaggregation increased as a function of the turbulent velocity fluctuation.

4.4.4 Conclusions Drawn from Experimental Work

The studies presented in this review present a large and comprehensive set of deaggregation mechanisms. The authors of the different studies all point to one or more

flow characteristics they believe to cause particle deaggregation. Most dispersion devices create a combination of these mechanisms. This makes it difficult to isolate any one mechanism. A universal conclusion can be drawn from this set of research.

Deaggregation is highly dependent upon the material being dispersed. The size of the primary particles, the structure, and the material properties all affect the degree to which a particle can be broken down into its constituent particles. Some deaggregation mechanisms may work particularly well for a material of one structure, but not for another. Each case should be evaluated carefully taking into account the material properties and physical characteristics of the powder.

5 AEROSOL GENERATOR AND NOZZLE DESIGN

5.1 Introduction

Sufficient energy must be supplied to overcome interparticle forces present in fine powders, i.e. deaggregate aerosol particles. This input energy must also overcome any adhesive forces present between the particles and surfaces enclosing the dry powder. Understanding these properties and their influence on particle interactions is vital to the efficient and effective deaggregation of the powder.

5.2 Powder Dispersion Devices

Dry dispersion is the most widely used generation method for aerosols of solid particles. This method utilizes pneumatics to disperse the solid particulate material into a gas stream. The two most prevalent dry dispersing devices are dust generators and fluidized beds. Each device has two basic requirements, a mechanism to feed the powder into the device, and a means to suspend the powder in a gas stream.

The first basic requirement of a dry dispersion device is a way to feed the solid material into the aerosol generator. The simplest generators introduce the material into the air stream through gravity, vibration, or a combination of the two. This particular approach can yield inconsistent aerosol concentrations due to fluctuations in the bulk density of the material and inconsistent delivery of the material into the generator. A more accurate way to meter the powder into the generator would consist of an auger type feed system in which the powder was uniformly compressed to eliminate inconsistencies in the material from one location to the next. The second requirement of an effective dry dispersion device is to aerosolize the powder. The powder is fed into an air stream in some manner to create the aerosol. Many particles are broken down into their constituent parts by shear or other forces during the suspension process. The manner in which the aerosol is created is the main difference between dry dispersion devices.

A fluidized bed is a device that breaks up aggregates and suspends the particles in an airstream. The unique characteristic of a fluidized bed is the use of coarser particles to break the powder into smaller particles through mechanical agitation and collisions. The flow rate is sufficient to allow for suspension and transport of the small particles but remains too low to pick up the coarse particles. A dust generator does not utilize coarse particles like the fluidized bed. Many dust generators use high speed flows, vibration, or some other form of mechanical agitation to suspend the particles.

5.3 Aerosol Generator

An aerosol of consistent concentration had to be generated to measure the effects of impaction and fluid dynamic forces on aerosol particle size. Figure 5.1 shows a drawing of the aerosol generator used to disperse the powders in this study. Detailed drawings of each component can be found in Appendix A. Figure 5.1 is further detailed in drawing A.1.

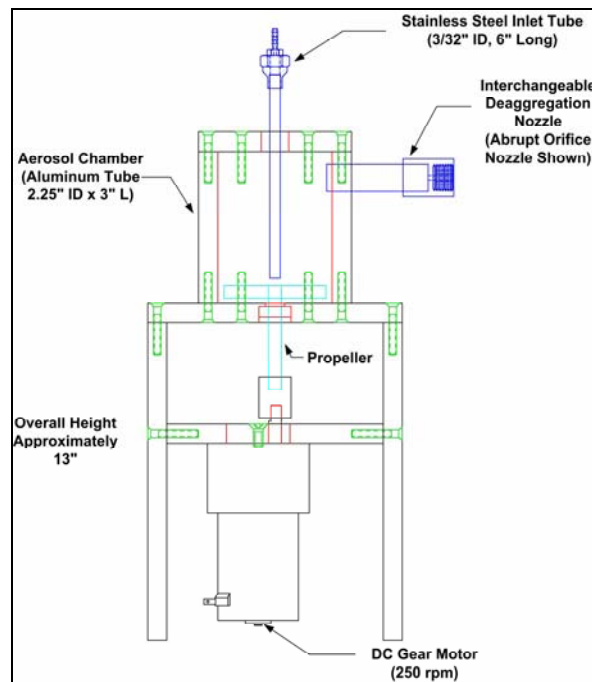


Figure 5.1: Aerosol Generator

A slug of powder is put into the aerosol chamber prior to dispersion. There is no automatic feed mechanism to supply a continuous flow of powder into the chamber.

There are three ports in the aerosol generator. Each port provides some flexibility as to how the aerosol generator functions. Air can be injected tangentially at the bottom of the aerosol generator to induce a swirling pattern within the chamber. The air can also be injected through the top of the container straight down at the powder. The outlet can be placed in the top center or tangentially as well. The inlet and outlet configuration shown in Figure 5.1 was the most effective at creating an aerosol of consistent concentration. The air inlet is located at the top-center facing downward and the air outlet is located at the top exiting tangentially to the chamber.

5.3.1 Air Inlet Tube

The dry powder aerosol generator shown in Figure 5.1 aerosolizes a slug of powder placed in the center of the chamber prior to the experiment. Compressed air is injected down through the center of the circular chamber through a tube which is screwed into the top plate. The air inlet tube is shown in Figure 5.2. The tube consists of a 1/8" NPT copper reducer that is attached to the stainless steel tube. The inlet tube is 2.5" in length from the bottom of the threaded plug to the outlet. A plastic barbed hose connector is screwed into the reducer as a connection to the compressed air source. A hole of same diameter as the inlet tube was drilled through a fully threaded plug. The plug and reducer were both epoxied to the stainless steel inlet tube. Finally, the inlet tube was screwed into the top plate via the threaded plug. In the drawings, supplied in Appendix A, the top plate is referred to as the orifice plate. The 3/32" orifice was screwed into the top plate in early experiments. This is the reason for it being called the orifice plate in the drawings.



Figure 5.2: Aerosol Generator Air Inlet Tube

5.3.2 Mechanical Agitation

A DC gear motor turns an adjustable pitch propeller to mechanically agitate the powder. The NanoActive™ MgO powder used in this study had a tendency to clump and adhere to other surfaces. These tendencies created the need for mechanical agitation. The motor helped achieve more consistent particle concentrations in the aerosols. The gear motor turned at approximately 250 rpm. At this speed no flow was induced within the chamber due to the motion of the propeller. Aluminum tape was attached to the edges of the propeller to wipe the sides of the aerosol chamber clean of material during the experiment. The aluminum wipers are shown in Figure 5.3.

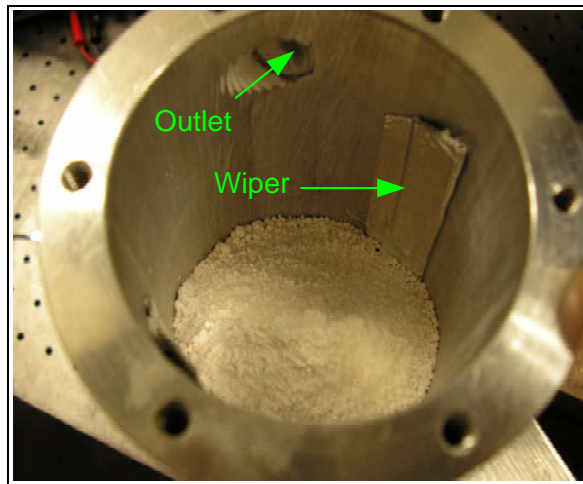


Figure 5.3: Aerosol Generator Aluminum Wipers

5.3.3 Deaggregation

The threaded port at the top of the aerosol generator chamber was used as the outlet. The deaggregation nozzles were screwed into this port, subjecting the aerosol particles to the various deaggregation mechanisms discussed in Chapter 4. Nozzle design will be discussed in the next section. Figure 5.1 shows the configuration of the abrupt orifice. A 2" nipple is screwed into the outlet port. A coupler is then used to attach a plug with a 3/32" hole drilled in it.

5.4 Deaggregation Nozzles

5.4.1 Abrupt Orifice

The abrupt orifice was the first nozzle configuration used experimentally. The configuration is shown in Figure 5.1. It is simple. A $3/32$ " hole was drilled in a threaded plug and connected to the outlet of the aerosol generator with a nipple and coupler.

There are many possible deaggregation mechanisms for this nozzle. These mechanisms include impaction at the orifice face, acceleration and deceleration at the orifice, and shear and turbulent effects at the exit. Additional nozzles were designed in an effort to isolate these mechanisms as the study progressed.

5.4.2 Converging-Diverging Nozzle

The turbulent motion and shear forces created at the outlet of the orifice jet were believed significant in the deaggregation process. The converging-diverging nozzle was designed to reduce these two characteristics of the flow. The converging-diverging nozzle is shown in Figure 5.4. The inside diameter at the inlet and outlet is the same as the inside diameter of the pipe nipple used with the abrupt orifice. The flow accelerates up to the $3/32$ " diameter region. The aerosol then decelerates until the exit region of the nozzle. The sudden contraction and expansion of the flow is eliminated. Since the streamlines do not change direction as rapidly as in the abrupt orifice, the large particles are less likely to deviate and impact any surface.

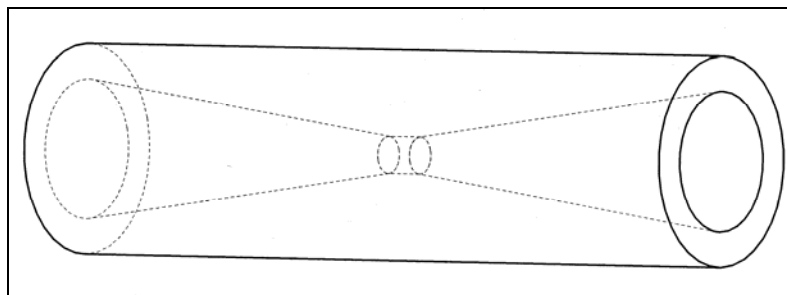


Figure 5.4: Converging-Diverging Nozzle

5.4.3 Converging Nozzle

The converging nozzle was designed to have the same exit characteristics as the abrupt orifice without the sudden acceleration of the flow through the orifice or impact at the orifice face. Figure 5.5 shows the converging nozzle. The inside diameter of the inlet is the same as the pipe nipple used in the abrupt orifice configuration. The outlet diameter is also the same as the abrupt orifice. The aerosol theoretically accelerates to the same velocity as in the abrupt orifice. The difference is in the acceleration. Similar to the converging-diverging nozzle, the streamlines converge more gradually. This eliminates the large acceleration of particles at the inside edge of the orifice and any possible impaction.

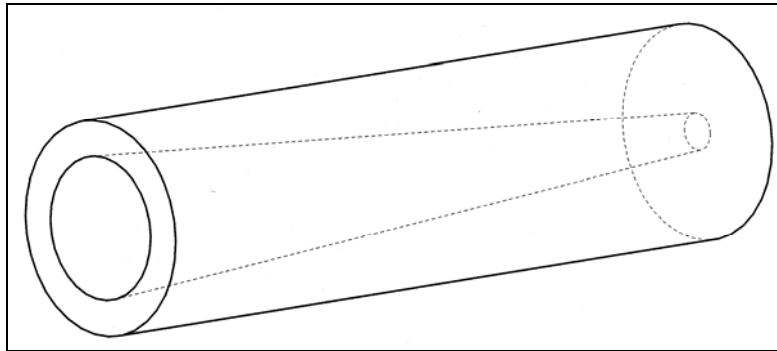


Figure 5.5: Converging Nozzle

The converging-diverging and converging nozzles were created using a Dimension 3D printer. The outside dimensions were modeled after the $\frac{1}{4}$ " NPT pipe nipple. The inside dimensions were created with flow control in mind. A rapid prototyping machine then formed the nozzles after which the threads were turned on the plastic.

5.4.4 Mesh Nozzle

Kousaka et al. (1979) and other researchers have suggested that impaction is an effective deaggregation mechanism. The mesh nozzle was created to increase the number of impaction events occurring within the deaggregation device. Three 26 x 26 wire meshes were inserted in the path of the flow. The diameter of the wire is 0.0075". The width of the each opening is 0.031". The nozzle was pieced together with aluminum washers, copper nipples and coupler, and epoxy. The mesh nozzle is shown in Figure 5.6.

With an open area of 64.8% there is a 35.2% chance that a particle would impact one of the wires for one mesh. This assumes impact is proportional to mesh area. With three successive meshes there is a 27% probability that any particle would make it through the nozzle without impact. This probability assumes that all particles in the projected area of the mesh would impact. Some particles would actually follow the fluid flow around the mesh. Therefore, at least 27% of the particles would make it through the nozzle without impact.

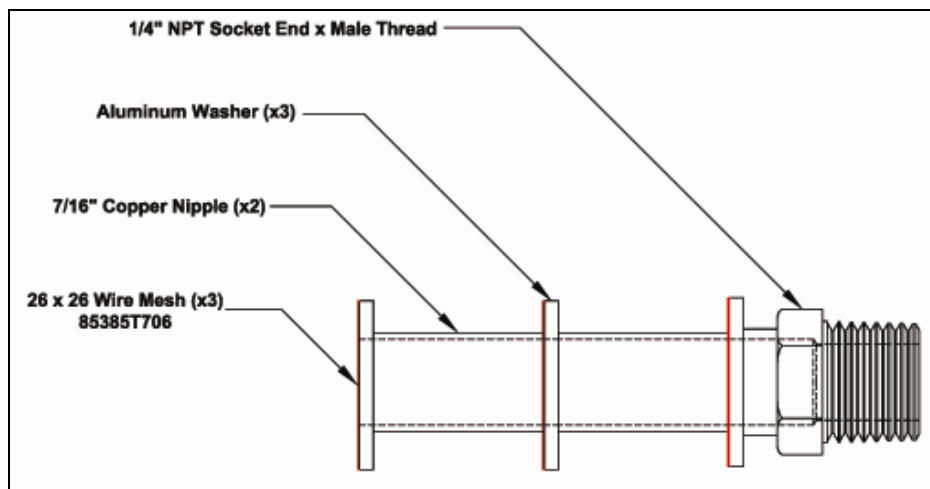


Figure 5.6: Mesh Nozzle

5.5 Evaluating the Electrostatic Effects of Mechanical Agitation

Experiments conducted without the aid of the mechanical wipers show significant buildup of NanoActive™ MgO on the walls of the aerosol generator. The buildup can be seen in Figure 5.7. This buildup raised significant questions about the operation of the aerosol generator and the charge of the NanoActive™ MgO powder. Electrostatic cohesive and adhesive forces induced by the aerosol generator had the potential to influence the outcome of the experiment. The experiments would not be an accurate representation of other dispersion applications if these forces were created by the aerosol generation device. Particle charge measurements were conducted to rule out any influence of the aerosol generator on aerosol particle size.



Figure 5.7: Aerosol Generator Buildup (Without Mechanical Wipers)

5.5.1 Experimental Setup

The Dynamic Faraday-Cage Sampler, built in the Kansas State University Air Movement Laboratory (AML), was used to determine the charge-to-mass ratio of NanoActive™ MgO dispersed by the aerosol generator designed for this study. This device was modeled after a similar device described in Murtomaa (2005). The schematic of the electrostatic charge measurement device is shown in Figure 5.8.

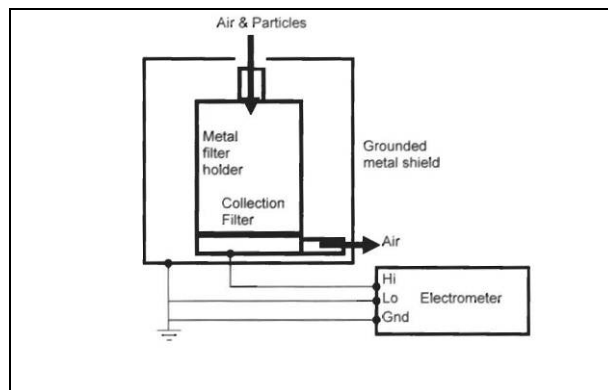


Figure 5.8: Dynamic Faraday Cage Sampler Schematic (Taken from AML Handout)

The device consists of a glass fiber filter held in place by a metal filter holder and backup metal screen. The filter holder is connected to an electrometer that measures the accumulation of charge on the sample collected by the filter. The filter is weighed before

and after the experiment. The charge-to-mass ratio is then calculated. The metal shield simply protects the sample and experiment from the influence of external fields.

A picture of the components is shown in Figure 5.9. The actual device is shielded by two metal cylinders. The filter holder components can be seen connected to the sampling pump and electrometer. The sampling tube is extended vertically from the top of the device through the bottom of the sampling chamber.



Figure 5.9: Dynamic Faraday Cage Sampler Components



Figure 5.10: Aerosol Sampling Chamber

The sampling tube was inserted through the bottom of the chamber shown in Figure 5.10. The top of the sampling tube was placed flush with the bottom of the chamber. The aerosol generator and pressure control apparatus was placed outside the chamber as shown in Figure 5.11. The experimental aerosol generator setup and pressure control can be seen in more detail in Chapter 9.



Figure 5.11: Aerosol Generator and Pressure Control Apparatus

5.5.2 Charge-to-Mass Ratio Data

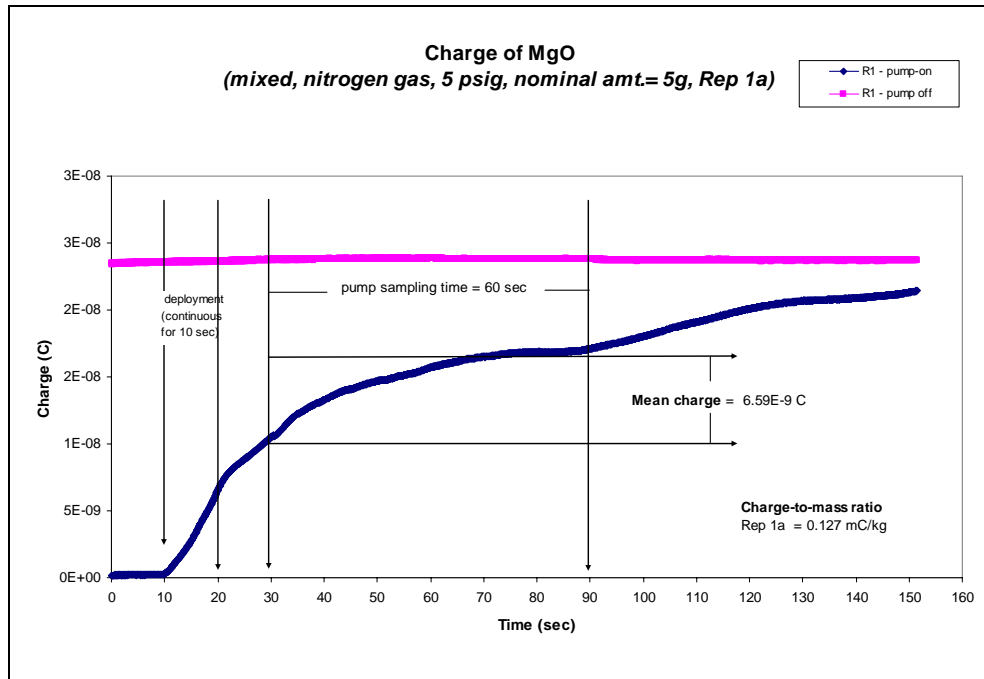


Figure 5.12: NanoActive™ MgO Charge vs. Time: Trial 1, Mixed

The data shown in Figure 5.12 illustrates the collection of charge in the prototype Faraday Cage Sampler versus time. The mixing device in the aerosol generator was turned on one minute prior to the beginning of the experiment. Data collection began at time $t=0$. At $t=10$ s the aerosol was deployed by opening the ball valve from the compressed nitrogen tank. At $t=20$ s the aerosol was shut off by closing the ball valve from the tank. The sampling pump was then turned on after an additional ten seconds and ran for a total of 60 seconds. The experiment was terminated at $t=160$ s. The bottom curve in the figure is the experimental curve. The flat curve, top, is data taken after the experimental run to verify no additional charge was acquired since the pump was off. The charge-to-mass ratio for this run was 0.127 mC/kg. This value was calculated by dividing the charge measured during the 60 s sampling time by the total mass of particulate collected on the filter.

The initial charge at the start of sampling, $t=30$ s, is not zero. The accrual of charge in the Faraday Cage Sampler prior to sampling is apparently due to the presence of a flow

field within the sampling chamber. Other experiments using fire extinguisher apparatus show similar phenomena due to the high initial velocities within the chamber. This is the reason sampling began ten seconds after the termination of flow of the aerosol.

The mixed experiment was duplicated with half the amount of NanoActive™ MgO in the aerosol chamber. The data for the second mixed experiment is shown in Figure 5.13. Since the number concentration of particles was less, fewer particles were collected in the sampler. Thus, the mean charge and mass collected is less than the first trial. The charge-to-mass ratio was 0.103 mC/kg in the second trial with half the mass of the first. The two values for charge-to-mass ratio average to 0.115 mC/kg.

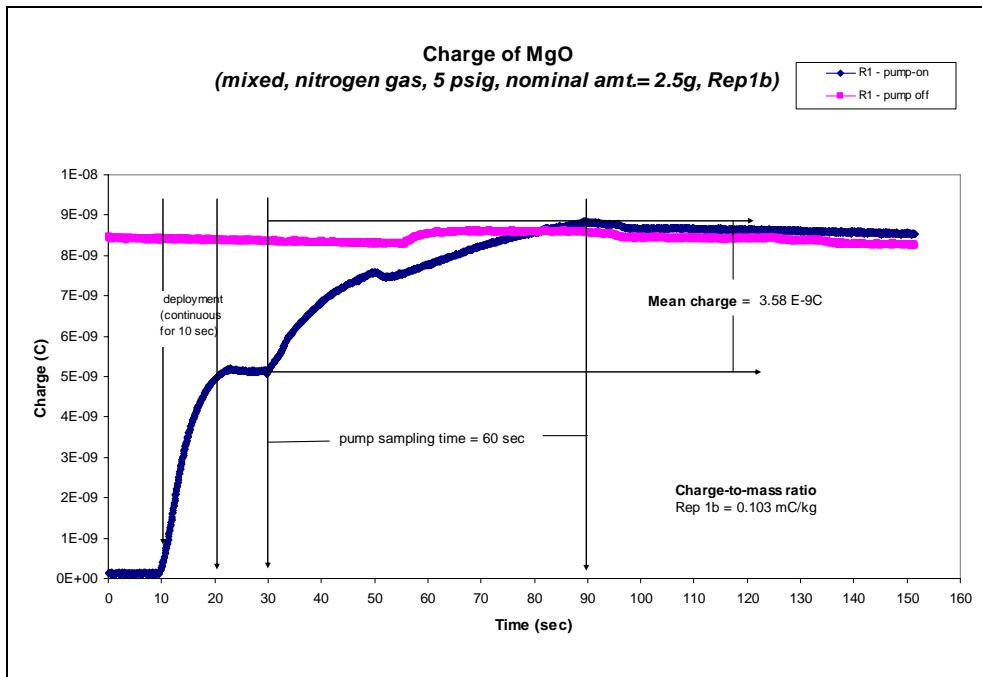


Figure 5.13: NanoActive™ MgO Charge vs. Time: Trial 2, Mixed

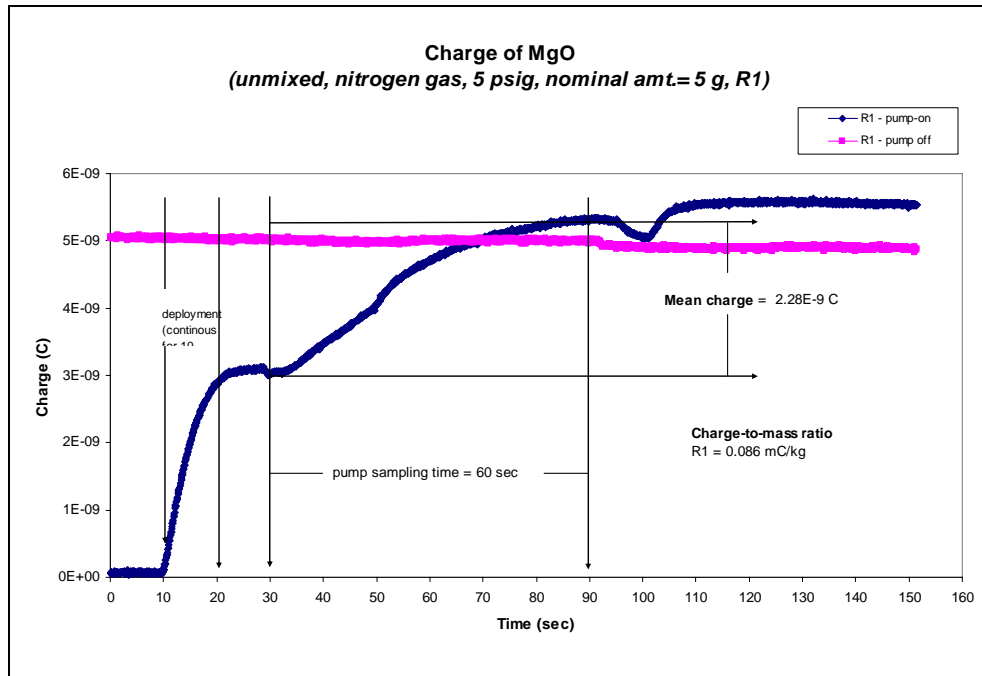


Figure 5.14: NanoActive™ MgO Charge vs. Time: Unmixed

Figure 5.14 shows the data collected when the experiment was conducted without the aid of the stirring mechanism. The time sequence for this run was similar to that of the two previous experiments. The aerosol was deployed ten seconds after the start of data collection, run for 10 seconds, and then shut off. Ten seconds then elapsed before the sampling pump was turned on. The charge-to-mass ratio for the unmixed NanoActive™ MgO aerosol was 0.086 mC/kg. This ratio is less than the average mixed ratio 0.115 mC/kg, but not substantially less.

Data collected by Susan Castro of the Biological Engineering Department shows that a tribo-charging device used for powder paints can be used to give an NanoActive™ MgO aerosol a charge-to-mass ratio very close to 1.0 mC/kg.

5.5.3 Conclusion

The electrostatic charge induced by the aerosol generator will be neglected considering the charge-to-mass ratios for mixed, unmixed, and aerosols charged by a tribocharging device. The values for mixed and unmixed aerosols differ by approximately 25%. The first experiment also shows approximately 10% difference between trials for mixed

aerosols. Both aerosols produced in the aerosol generator were charged to less than 12% of the aerosol charged by a tribo-charging device. The electrostatic charge induced by mixing in the aerosol generator is small relative to the potential charge induced by other devices. The main conclusion drawn from the data is the mixing mechanism in the aerosol generator does not significantly charge the aerosol particles. This data does not suggest anything about the electrostatic forces present between aerosol particles.

6 PARTICLE IMAGE VELOCIMETRY

6.1 Introduction

Particle image velocimetry (PIV) is an optical technique used to characterize fluid flows. Throwing a stick in a river is a rudimentary example of PIV. Qualitative conclusions about the flow of the river can be made by observing the motion of the floating stick. With the use of pulsed lasers, photo imaging equipment, and computers, quantitative data regarding speed and other characteristics can be collected from all types of flows in a laboratory setting. A schematic of how PIV works is shown in Figure 6.1.

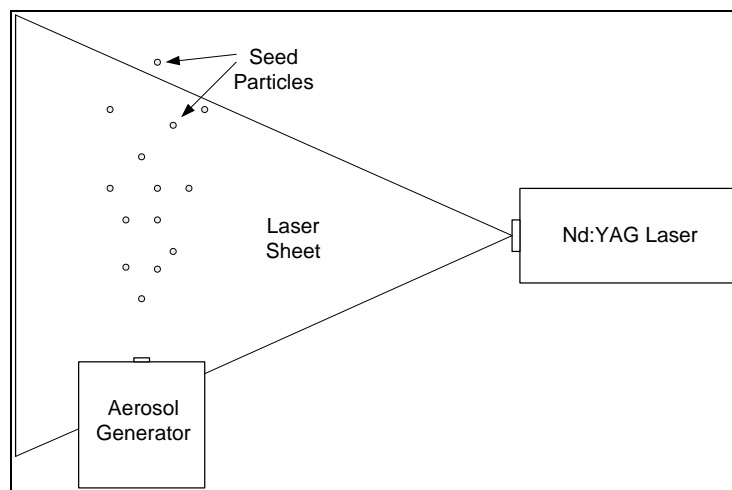


Figure 6.1: PIV Schematic

6.1.1 Seeding the Flow

To capture data about the flow there must be something that can be observed. The stick was the reference for observation in the rudimentary example previously mentioned. The flow is “seeded” in PIV measurements with particles. The particles are observed and conclusions are made about the flow from the motion of the particles. Seed particles are chosen based on two criteria, light scattering properties and inertial properties. Larger particles scatter more light. Higher intensity scattered light translates into higher resolution. However, large particles have more inertia, which makes them more likely to deviate from the streamlines of the flow. Thus, smaller particles are optimal when considering the accuracy to which their motion represents the motion of the fluid. In

most experimental works, 1 to 5 μm particles are used to satisfy the two constraints previously discussed.

6.1.2 Illuminating the Seed Particles

A pulsed laser sheet is used to illuminate the seed particles for observation. Most current PIV systems use a double pulsed Nd:YAG laser because of high amplification and good mechanical and thermal properties. Neodymium-doped yttrium aluminum garnet is the lasing medium in these lasers, hence the acronym Nd:YAG. The laser pulses are timed at specific intervals which illuminate the particles for imaging.

6.1.3 Imaging the Seed Particles

Calculations of flow field data are based on the relative locations of seed particles in successive images. Photographic film has been used in the past but digital cameras have become the imaging tool of choice because of their high resolution and operational speed. Pictures are taken on the order of 10-15 Hz. The images are then analyzed by computer to gather information regarding the flow.

6.1.4 Post Processing

Successive images are compared to track relative locations of groupings of seed particles. This is called cross-correlation. Two successive PIV images are shown in Figure 6.2. The distances the particle moved, dx and dy , are greatly exaggerated for illustration purposes.

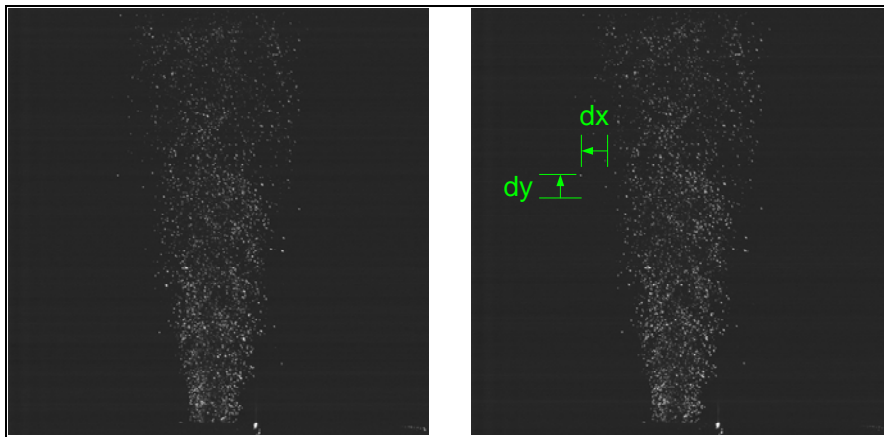


Figure 6.2: Successive PIV Images

The time between frames is known. The displacement of the particle grouping is determined and instantaneous velocities are calculated.

The Hart cross-correlation is a commonly used recursive correlation algorithm in PIV (Hart 1999). A recursive algorithm takes a sub region of the image and the peak velocity is determined. That datum is stored and the sub region is further broken down into smaller regions which are correlated again for their peak velocities. Basic knowledge of the flow provided by the initial correlation aids the correlation process at higher resolutions by providing some rough idea of where the particles are headed. This allows for greater probability of success in tracking particle groups at higher resolutions. The recursive correlation process is continued until the spatial resolution is near the size of the particles. Hundreds of images are collected, the velocities at each point in the flow are calculated for each successive set of images, and the data are combined to provide an average velocity at each point in the flow.

6.2 Experimental Setup

The PIV laboratory setup, including Nd:YAG laser, digital camera, and aerosol generator, is shown in Figure 6.3.

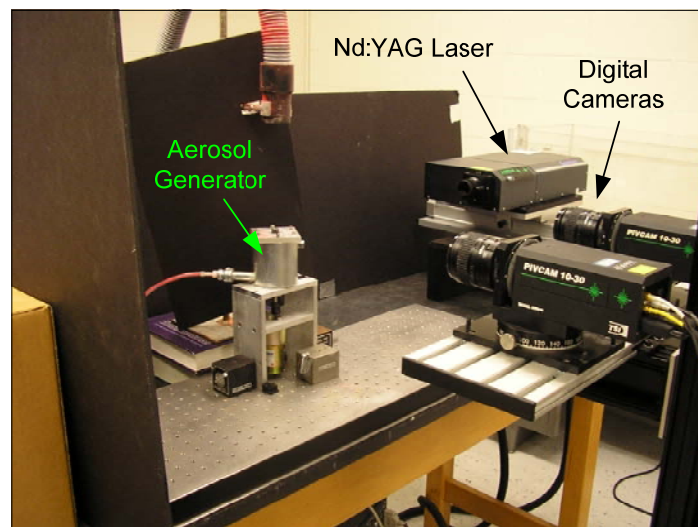


Figure 6.3: PIV Laboratory Setup

6.2.1 Seed Particles

Pro-Tec red fluorescent powder paint particles were used to seed the flow. These particles possess special optical properties that are useful in PIV. The Nd:YAG laser wavelength is 532 nm. When the paint particles are illuminated they reemit light with a wavelength of 604.5 nm. A special filter on the digital camera lens eliminates any light with wavelengths less than 600 nm. Only the light scattered by the particles is seen in the images with the use of these particles and optical filter. The average particle diameter was in the 10-13 μm range.

6.2.2 Imaging

The digital cameras are shown in Figure 6.3. Two cameras are available for imaging but only one was used. The use of two cameras allows for three dimensional flow characterization. The camera lens was 0.5 m away from the aerosol generator giving an image resolution was 60 μm per pixel. The imaging rate was 15 Hz.

6.2.3 Post Processing

The images were analyzed and cross-correlated using the Hart Algorithm. The spot size or interrogation area was 32 x 32 pixels. Validation was performed twice to remove any vectors outside four standard deviations from the mean.

6.3 Data

6.3.1 Velocity

The velocities at each point of the abrupt orifice flow field were measured for pressures ranging from 0.5 to 3.5 psi at increments of 0.5 psi. The PIV calculations base the velocity off of measured values for the speed in the x and y directions. The velocity magnitude is given by

$$U = \sqrt{u^2 + v^2}, \quad (6.1)$$

where u is the velocity in the x-direction and v is the velocity in the y-direction. Velocity contour plots for pressures of 0.5 to 3.0 psi can be found in Appendix B. Maximum velocities for pressures from 0.5 to 3.5 psi can be found in Table 6.1.

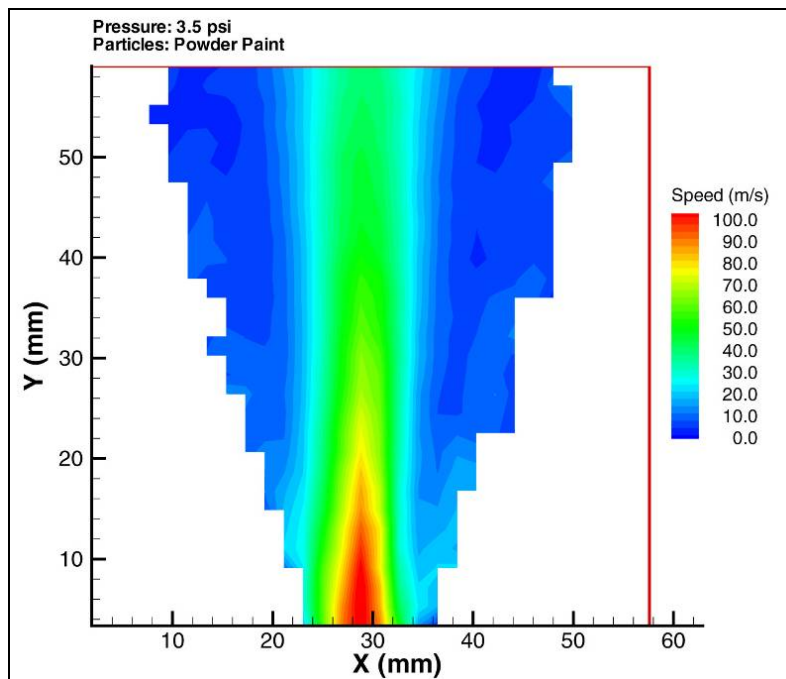


Figure 6.4: PIV Velocity Plot for Abrupt Orifice at 3.5 psi

The data shown in Figure 6.4 are in the mid-plane of the jet. Therefore, the x and y directions are analogous to the radial and axial directions in cylindrical coordinates. The measured data will not be written in cylindrical coordinates because CFD data presented in later sections will be presented in Cartesian Coordinates as well.

6.3.2 Turbulent Kinetic Energy

Turbulent Kinetic Energies were computed using the variance of the velocities in the x and y directions. Turbulent flow can be thought of as small, high frequency velocity fluctuations superimposed on the mean motion of the flow. The mean flow of the jet is in the y direction, but at any one point in the flow, the velocity may change rapidly in all directions. The fluctuations in the velocity field were used to compute the turbulent kinetic energy. The variance of the velocity was calculated from the PIV velocity data. The variances were then used to calculate the turbulent kinetic energy, given by

$$k = \frac{1}{2} (S_u^2 + S_v^2). \quad (6.2)$$

Figure 6.5 shows the contour plot of turbulent kinetic energy for the abrupt orifice operating at 3.5 psi. Data for pressures ranging from 0.5 to 3.0 psi can be found in Appendix B and maximum turbulent kinetic energies can be found in Table 6.1.

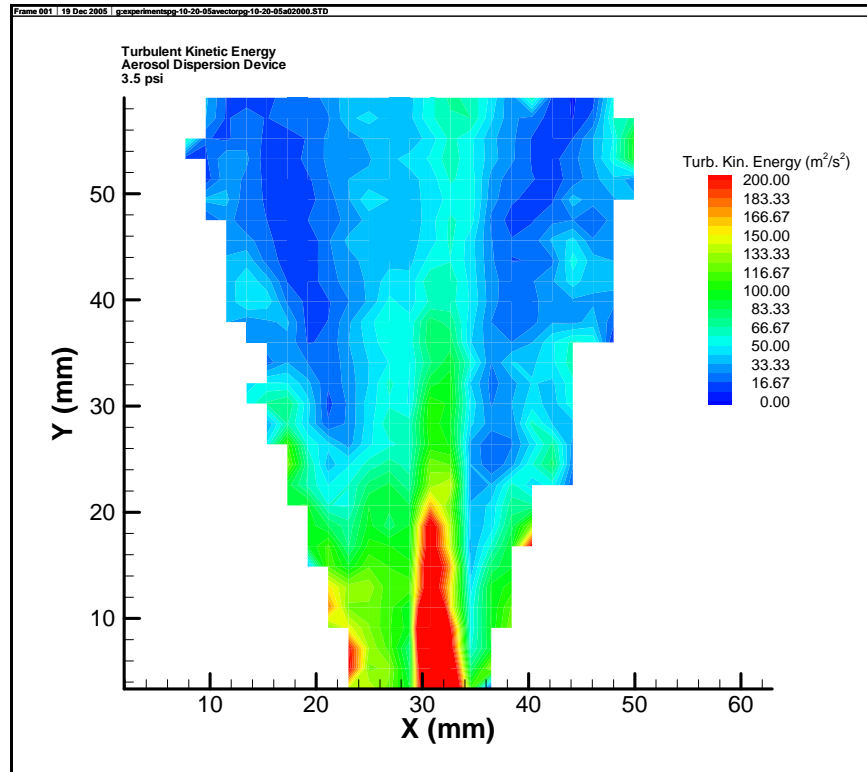


Figure 6.5: PIV Turbulent Kinetic Energy Plot for Abrupt Orifice at 3.5 psi

6.3.3 Shear Stress

The viscosity of a fluid relates the rate of deformation of a small element in the fluid to the shear stress. The shear stress acting in the plane whose normal is in the x direction and acts in the y direction is given by

$$\tau_{xy} = \tau_{yx} = \mu \left(\frac{\partial v}{\partial x} + \frac{\partial u}{\partial y} \right). \quad (6.3)$$

The partial derivative of the velocity in the x direction with respect to y is much less than the partial derivative of the y velocity with respect to x. This relation between the relative magnitudes was determined from experimental data. This relation simplifies Equation 6.3 to

$$\tau_{xy} = \tau_{yx} = \mu \left(\frac{\partial v}{\partial x} \right). \quad (6.4)$$

Figure 6.6 shows the shear stress contours for abrupt orifice flow at 3.5 psi. Shear stress plots for pressures ranging from 0.5 to 3.0 psi are given in Appendix B and maximum shear stress values can be found in Table 6.1.

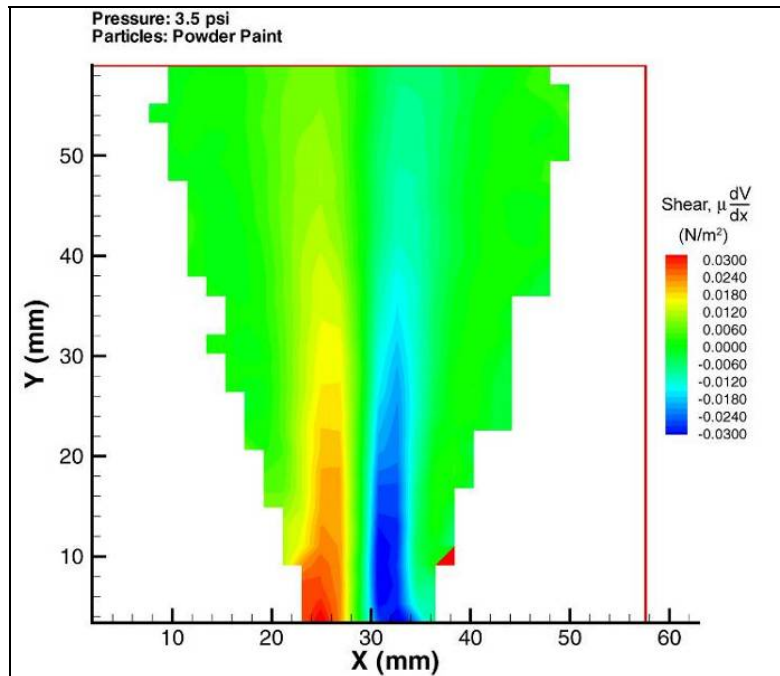


Figure 6.6: Shear Stress for Abrupt Orifice at 3.5 psi

6.4 PIV Data Summary for Abrupt Orifice

The maximum values for velocity, turbulent kinetic energy, and shear stress are given in Table 6.1. The maximum velocities range from 30 to 106.3 m/s. The maximum turbulent kinetic energy ranges from 60 to 481.9 m^2/s^2 . Although the turbulent kinetic energies for 3.0 and 3.5 psi seem to be outliers, the choice code for each measurement was greater than 100. This means the 481.9 m^2/s^2 measurement represents the average of over 100 measurements taken from a point at approximately $(x,y)=(30 \text{ mm}, 7 \text{ mm})$. The data shows a drop in turbulent kinetic energy from 3.0 to 3.5 psi. The choice code for this measurement is also very high. Neither measurement should be dismissed even though the results seem peculiar. The fluctuation could possibly have been due to fluctuations in the pressure from the pressure control device or some other experimental factor. The maximum shear stress values are calculated using Equation 6.4. This equation neglects the influence of Turbulent Reynolds Stresses. The peak velocity increases with pressure but the surrounding air remains still, increasing the shear stress.

Table 6.1: Summary of PIV Data for Abrupt Orifice

PIV DATA FOR ABRUPT ORIFICE			
Pressure (psi)	Maximum Velocity (m/s)	Maximum Turbulent Kinetic Energy (m^2/s^2)	Maximum Shear Stress (N/m^2)
0.5	30	58.9	1.19E-02
1.0	28.5	97.2	1.48E-02
1.5	48.9	146.7	1.76E-02
2.0	56.5	239.2	2.08E-02
2.5	74.5	227.3	2.90E-02
3.0	87.2	481.9	3.05E-02
3.5	106.3	431.6	3.32E-02

7 CFD SIMULATIONS

Fluent simulations were performed to determine the respective values of maximum acceleration, strain, and turbulent energy dissipation rate for the abrupt orifice, converging, and converging-diverging nozzles. Fluent is a computational fluid dynamics package that uses a control volume based finite difference method to model fluid flows. Fluent models flows by solving the conservation of mass, energy, and momentum equations. Gambit version 2.2.30 was used to create and mesh the model geometries used in the CFD simulations. Fluent version 6.2.16 was then used to run the simulations. All simulations were three dimensional.

7.1 Nozzle Model Data

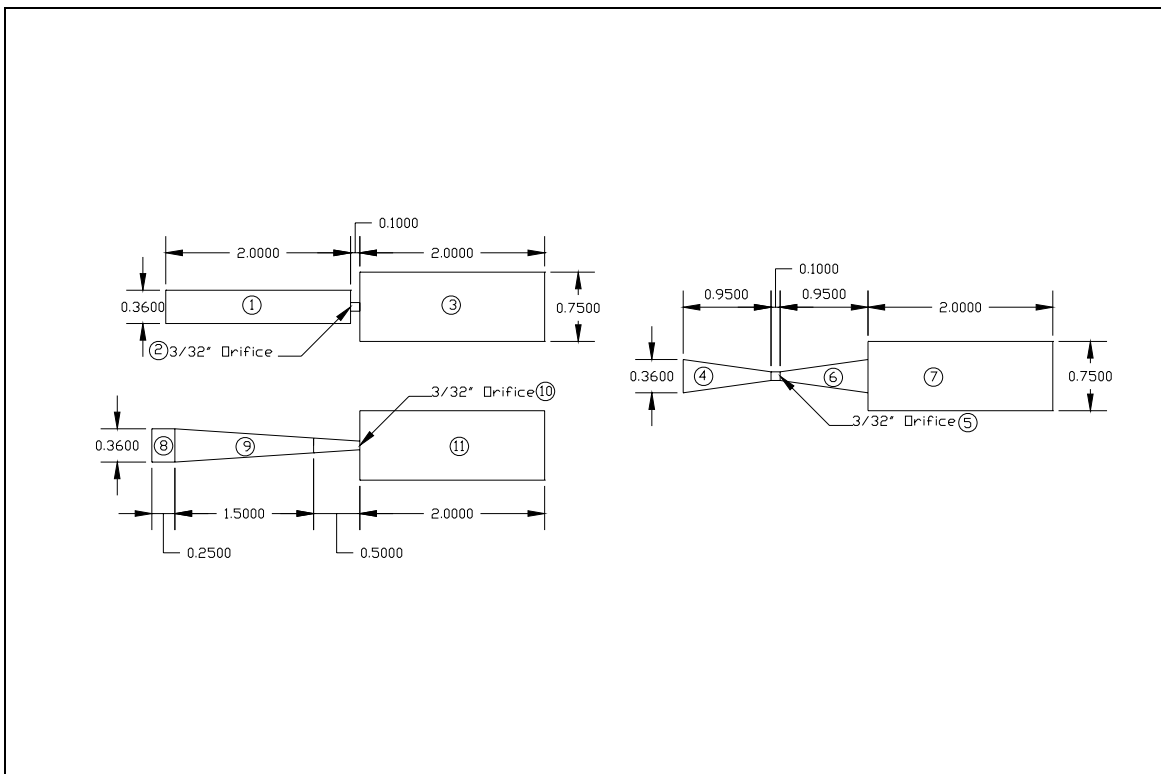


Figure 7.1: Model Geometries Created in Gambit

Figure 7.1 shows the nozzle models used in FLUENT simulations. All dimensions in Figure 7.1 are in inches. The model meshes were entirely comprised of hexahedral elements. The mesh intervals and total number of elements in each section of each model

are listed in Table 7.1. The boundary conditions at the inlet and outlet faces were set as constant pressure boundaries.

Table 7.1: Gambit Mesh Description

Nozzle Type	Segment	Mesh Interval	Number of Elements
Abrupt Orifice	1	0.025	81972
	2	0.005	6460
	3	0.035	128470
			216902
Converging-Diverging Nozzle	4	0.035	45795
	5	0.005	18060
	6	0.035	45795
	7	0.035	97920
			207570
Converging Nozzle	8	0.04	7552
	9	0.04	45312
	10	0.007	33984
	11	0.04	144126
			230974

7.2 Simulation Setup

Fluent version 6.2.16 was used to simulate the flows in the three nozzles. The single precision 3d model was used rather than the double precision model to save computation time and memory.

7.2.1 Operating Conditions

Turbulent model k-epsilon was selected for the nozzle simulations. The k-epsilon model is the standard two equation model used for including viscous effects in the flow. This model has been used extensively in engineering practice for the last 20 years. The k-epsilon model is robust, economical, and reasonably accurate for a wide range of turbulent flows such as jet flow and duct flow. This model is semi-empirical. The constants used in the model were the default values in Fluent 6.2.16.

Gravity was considered as an operating condition for this simulation. A value of $g = -9.81 \text{ m/s}^2$ was used for the gravitational constant. The flow direction was assigned in the y-axis. All calculations will rely on this designation.

Air is the default material used in Fluent. No alterations to the material data were made for this simulation.

7.2.2 Boundary Conditions

Pressures were used as boundary conditions at the inlet and outlet. The inlet gage pressure was set at 0.5 psi (3446 Pa). The outlet boundary gage pressure was set to atmospheric 0 psi (0 Pa). When specifying the boundary pressure, one must also specify the turbulence. To do so the turbulence intensity and hydraulic diameter method was used. The turbulence intensity was left at 10% (default) and the diameters of the inlet and outlet were specified. The rest of the boundary was modeled as a solid with a no-slip boundary condition.

7.2.3 Initial Conditions

The initial values for pressure, x velocity, y velocity, z velocity, turbulent kinetic energy, and turbulent dissipation rate were all set to zero at the beginning of the simulation.

7.2.4 Convergence Criteria

To test for convergence, the residuals were monitored for the following variables: continuity, x velocity, y velocity, z velocity, kappa, and epsilon. The convergence criteria were that each of the variable residuals be less than 1E-5.

7.2.5 Incompressible Flow

It should be noted that these simulations assume incompressible flow. As the velocity approaches one-third of the speed of sound, this assumption fails. Therefore, at velocities close to 100 m/s, this model is less accurate than a model that considers compressibility.

7.3 Simulation Model Data

7.3.1 Velocity

Figure 7.2 shows velocity contours for the mid-plane of each nozzle configuration.

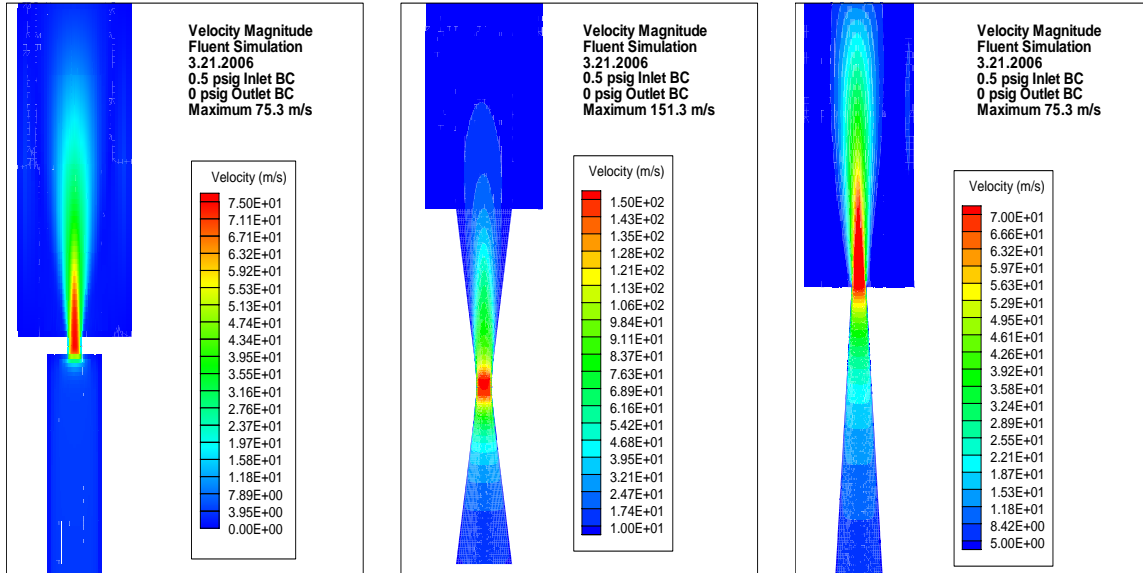


Figure 7.2: CFD Velocity Contour Plots

The peak velocities for the abrupt and converging nozzles are the same, 75.3 m/s. The maximum velocity for the converging-diverging nozzle is twice the value of either the abrupt orifice or converging nozzle. This can be explained via the Bernoulli equation. The following is the Bernoulli equation assuming negligible elevation change and incompressible flow.

$$\frac{P_1}{\rho} + \frac{V_1^2}{2} = \frac{P_2}{\rho} + \frac{V_2^2}{2} \quad (7.1)$$

The inlet and outlet pressures are the same for each nozzle simulation. The Bernoulli equation states the change in velocity difference should be the same for any given pressure difference. The geometry of the converging-diverging nozzle makes it different from the other nozzles. In the converging-diverging nozzle, the pressure at the 3/32” diameter section is not atmospheric pressure as in the other models. In the converging-diverging nozzle, atmospheric pressure is downstream of the 3/32” section. The velocity in the converging-diverging nozzle would be 75.3 m/s at the section where the pressure is

equal to atmospheric. The continuity equation then implies the velocity must be higher at the 3/32” section due to a reduction in area.

7.3.2 Verification

CFD velocity data were compared to measurements made with Particle Image Velocimetry to verify the accuracy of the simulations. Figure 7.3 shows the velocity profile of the abrupt orifice jet at height of $y = 15$ mm (according to PIV axes) for a pressure of 0.5 psi. PIV velocity data for 0.5 psi can be seen in Figure B.1. The data for this height above the orifice were plotted as a function of x (mm). A slice from the CFD data was then plotted over the velocity measurements for the same height. Excellent agreement between simulation and measurement is seen in Figure 7.3. This provides reassurance that information provided by CFD simulations is accurate.

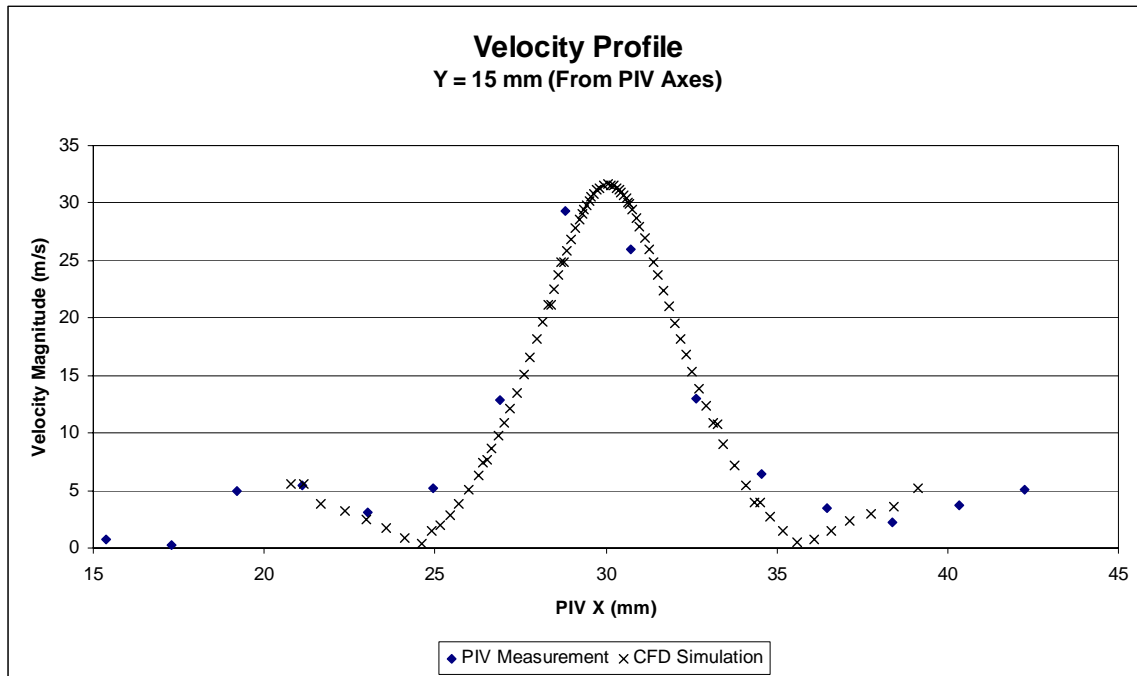


Figure 7.3: CFD Verification through Comparison with PIV Velocity

7.3.3 Acceleration

The magnitude of acceleration in the Cartesian coordinate system is given by

$$a = \sqrt{a_x^2 + a_y^2 + a_z^2} . \quad (7.2)$$

The material derivative can be used to find the components of acceleration. The steady-state components of acceleration are given by

$$a_x = \frac{Du}{Dt} = u \frac{\partial u}{\partial x} + v \frac{\partial u}{\partial y} + w \frac{\partial u}{\partial z}, \quad (7.3)$$

$$a_y = \frac{Dv}{Dt} = u \frac{\partial v}{\partial x} + v \frac{\partial v}{\partial y} + w \frac{\partial v}{\partial z}, \quad (7.4)$$

$$\text{and } a_z = \frac{Dw}{Dt} = u \frac{\partial w}{\partial x} + v \frac{\partial w}{\partial y} + w \frac{\partial w}{\partial z}. \quad (7.5)$$

The components of acceleration given by Equations 7.3, 7.4, and 7.5 were calculated from Fluent model data. The contour plots for acceleration in each nozzle are shown in Figure 7.4.

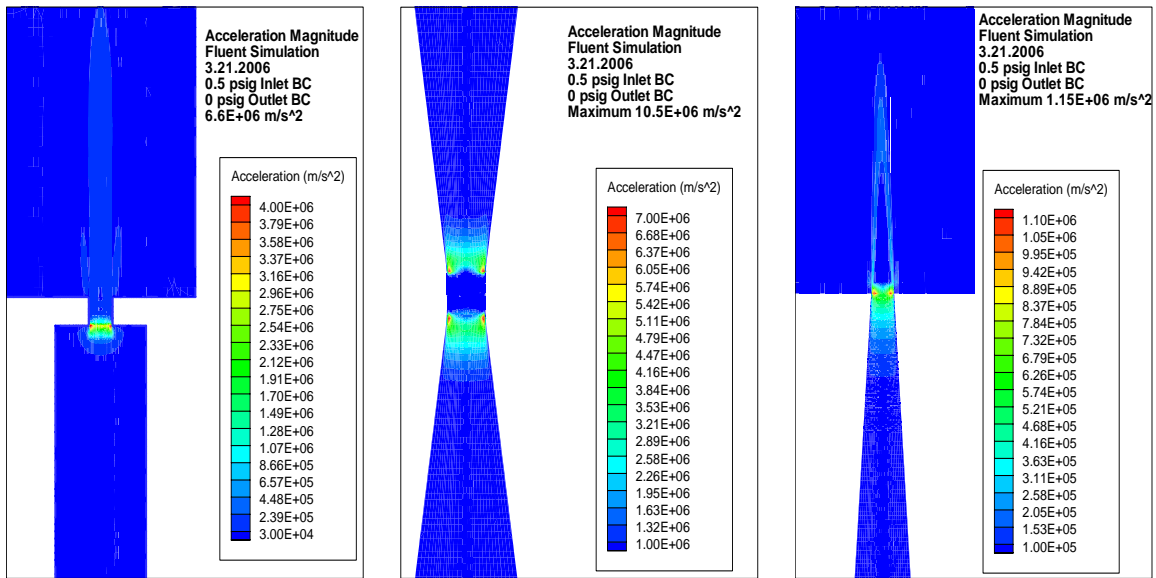


Figure 7.4: Acceleration Contour Plots

The results from the CFD simulations suggest the fluid accelerations in each of these nozzles are of the same order of magnitude. The converging-diverging nozzle has the highest acceleration at 10.5E6 m/s². It should be noted the Fluent model assumes incompressible flow. In the case of the converging-diverging nozzle this is a bad assumption since the velocity is greater than one-third the speed of sound.

7.3.4 Scale Invariance

The mesh sizes used in each of the model geometries were changed to determine if the meshing algorithm significantly affected the results for velocity and acceleration. These results are shown in Table 7.2. The velocities and accelerations varied slightly with an increase and decrease in mesh number. This implies we did not reach grid independence in these simulations. However, for the purposes of this study and calculations made in proceeding sections, the differences will be considered negligible. Mesh A models will be used in all proceeding calculations.

Table 7.2: Dependence of Velocity and Acceleration Based on Mesh Size

Nozzle Type	Mesh A			Mesh B		
	Total Number of Elements	Maximum Velocity (m/s)	Maximum Acceleration (m/s ²)	Total Number of Elements	Maximum Velocity (m/s)	Maximum Acceleration (m/s ²)
Abrupt	216902	75.3	6.60E+06	60098	73.8	4.00E+06
Converging	230974	75.4	1.15E+06	551730	75.2	1.70E+06
Converging Diverging	207570	151.3	1.05E+07	84356	144.3	6.90E+06

7.3.5 Shear Stress

The shear stresses in each nozzle were calculated from Fluent Simulation data. The shear stresses on a fluid element are given by the following three equations.

$$\tau_{xy} = \tau_{yx} = \mu \left(\frac{\partial v}{\partial x} + \frac{\partial u}{\partial y} \right) \quad (7.6)$$

$$\tau_{yz} = \tau_{zy} = \mu \left(\frac{\partial w}{\partial y} + \frac{\partial v}{\partial z} \right) \quad (7.7)$$

$$\tau_{zx} = \tau_{xz} = \mu \left(\frac{\partial u}{\partial z} + \frac{\partial w}{\partial x} \right) \quad (7.8)$$

The shear stress acting on the face perpendicular to the x-axis, in the y-direction, is denoted τ_{xy} . The components of the velocity in the x,y, and z directions are given by u,v, and w, respectively. The viscosity of the fluid is represented by μ . For air, $\mu = 1.81 \cdot 10^{-5} Pa \cdot s$.

Figures 7.5, 7.6, and 7.7 show all three components of shear stress for each nozzle design. The maximum value listed on each figure seems higher than the observed values from the contour plots. A search of the simulation data failed to reveal where these points were located. They will be considered anomalies and the maximum values will be read from the contour plots.

Figure 7.5 shows all three components of shear stress for the abrupt orifice. The highest stress component is τ_{xy} at 2.0 Pa. The other two stress components are on the order of 0.1 Pa and 0.05 Pa.

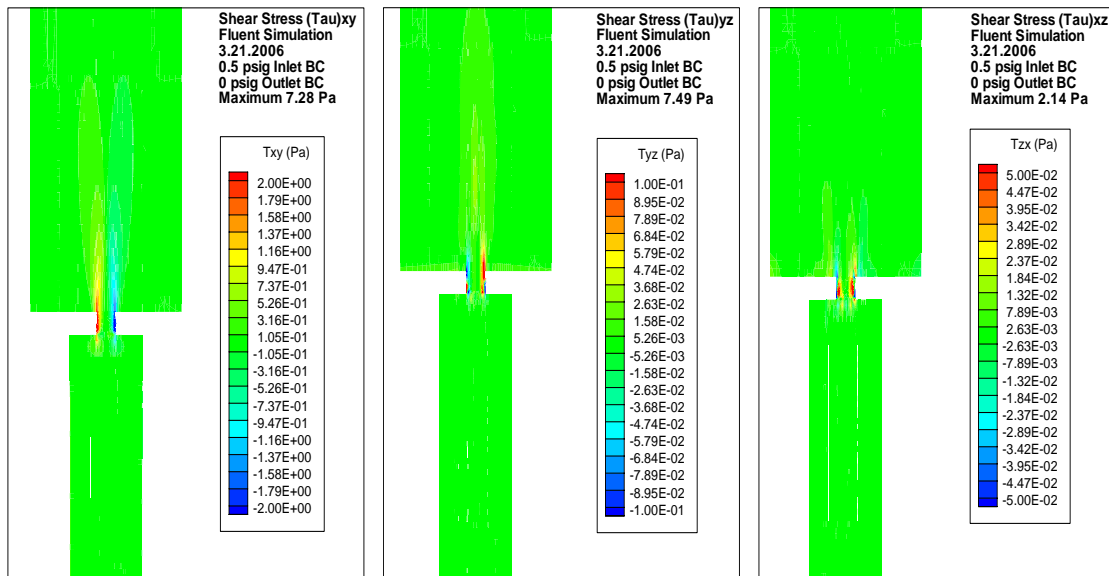


Figure 7.5: Shear Stress Contour Plots for Abrupt Orifice

The shear stress components for the converging-diverging nozzle are shown in Figure 7.6. The maximum stress is τ_{xy} at 2.0 Pa.

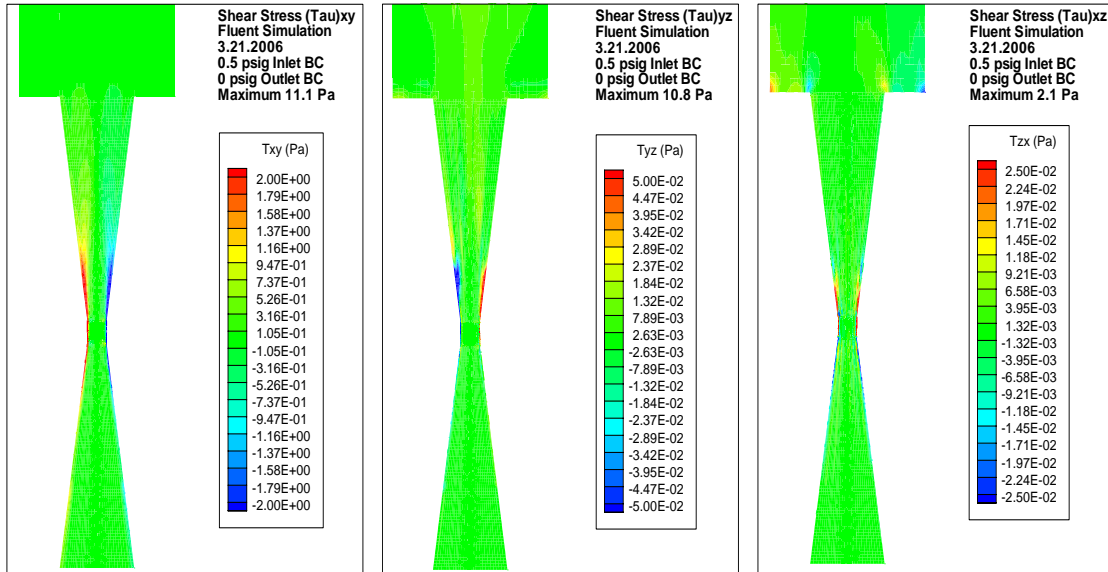


Figure 7.6: Shear Stress Contour Plots for the Converging-Diverging Nozzle

Figure 7.7 shows the shear stress components in the converging nozzle. The maximum shear stress is approximately the same as the other two cases, $\tau_{xy} = 2.0$ Pa.

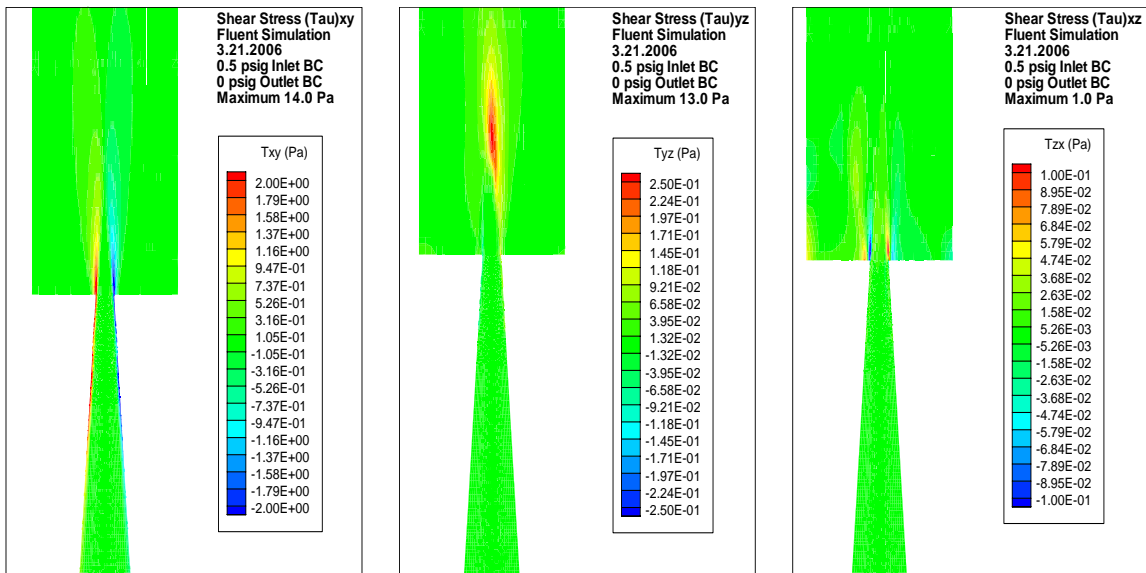


Figure 7.7: Shear Stress Contour Plots for Converging Nozzle

7.3.6 Strain Rate

The strain rates were calculated by FLUENT from Equation 7.9 and are shown in Figure 7.8.

$$S^2 = \left[\frac{\partial u}{\partial x} \left(\frac{\partial u}{\partial x} + \frac{\partial u}{\partial x} \right) + \frac{\partial u}{\partial y} \left(\frac{\partial u}{\partial y} + \frac{\partial v}{\partial x} \right) + \frac{\partial u}{\partial z} \left(\frac{\partial u}{\partial z} + \frac{\partial w}{\partial x} \right) \right] + \left[\frac{\partial v}{\partial x} \left(\frac{\partial v}{\partial x} + \frac{\partial u}{\partial y} \right) + \frac{\partial v}{\partial y} \left(\frac{\partial v}{\partial y} + \frac{\partial v}{\partial y} \right) + \frac{\partial v}{\partial z} \left(\frac{\partial v}{\partial z} + \frac{\partial w}{\partial y} \right) \right] + \left[\frac{\partial w}{\partial x} \left(\frac{\partial w}{\partial x} + \frac{\partial u}{\partial z} \right) + \frac{\partial w}{\partial y} \left(\frac{\partial w}{\partial y} + \frac{\partial v}{\partial z} \right) + \frac{\partial w}{\partial z} \left(\frac{\partial w}{\partial z} + \frac{\partial w}{\partial z} \right) \right] \quad (7.9)$$

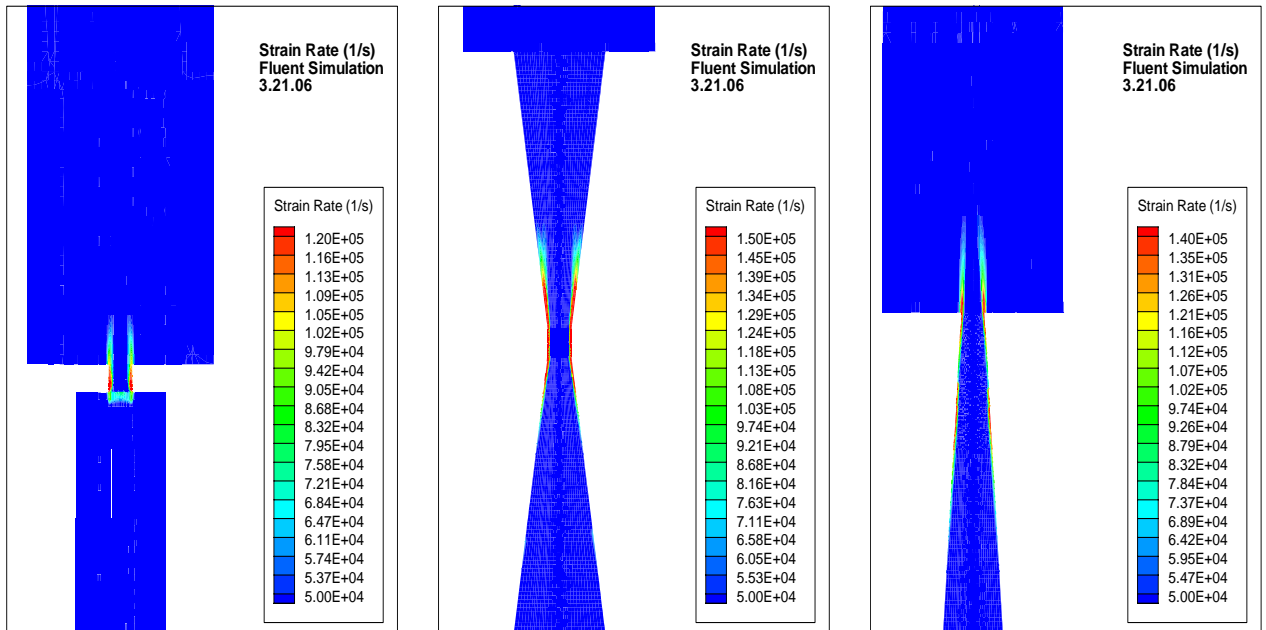


Figure 7.8: Strain Rate Contour Plots

The strain rates seen in Figure 7.8 will be used in later sections to calculate theoretical stresses in particles and aggregates in shear flow.

7.3.7 Turbulent Energy Dissipation Rate

The turbulent energy dissipation rate, ε , is often used to describe turbulent flows.

Contour plots for the energy dissipation rates of the three experimental nozzles are shown in Figure 7.9. The values of maximum turbulent energy dissipation rate will be used in later sections to calculate theoretical maximum stresses in particles in turbulent flow.

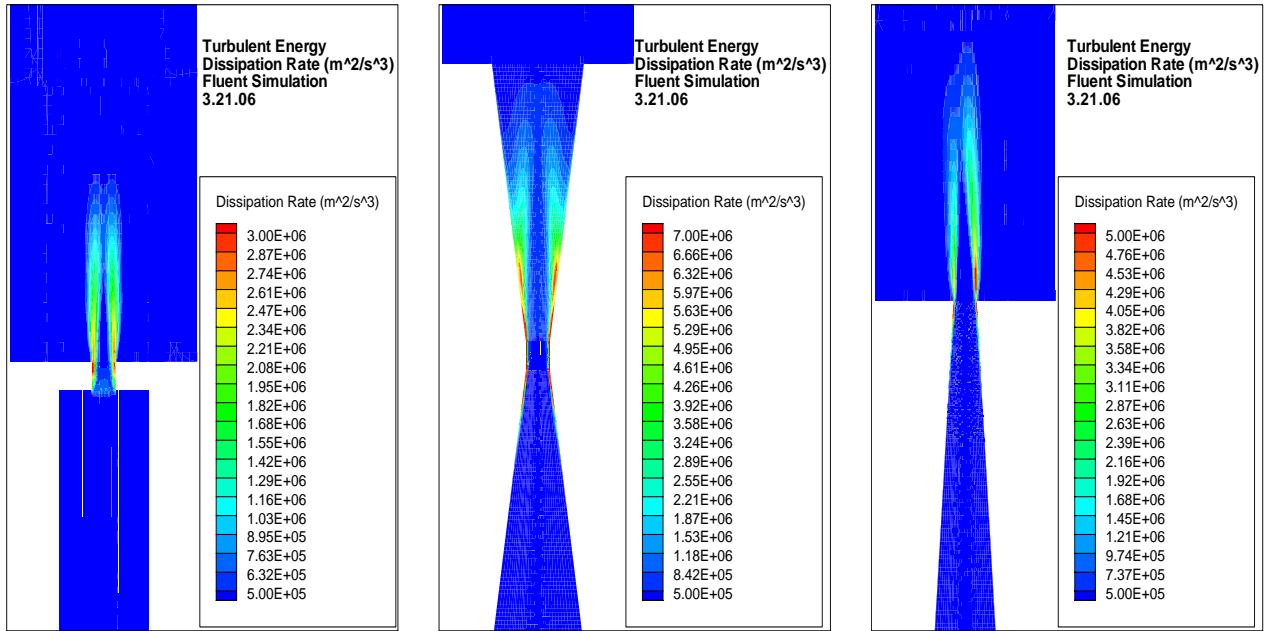


Figure 7.9: Turbulent Energy Dissipation Rate Contour Plots

7.4 Conclusions

CFD simulations were run to calculate the maximum accelerations, strain rates, and turbulent energy dissipation rates in each of the deaggregation nozzles. PIV data show excellent agreement with the velocity profile produced by the simulation of the abrupt orifice. This agreement provides some assurance that the simulated data are correct. Values found from the simulations will be used to calculate theoretical deaggregation stresses in the Discussion Chapter.

8 LIGHT SCATTERING REVIEW

8.1 Review of Electromagnetic Waves

Maxwell was the first to introduce the idea that all electric and magnetic phenomena could be described by four governing equations of electric and magnetic fields. This revolutionary set of equations lead to the theory that light could be described by an electromagnetic wave, shown in Figure 8.1. These electromagnetic waves are produced by oscillating electric charges, i.e. accelerating charges, and consist of an electric field oscillating in the xy plane and a magnetic field oscillating in the xz plane. The cross product, $\vec{E} \times \vec{B}$, gives the direction of propagation of the wave.

According to Maxwell, a magnetic field will be produced from a changing electric field. If a changing magnetic field produces an electric field, that electric field must be changing as well. The changing electric field will then produce another changing magnetic field and so on. Maxwell's conclusion was that the net result of these changing fields was to produce a wave of magnetic and electric fields that propagates through space.

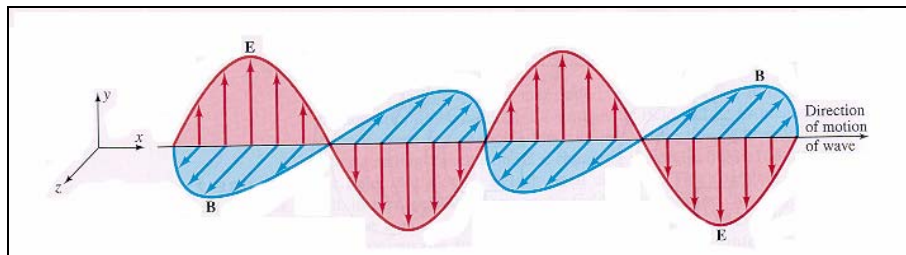


Figure 8.1: EM Wave Diagram (Taken from Giancoli 1998)

It is important to note that energy is transported by waves. That energy is proportional to the amplitude of the wave squared. Thus, the intensity of the wave is also proportional to the amplitude of the wave squared.

8.2 Light Scattering

Light is an electromagnetic (EM) wave. This principle is the basis for all light scattering phenomena. A schematic representation of a light scattering event is presented in Figure

8.2. When a particle is struck by the oscillating electric field of the incident EM wave the electrons of that particle are set into oscillatory motion. Since EM waves are produced by accelerating charges, the particle struck by the incident EM wave then emits another EM wave. The wave reemitted by the particle is referred to as the scattered wave.

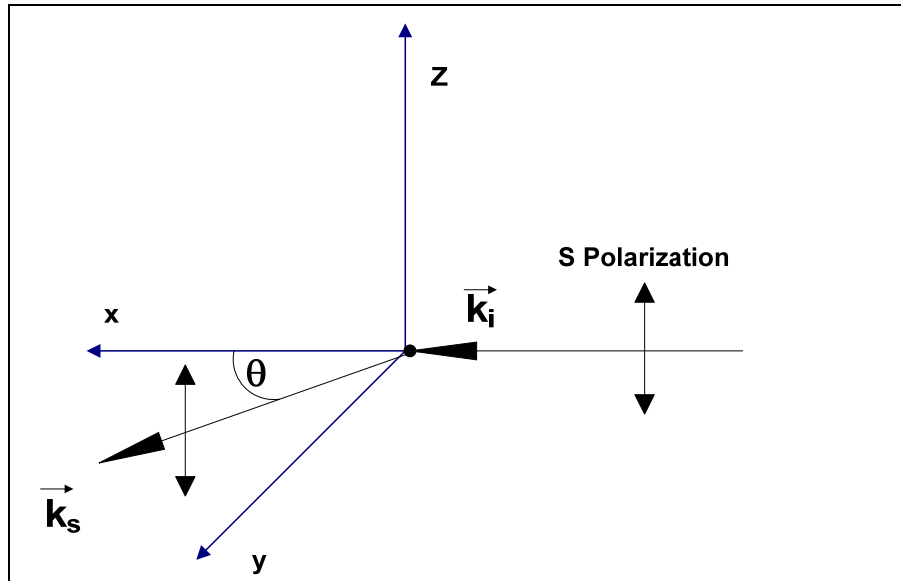


Figure 8.2: Light Scattering Diagram

The interaction between the incident wave and the particle is considered elastic, therefore, $|\vec{k}_s| = |\vec{k}_i|$. Since most experimental detectors lie within the xy plane, only the scattered light in the xy plane with vertical polarization will be considered. Polarization will be presented in more detail in the next section. The angle between the scattered wave and the incident wave is denoted θ and is called the scattering angle.

8.2.1 Polarization

As seen in Figure 8.2, the incident and scattered waves are polarized. In laboratory experiments the vertical or s-polarization is important because lasers produce vertically polarized light. Light from the sun or a source like a light bulb is unpolarized, meaning the EM waves sent from the source have many orientations. If a wave is polarized the orientation of the wave is fixed. In Figure 8.2 the vertical polarization is denoted by an arrow lying within the xz plane. In vertically polarized light there is no electrical wave

component in the y direction. Light can be polarized in any orientation with optical devices called polarizers. The incident light polarization is often set by optics or the laser. The scattered wave polarization can be found by taking the projection of the incident polarization on a plane perpendicular to the scattered wave vector \vec{k}_s . In Figure 8.2 the scattered and incident polarizations are both vertical.

8.2.2 Relative Particle Size

A simple, relative measure of particle size is made when light scattering techniques are employed. The circumference of the particle compared to the wavelength of light is the dimensionless term called the size factor, α , and is given by

$$\alpha = \frac{2\pi r}{\lambda}. \quad (8.1)$$

The size factor is simply a comparison of the two length scales involved in the light scattering event.

8.3 Scattering Cross Section

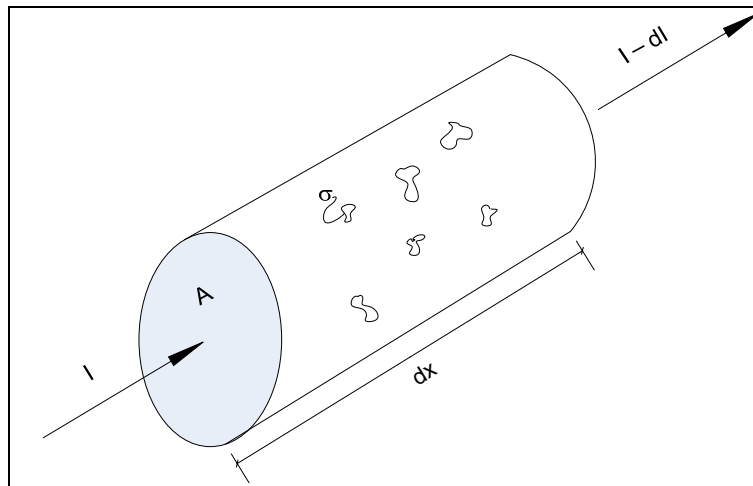


Figure 8.3: Scattering Cross Section Diagram

Figure 8.3 illustrates the idea of a scattering cross-section. There is some incident intensity, I , applied to the cross sectional area, A . Exiting the differential element is the incident intensity minus some differential intensity lost to extinction. If dx is taken to be very small, there will be no overlap between particles in the viewing area. Taking a

projected image, looking down the axis of the cylinder, N particles with area σ would be seen by the incident light. The attenuation factor, dI , is proportional to the probability of the light hitting a particle and is given by

$$dI = I \frac{N\sigma}{A}. \quad (8.2)$$

Dividing both sides by dx gives,

$$\frac{dI}{dx} = I \frac{N\sigma}{Adx}, \quad (8.3)$$

an equation for the derivative of the intensity with respect to x . Since $A dx$ is the volume of the differential element, the above equation simplifies to one involving the number concentration, n . The attenuation is noted by adding the negative sign since the intensity weakens with x .

$$\frac{dI}{dx} = -In\sigma \quad (8.4)$$

Solving the first order differential equation yields the Lambert-Beer Law,

$$I(x) = I_0 e^{-n\sigma x} \quad (8.5)$$

In this example σ is the scattering cross section. In experimental light scattering studies the scattered intensity is measured over the entire range of solid angles.

8.3.1 Measurement of Particle Size

The sizes of simple shapes like spheres and cubes are easy to define. Very rarely are particles perfect spheres or cubes though. Most naturally occurring particles are rough; they are not easily defined by one characteristic dimension like radius to a sphere. The radius of gyration, denoted R_g , is used to characterize the size of non-spherical particles and is given by

$$R_g^2 = \frac{\int \rho(\vec{r})(\vec{r} - \vec{r}_{cm})^2 d\vec{r}}{\int \rho(\vec{r}) d\vec{r}} \quad (8.6)$$

where the density of the particle at position \vec{r} is $\rho(\vec{r})$ and \vec{r}_{cm} is the position of the center of mass. The radius of gyration can be considered a root mean-square-radius that accounts for odd shaped and anisotropic particles.

8.3.2 Differential Scattering Cross Section

The differential scattering cross section, $d\sigma/d\Omega$, is defined as the power scattered per unit solid angle for a given incident intensity,

$$\frac{P_{scattered}}{\Omega} = \frac{d\sigma}{d\Omega} I_o. \quad (8.7)$$

The intensity of light scattered is the power scattered divided by the area of the detector,

$$I_{scattered} = \frac{P_{scattered}}{A_{detector}}. \quad (8.8)$$

Using the definition of a solid angle, $\Omega = A/r^2$, the intensity of the scattered light simplifies to

$$I_{scattered} = I_o \frac{d\sigma}{d\Omega} \frac{1}{r^2}. \quad (8.9)$$

The intensity of scattered light is proportional to the differential scattering cross section.

The differential scattering cross section in the forward direction is shown in Figure 8.4. If the differential scattering cross section is plotted versus the radius of gyration on a log-log plot, a transition is noticed at $\rho=1$. The phase shift parameter, ρ , is a material property and is explained in more detail in the section that discusses Rayleigh-Debye-Gans Scattering. The differential scattering cross section in the forward direction is proportional to the R^6 for $\rho < 1$ and R^4 for $\rho > 1$. The forward direction is defined as the angle corresponding to λ/R_g for a given scatterer and the wavelength of light, λ . The forward direction is analogous to the diffraction lobe seen in a single-slit diffraction pattern.

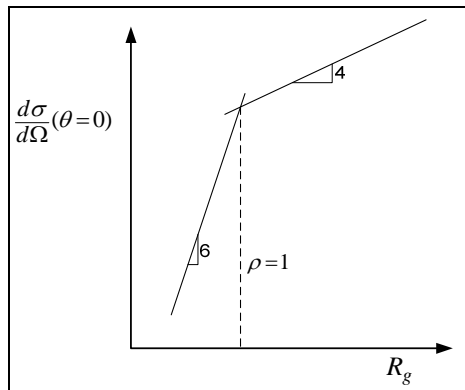


Figure 8.4: Scattering Cross Section in the Forward Direction

8.3.3 Rayleigh Scattering

If the particles are small with respect to the wavelength of light, i.e. $\alpha \ll 1$, the scattering results are simple. These results are referred to as Rayleigh Scattering. The electromagnetic field may be assumed uniform across the entire volume of the particle since the particle is small. Each differential element of the particle will be incident to the same phase of light. They will also emit light in the same manner, in phase. The scattered light from each element adds constructively at the detector. Hence, a proportional relationship between the amplitude of the light and the volume of the particle exists. The intensity measured by the detector is proportional to the square of field amplitude, therefore, the intensity is a function of the volume of the particle squared.

The differential scattering cross section for Rayleigh Scattering is given by

$$\frac{d\sigma}{d\Omega} = k^4 a^6 \left| \frac{m^2 - 1}{m^2 + 2} \right|^2 \quad (8.10)$$

where k is the magnitude of the incident wave, $k = 2\pi / \lambda$, a is the radius of gyration of the particle, and m is the relative index of refraction of the particle with respect to the surrounding medium. Plugging Equation 8.10 into Equation 8.9 gives

$$I_{scattered} = \frac{k^4 a^6}{r^2} \left| \frac{m^2 - 1}{m^2 + 2} \right|^2 I_o, \quad (8.11)$$

and substituting for k ,

$$I_{scattered} = \frac{16\pi^4 a^6}{\lambda^4 r^2} \left| \frac{m^2 - 1}{m^2 + 2} \right|^2 I_o. \quad (8.12)$$

For Rayleigh Scattering, the scattered intensity is independent of scattering angle θ . Equation 8.12 shows the inverse relationship between the scattered intensity and the wavelength of the incident light to the fourth power. This means that incident waves with lower wavelengths such as blue will scatter light with a higher intensity than that scattered from a higher wavelength light like red. Lastly, the scattering is proportional to the volume of the particle squared. This can be seen by the a^6 factor in Equation 8.12. The Tyndall effect is a direct result of the size dependence. It states that for a group of

particles with constant mass, the scattered intensity will increase as the particles aggregate.

8.3.4 Rayleigh-Debye-Gans Scattering

Rayleigh scattering holds true if $\alpha \ll 1$, all subvolumes of the particle see and emit light of the same phase. In Rayleigh-Debye-Gans (RDG) scattering, as long as the phase of the light passing through the particle does not change significantly with respect to the phase of the light traveling through the surrounding medium, the scattering results can be simplified. The phase shift parameter, ρ , is a dimensionless parameter that quantifies the difference in phase between an EM wave that travels through a particle and one that travels through the surrounding medium. As long as $\rho < 1$, the simplifying assumptions can be made regardless of particle size. The phase shift parameter is given by

$$\rho = 2\alpha |m - 1|, \quad (8.13)$$

and substituting the expression for the size factor further reduces the equation to

$$\rho = \frac{4\pi r}{\lambda} |m - 1|. \quad (8.14)$$

Two significant results arise when the phase shift parameter is considered small. The RDG scattering cross section is the same as the Rayleigh scattering cross section when $\theta = 0$. The scattered light is also more intense in the forward direction. This trait becomes more pronounced as the particle gets larger.

8.3.5 Mie Scattering

The two forms of light scattering previously mentioned, Rayleigh and Rayleigh-Debye-Gans, make simplifying assumptions due to small size parameter or small phase shift parameter. For arbitrary particles, these assumptions cannot be made, therefore Maxwell's equations must be solved exactly. Solving these equations can prove to be very difficult for arbitrary shapes, thus, the particles are considered simple spheres in this review to make the analysis simpler.

In the past, plots of intensity vs. θ have been used to look for scattering trends. More recent work by Sorensen and Fischbach (2000) suggest the use of the scattering wave

vector, q , as the independent variable. The scattering wave vector is defined as the difference in incident and scattered waves,

$$\vec{q} = \vec{k}_i - \vec{k}_s. \quad (8.15)$$

The magnitude of the scattering wave vector is given by

$$q = 2k_i \sin\left(\frac{\theta}{2}\right). \quad (8.16)$$

Finally, plugging in the magnitude of the incident wave vector,

$$q = \frac{4\pi}{\lambda} \sin\left(\frac{\theta}{2}\right). \quad (8.17)$$

The most notable characteristic about the scattering wave vector is that it is the inverse length scale of the experiment. Analysis using q rather than θ is referred to as q -space analysis.

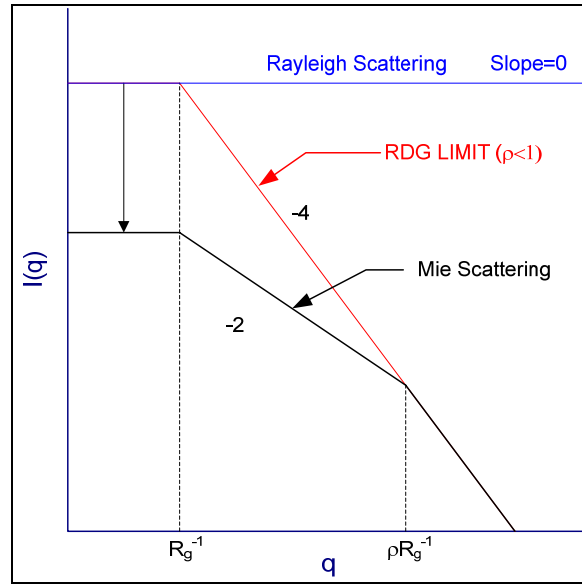


Figure 8.5: Patterns In Rayleigh, RDG, and Mie Scattering

There are three distinct regions for Mie scattering if $\rho > 1$:

$$I(q) \propto q^0 \text{ for } 0 < q < R_g^{-1} \quad (8.18)$$

$$I(q) \propto q^{-2} \text{ for } R_g^{-1} < q < \rho R_g^{-1} \quad (8.19)$$

$$I(q) \propto q^{-4} \text{ for } q > \rho R_g^{-1} \quad (8.20)$$

The horizontal section for $q < R_g^{-1}$ is called the Rayleigh Regime because the intensity does not vary with q . The region in which the slope changes from 0 to -2 is called the Guinier Regime and follows the relation

$$I(q) = I_0 \left(1 - q^2 R_g^2 / 3\right). \quad (8.21)$$

Equation 8.21 is called the Guinier Equation and holds true for $qR_g < 1$. The most important fact about the Guinier Equation is the radius of gyration of the scatterer may be determined from the inverse of q where the transition takes place. Assuming qR_g is small, Equation 8.21 may be rewritten in the form

$$I(q) = I_0 \left(1 + q^2 R_g^2 / 3\right)^{-1}. \quad (8.22)$$

Equation 8.22 will also be called the Guinier Equation since it is merely an algebraic transformation of 8.21. It should be noted that the Guinier Equation is independent of the index of refraction. This is convenient in practice when the optical properties of particles are unknown.

Equation 8.22 is true for non-fractal aggregates. For fractal aggregates see the *Handbook of Surface and Colloid Chemistry* (Sorensen 2003).

After the Guinier Regime, the slope is -2 and is often referred to as the power law regime. Once $q > \rho R_g^{-1}$, the slope changes to -4. The q^{-4} dependence is referred to as Porod's Law.

Figure 8.5 shows two distinctly different trends for the scattered intensity. If $\rho = 0$, the conditions for RDG scattering are met. Once this constraint is violated, the Rayleigh Regime drops and the power law regime develops, both indicative of Mie Scattering. The line transitioning from a slope of 0 to -2 to -4 represents Mie scattering. There is an explanation for this fundamental shift in scattering trends.

As the particle or the phase shift parameter becomes larger, $\rho \neq 0$, the EM wave is not constant across the volume of the particle. Each differential sub-volume of the particle

does not contribute equally to scattering. The Ewald-Oseen extinction theorem suggests that only the sub-volumes near the surface contribute to the scattering when the phase shift parameter is non-zero (Sorensen and Fischbach 2000). This accounts for the change in light scattering trends from RDG to Mie Scattering.

8.3.6 Polydisperse and Nonspherical Scatterers

The previous Mie Scattering results were derived for a set of monodisperse spherical scatterers. In application, most particles are non-spherical and very few aerosol systems are monodisperse. For this reason caution must be taken when interpreting the light scattering data collected from a set of polydisperse non-spherical scatterers (Lumme 1998).

Berg et al. (2005) has shown that a system of scatterers with log mean standard deviation of 1.22 still follow the Mie Scattering Envelops shown in Figure 8.5. Little deviation from these envelops is seen in simulated light scattering data. This suggests moderate polydispersity does not significantly affect the trends seen in light scattering data. The implication of this is that polydisperse systems may be concluded monodisperse without proper consideration. For this reason all data suggesting monodispersity, i.e. data following Mie Scattering trends, will be termed quasi-monodisperse in this study. Polydispersity beyond this degree will be termed super-polydisperse. Theoretical patterns in light scattering have not been developed for super-polydisperse systems of scatterers.

Scatterers occurring by natural processes are generally non-spherical. Zerull et al. (1977) described the differences between scattering seen for non-spherical particles and theoretical Mie Scattering. Zerull found that for most geometries the light scattering trends seen for non-spherical scatterers followed that of their spherical counterparts in the forward direction, $\theta < \lambda / R_g$. However, this study shows large differences in scattering trends for mid range angles all the way to backscattering.

The first geometry studied by Zerull et al. (1977) was a smooth sphere bombarded by metal shavings to give some statistical roughness. No significant difference was seen between scattering from the rough spheres and the corresponding Mie Theory for smooth spheres. Cubical and Octahedral scatterers of small size, $\alpha < 17.9$, were found to deviate from Mie Theory at mid-range scattering angles. The authors also found that concave and convex particle scattering deviated from Mie Theory by as much as a factor of five for mid-range scattering angles although the backscattering intensity did not deviate as distinctly. One other key observation made by Zerull et al. was that sharp minima and maxima, i.e. scattering ripples, seen in the scattering data are smoothed out for randomly oriented irregular particles.

This study suggested that Mie Scattering is not a good scattering approximation for non-spherical particles outside the diffraction lobe.

9 LIGHT SCATTERING EXPERIMENTAL SETUP

Chapter 8 presented the information that can be gathered about an aerosol from the collection and analysis of its scattered light. This chapter will outline the equipment and experimental setup required to gather such information.

9.1 Equipment

Spectra-Physics Model 165 Argon Laser

w/ Model 265 Control Unit

Parker 15R110FC Pressure Regulator (0-30 psi)

Hewlett Packard Model HP 34907A Data Acquisition Unit

Hewlett Packard Model HP 6205C DC Power Supply

Setra Model 230 Pressure Transducer (0-25 psi)

Dayton 6K030D 1/3hp Motor (1725 rpm)

w/ Dayton Model 1C792 Blower (7 ¾")

Photo Diode Detector Built by KSU Electronics Lab

Hamamatsu S3902-512 Photo Diode Array

9.2 Laboratory Setup

9.2.1 Light Scattering

Ferri (1997) describes a small angle light scattering measurement device used for the characterization of many physical and chemical systems. The experimental small angle light scattering device used in this study was modeled after Ferri's device.

Figure 9.1 shows a schematic of the optical equipment used in the light scattering experiment. The laser is at a right angle with the rest of the equipment. A 45° mirror is used to redirect the beam. A 0.3% filter is placed after the mirror to reduce the intensity of the beam. The detector would be saturated by incident light without the filter. The subsequent variable polarizer allows further variable control of the beam intensity. Since the beam is vertically polarized, changing the orientation of the variable polarizer reduces the intensity. A vertical polarizer follows the variable polarizer to make sure only

vertically polarized light is incident upon the scatterers. Irises are used throughout the system to eliminate unwanted diffraction.

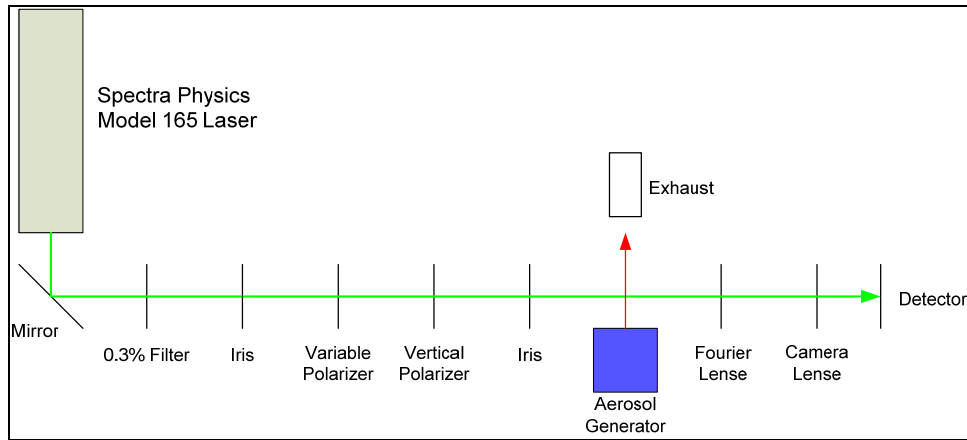


Figure 9.1: Laser Schematic

The equipment to the right of the aerosol generator is used to measure the intensity of scattered light. This equipment is further detailed in Figure 9.2. The combination of the Fourier and Minolta Camera Lenses provides “a one-to-one mapping between the intensity of the light scattered at different angles and the signals out from the corresponding pixels,” (Ferri 1997). For further information regarding optical calculations see Ferri (1997). Figure 9.2 shows the placing of each component in the system for the given lenses. These locations would differ depending on the focal lengths of the lenses used.

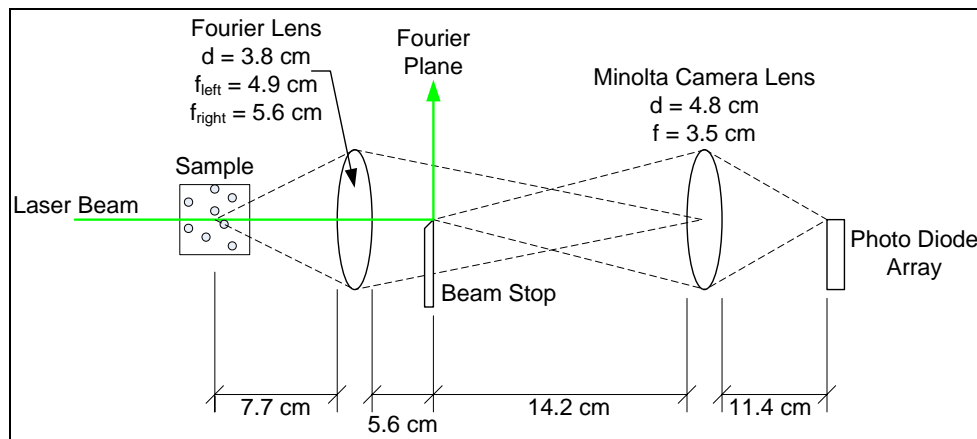


Figure 9.2: Scattered Light Measurement Apparatus

A beam stop is placed in-line with the incident beam to divert it away from the detector. The beam stop is a small drill bit, e.g. 1.5 mm, finely ground at a 45° angle. This ensures only scattered light is measured by the photo diode array. Only about 0.1% of the lowest angle scattering data are lost if care is taken to use only the very tip of the mirror to deflect the beam (Ferri 1997).

The output signal from the photo diode array is then presented in real time as Intensity vs. q . A Labview program was written by the designers of the photo diode array detector to display the data.

9.2.2 Aerosol Generation

A schematic diagram of the aerosol generation equipment is shown in Figure 9.3. All the components shown are incorporated to give some control over the aerosol generation process. A Parker pressure regulating valve is attached to the compressed air tank to control the pressure drop across the orifice. The pressure at the control valve is measured with respect to atmosphere by the Setra pressure transducer. The output of the pressure transducer is then sent to the HP Data Acquisition unit where it is converted to psi for viewing. The power supply in the figure powers the pressure transducer and the aerosol generator motor. A ground wire is attached to the aerosol generator to ensure the dissipation of any charge generated within the device.

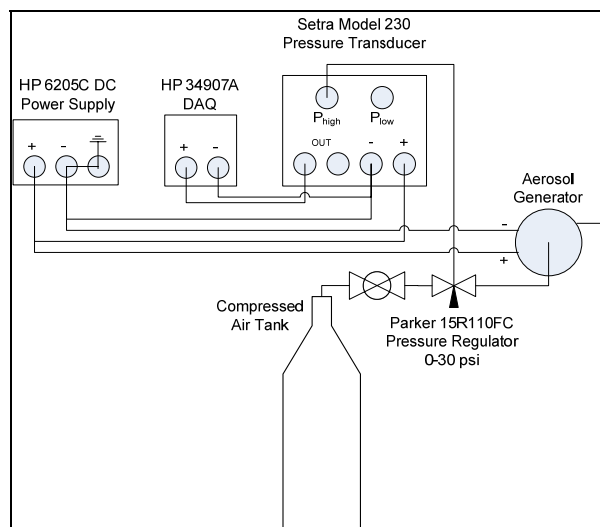


Figure 9.3: Aerosol Generation Equipment Schematic

The placement of the aerosol generator with respect to the laser beam is shown in Figure 9.4. The tip of the nozzle is placed 2.5 cm back from the beam and 8 cm in front of the Fourier Lens. A 4" flex hose is used to connect the blower to the exhaust port in front of the aerosol generator.

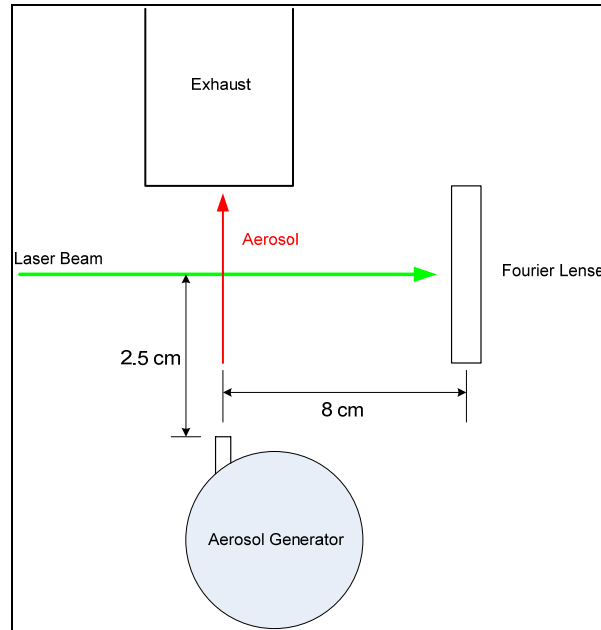


Figure 9.4: Position of Aerosol Generator

A picture of the experimental setup is shown in Figure 9.5. The DC power supply and data acquisition unit can be seen on the left. The aerosol generator and exhaust duct sit in front of the optical equipment. Following the aerosol generator are the Fourier and Minolta Camera Lenses. Lastly, on the far right, is the photo diode array detector.

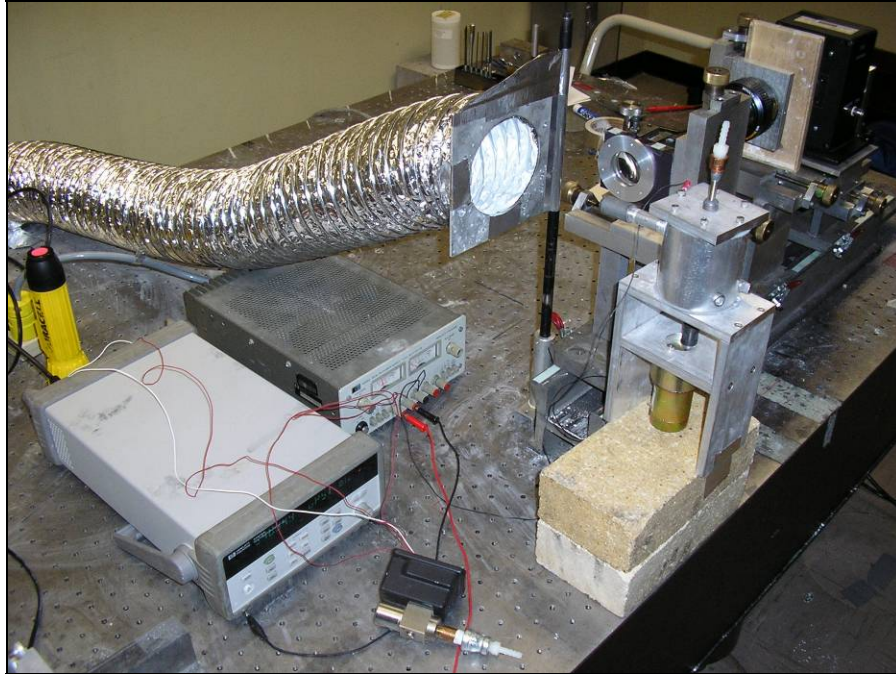


Figure 9.5: Picture of Experimental Setup

Additional experimental settings are shown in Table 9.1.

Table 9.1: Additional Experimental Settings

Laser Control Power	20 Watts
Laser Control Intensity	8
Laser Wavelength	488 nm
Aerosol Generator Motor Voltage	20 VDC
Pressure Transducer Excitation Voltage	20 VDC
DAQ Gain	5
DAQ Offset	Measured
Initial Mass of Powder	20 g

9.3 Calibration

The scattered light measurement device mentioned above can be calibrated through knowledge of diffraction patterns. Young's famous double slit experiment proved the wave nature of light by showing that a point source shown through a double slit gives constructive and destructive interference patterns. Similar phenomena can be seen for the diffraction of light through a single slit. In a single slit the maximum intensity occurs at $\theta = 0$ while minima occur corresponding to the relation

$$D \sin(\theta) = m\lambda, \quad (9.1)$$

where $m = 1, 2, 3, \dots$, D is the width of the slit, and λ is the wavelength of light.

A $10 \mu\text{m}$ single slit is placed at the position of scattering volume of the Fourier Lens for calibration purposes. Equation 9.1 is converted to q -space and plotted vs. the actual light scattering measurements made by the photo diode array detector. The physical locations of the components of the light scattering apparatus are adjusted until the theoretical curve fits the data. An example of this calibration can be seen in Figure 9.6. In this calibration, the light scattering data is accurate up to $q \approx 25,000 \text{cm}^{-1}$.

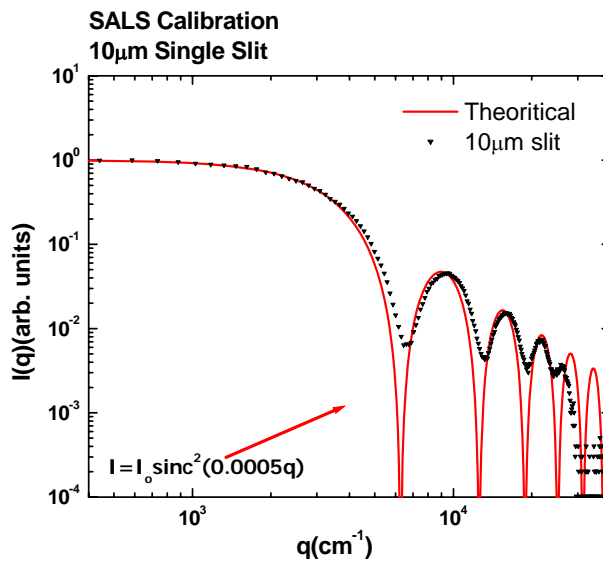


Figure 9.6: SALS Calibration Curve

10 LIGHT SCATTERING DATA

10.1 Data Normalization

One of the earliest experiments in this study focused on deaggregation as a function of distance from the orifice outlet. Figure 10.1 shows this relation. The pressure drop across the orifice was 20 psi in this data set. It can be seen in the figure that the peak intensity for various measurements were different. This difference is due to the dependence of light scattering on number concentration. The intensity of scattered light is proportional to the number of scatterers multiplied by the radius of gyration to the fourth power. This relation is applicable in the forward scattering lobe for scatterers with a phase shift parameter greater than 1. The major differences in scattering for the measurements are at high q . Therefore, to make better observations in these differences, each measurement is normalized to the peak intensity for that particular pressure. The peak intensity in Figure 10.1 is located at $q \approx 1000 \text{ cm}^{-1}$. Figure 10.2 shows the normalized measurements for the same data set. Light scattering data for various materials and nozzles will be displayed normalized from this point forward.

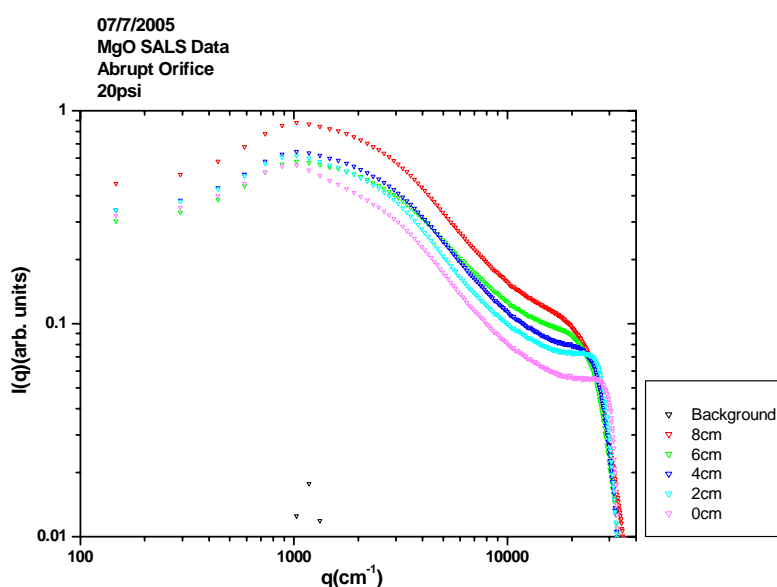


Figure 10.1: NanoActive™ MgO SALS Data as a Function of Distance from the Orifice

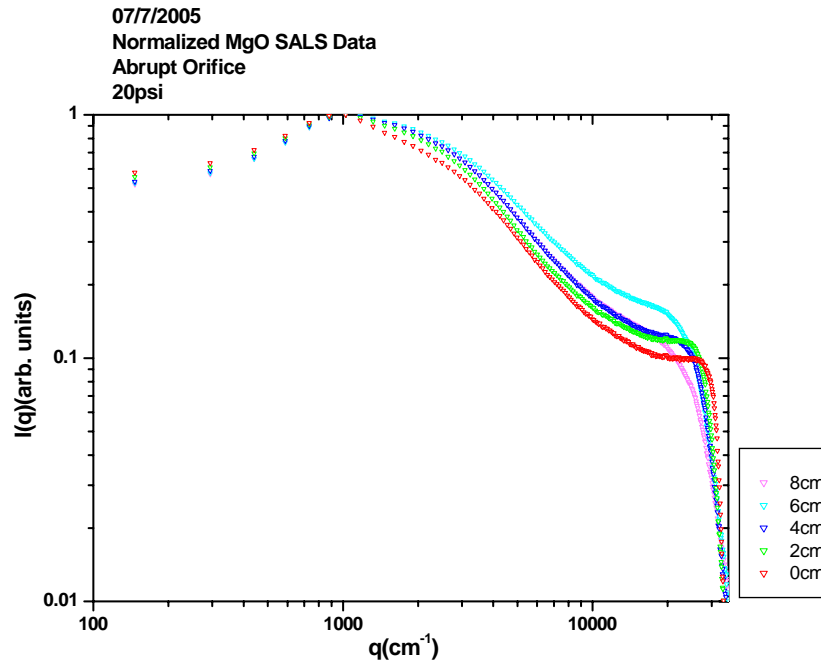


Figure 10.2: Normalized NanoActive™ MgO SALS Data as a Function of Distance from the Orifice

10.2 Bimodal Modeling of Small Angle Light Scattering Data

The data shown in Figure 10.2 do not fit within the Mie Scattering envelopes shown in Figure 8.5. It is reasonable to assume the aerosol is polydisperse. The presence of an inflection point is particularly odd. This characteristic of the measurements lends itself to the theory that the data could be bimodal. The first mode is of large particles, those larger than about 5 μm . The second mode is of particles on the order of 0.3 μm . When the light scattering data were modeled bimodal, the experimental data were fit quite accurately. All data in this study were fit by eye.

Figure 10.3 shows a bimodal fit for the light scattering data at the nozzle exit. Equation 8.22, the Guinier Equation, is used to approximate what the Mie scattering curves would look like for two monodisperse or quasi-monodisperse aerosols.

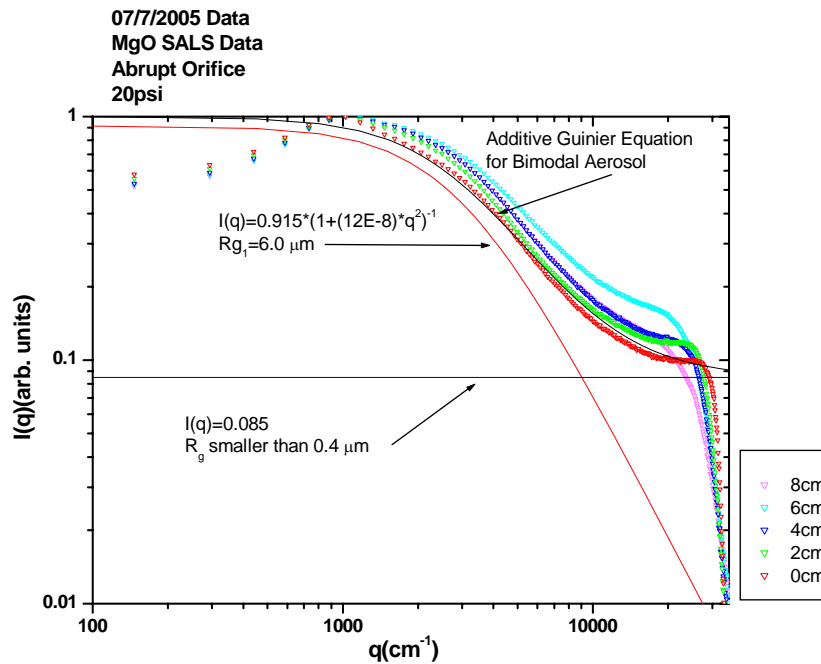


Figure 10.3: Bimodal Modeling of NanoActive™ MgO SALS Data

The Mie scattering envelopes shown in Figure 8.5 represent the light scattered from a system of scatterers of uniform size. In fact, if the size of the scatterers assumes a size distribution with a standard deviation on the order of 1.2, the Mie scattering envelopes still represent the scattered intensity of the system (Berg 2005). From this point forward, data resembling the Mie scattering curves will be referred to as quasi-monodisperse considering the inherent, yet small, variance in size from one particle to the next. The first quasi-monodisperse aerosol is modeled with respect to the first change in slope from 0 to -2 at $q \approx 1000 \text{ cm}^{-1}$, this is the large mode in the bimodal distribution assumed previously. The second quasi-monodisperse aerosol is approximated by a much smaller mode. It is difficult to approximate the size of the small mode due to limitations in the data collection device. The photo diode array does not allow for measurements to be taken beyond $q \approx 25,000 \text{ cm}^{-1}$ or $\theta \approx 11^\circ$. Referring to Figure 8.5, the Mie Scattering envelopes show that the slope changes from 0 to -2 at the radius of gyration of the particle. By assuming the radius of gyration of the smaller mode is less than the minimum size

that can be measured, $R_g = q_{\max}^{-1} = 0.4 \mu m$, the Mie Scattering curve for the small particles would be a flat line for all q in this experiment.

By varying the q^2 coefficient in the large mode Guinier Equation (e.g. 12E-8 from Figure 10.3), the overall coefficients in front of each Guinier Equation (e.g. 0.915 and 0.085), and adding the two equations, a fit can be obtained that closely resembles the actual data. Furthermore, the overall equation coefficients must add to one since the data is normalized. This can be more easily explained in the region of low q , $q < 1,000 \text{ cm}^{-1}$. Both equations are constant before the radius of gyration for the large mode particles is reached on the q scale. Thus, the normalization process imposes the constraint. By adding this constraint the coefficients become a scattering contribution ratio, termed in this study. In Figure 10.3, 91.5% of the light scattered comes from the large mode. Similarly, 8.5% of the light scattered comes from the particles of the small mode. These two values are simply the coefficients of the two Guinier Equations. The q^2 coefficient in the Guinier Equation is equal to $1/3 \cdot R_g^2$. From the coefficients, the radii of gyration can be computed. In this data set, the large mode is 6.0 μm and the small mode is below 400 nm.

This model suggests the presence of large particles in this NanoActive™ MgO aerosol, but even more significant is the scattering contribution from the small particles, assumed to be primary NanoActive™ MgO particles. Figure 8.5 shows the relation between the size of scatterers to the intensity of scattered light, which is proportional to the differential scattering cross section. Since the scattered light is proportional to the radius of gyration to the fourth power, the number of primary particles must be large to have an impact in the overall scattering. For example, there would have to be 100 million particles of radius 70 nm to scatter the same intensity of light scattered by one 7 μm particle. This example illustrates the relative numbers of primary particles required to have such an impact on the overall scattering pattern.

10.3 Abrupt Orifice

10.3.1 NanoActive™ MgO

10.3.1.1 High Pressure Data

Experimentation began with very high pressures to determine if complete breakup of NanoActive™ MgO particles was possible. A rudimentary aerosol generator was being used at the time without the aid of the mechanical stirrer and wiper system. The air was injected tangentially at the bottom of the generator and the aerosol exited the orifice at the top center of the generator. The aerosol generator was placed underneath the laser beam and pressure was controlled at the compressed air tank with the primary pressure control valve.

The first set of experiments was conducted at a range of pressures from 20-100 psi static pressure. The pressure was set at the tank with no flow. The ball valve was then opened and no difference was seen in light scattering data for all pressures in this range. Trends similar to those in Figure 10.2 were observed. The data were bimodal for pressures ranging from 20-100 psi.

Figure 10.2 shows little variation in particle size distribution as the distance from the orifice increased. This implies no significant level of aggregation or deaggregation occurs as a function of distance from the orifice. These data were taken at a static pressure, at the tank, of 20 psi.

10.3.1.2 Low Pressure Data

The rudimentary aerosol generator produced aerosols with inconsistent particle concentrations due to the cohesive nature of the NanoActive™ MgO powder. This was the reason for designing the aerosol generator shown in Appendix A. Pressure control and measurement were also improved. A pressure regulator and pressure transducer were introduced to the system, as shown in Chapter 9, to provide more accurate control and measurement of the pressure drop across the orifice.

Once the new system was in use, experiments were repeated at lower pressures. No significant changes in shape were noticed until the pressure drop across the orifice was below 4 psi. At these pressures the light scattering data began to transition to something that resembled Mie Scattering. This transition was first seen in Figure 10.4.

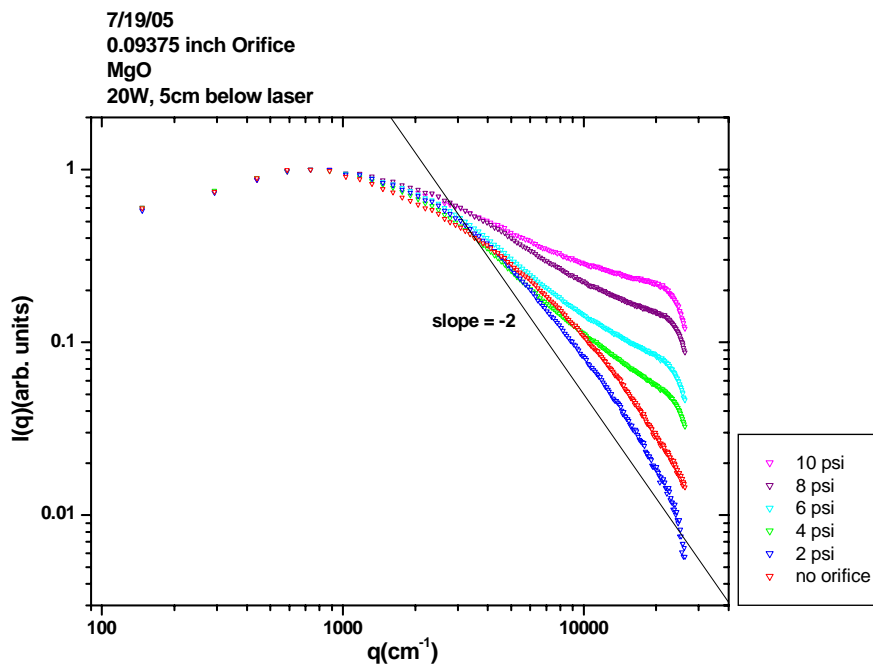


Figure 10.4: NanoActive™ MgO SALS Data at Low Pressures for Abrupt Orifice

The bimodal distribution began to emerge at low pressures as pressure increased. Efforts were then made to refine the measurements at pressures lower than the emergence of the bimodal distribution. Figure 10.5 shows the measurements taken for the refined low pressure scale. Increments of 0.25 psi were used from 0 to 1 psi. After 1 psi the aerosol measurements were taken every 0.5 psi up to 5 psi. Then additional measurements at 7.5 psi and 10 psi were made for the high pressure scale.

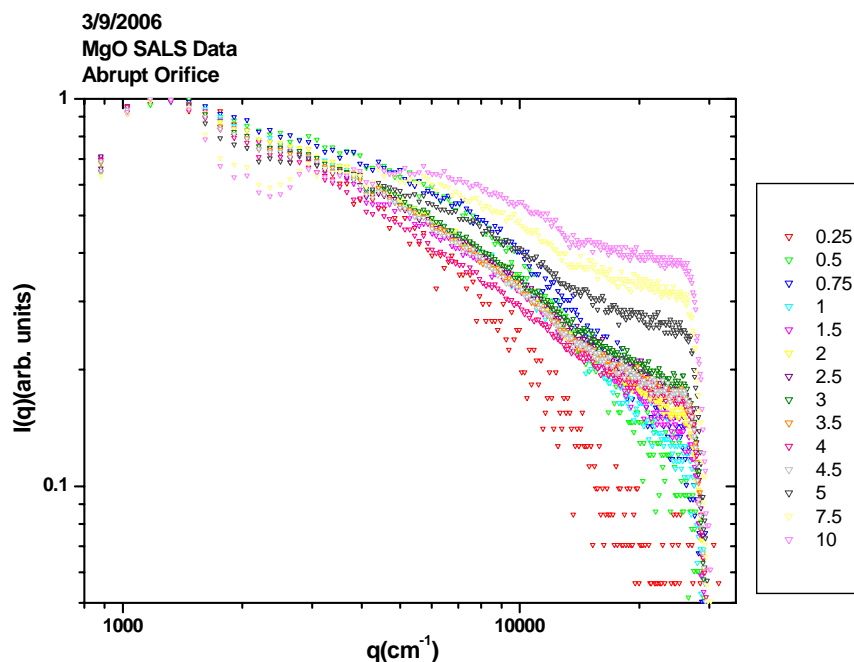


Figure 10.5: NanoActive™ MgO SALS Data for Abrupt Orifice

A bimodal distribution emerges at low pressures, as pressure increases. At pressures of 0.25-0.5 psi, the scattering data resembles Mie Scattering. As pressure increases, there is a significant increase in the intensity at higher q , indicating a larger presence of submicron particles, i.e. primary particles, in the aerosol. The transition appears to be continuous over a wide range of pressures. There does not seem to be a critical value of pressure at which the transition takes place.

The data were fit with bimodal distributions and shown in Figure 10.6. The scattering contribution ratios and mode sizes are given in Table 10.1.

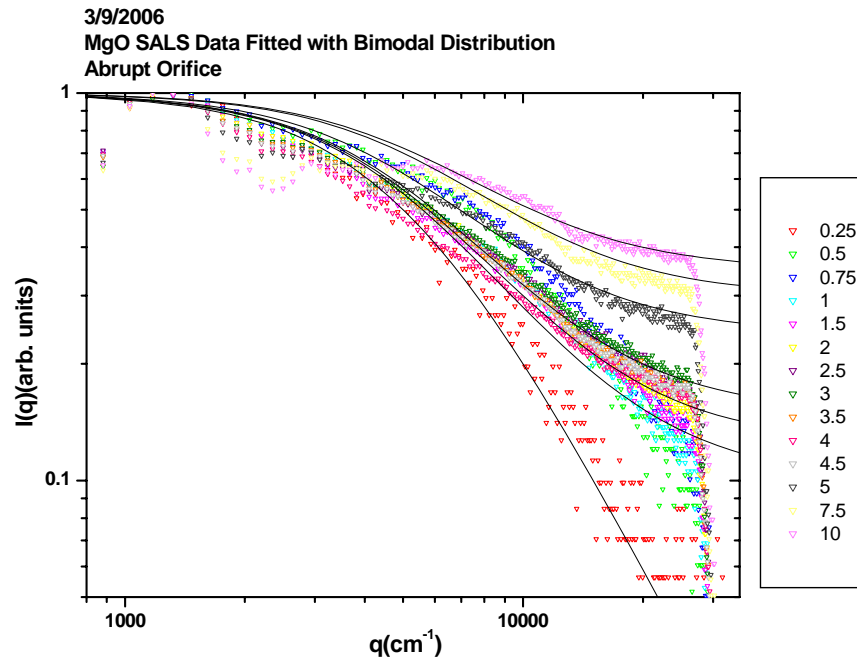


Figure 10.6: NanoActive™ MgO SALS Data for Abrupt Orifice Fitted with Bimodal Distribution

Data gathered on March 9, 2006 have a dip in the scattered intensity at $q \approx 2,500 \text{ cm}^{-1}$. This dip is due to background light subtraction. Before any light was scattered from the aerosol there was light incident upon that particular area of the photo diode array. When the signal was subtracted it created the dip in scattered intensity.

10.3.2 NanoActive™ MgO Plus

NanoActive™ MgO Plus was also aerosolized to observe changes in its size distribution as a function of pressure drop across the orifice. The experimental data collected for NanoActive™ MgO Plus was distinctively different than that of NanoActive™ MgO. Figure 10.7 shows no significant change in scattering for any change in pressure drop across the orifice. At first, the scattering data looks similar to the Mie Scattering trends that would be expected for a quasi-monodisperse aerosol. At $q \approx 5,000 \text{ cm}^{-1}$ the data transitions to a linear segment with a slope of -1.3. This linear segment shows the aerosol of NanoActive™ MgO Plus is polydisperse well beyond that of the bimodal distributions seen for NanoActive™ MgO. Polydisperse data that show no resemblance or signs of the Mie scattering envelops will be termed super-polydisperse. The NanoActive™ MgO Plus aerosol was super-polydisperse in the region of $q > 5000 \text{ cm}^{-1}$.

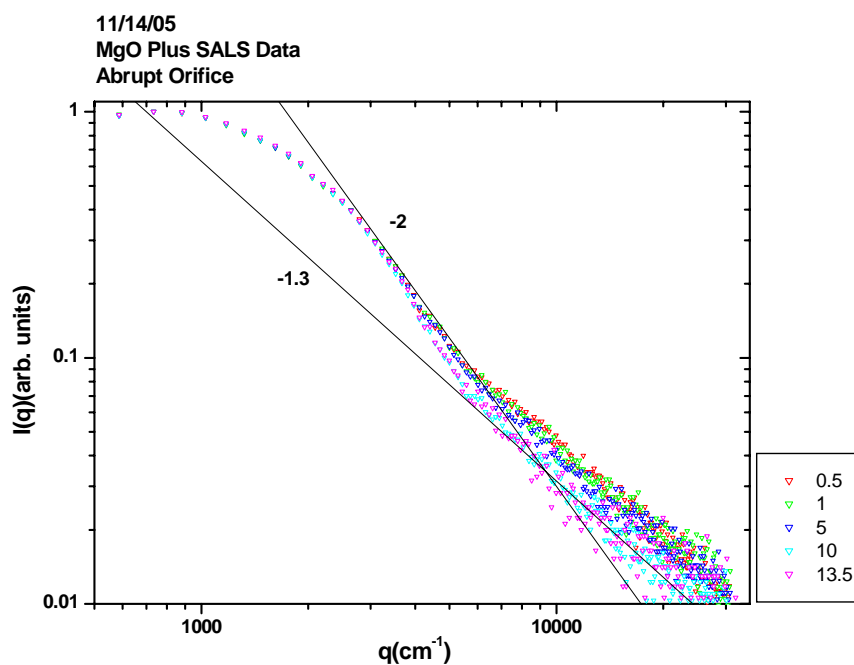


Figure 10.7: NanoActive™ MgO Plus SALS Data for Abrupt Orifice

10.3.3 TSI Hollow Glass Spheres

The experiments were repeated with TSI's hollow glass spheres because the size distribution had been acquired through the manufacturer. It was hypothesized that no aggregates were present to break up under increasing aerodynamic forces. Figure 10.8 shows scattering data for aerosols dispersed at pressures up to 13.5 psi across the orifice. The scattering data is constant as a function of pressure. The hypothesis was correct, no deaggregation occurred in the aerosol of hollow glass spheres and the curves showed Mie scattering trends.

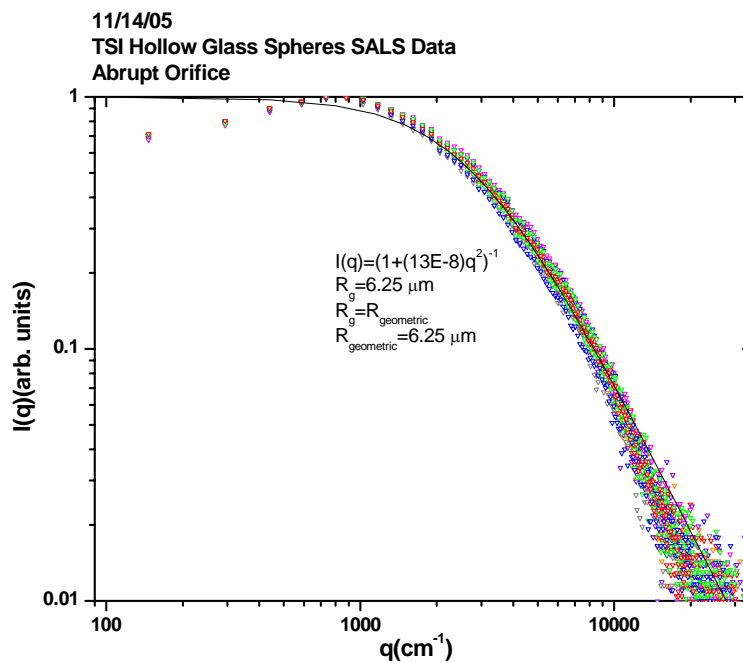


Figure 10.8: TSI Hollow Glass Spheres Guinier Analysis for Abrupt Orifice

The data were fitted with the Guinier Equation. The radius of gyration of the particles is found from the coefficient of q^2 . This fit suggests the particles are quasi-monodisperse and have a radius of gyration approximately $6.25 \mu\text{m}$. The radius of gyration is the same as the geometric radius for a thin spherical shell. The size distribution of these spheres was given by the manufacturer. Figure 2.3 shows these particles are in fact polydisperse.

The intensity is a strong function of size, the radius of the particle raised to the fourth power. If the number size distribution for the hollow glass spheres is weighted by the radius to the fourth power, Figure 10.9 results. Even though the size distribution is not unimodal, after weighting, it appears to have one particle size that dominates the scattering. This dominant size is approximately 7 μm . This shows excellent agreement with experimental data.

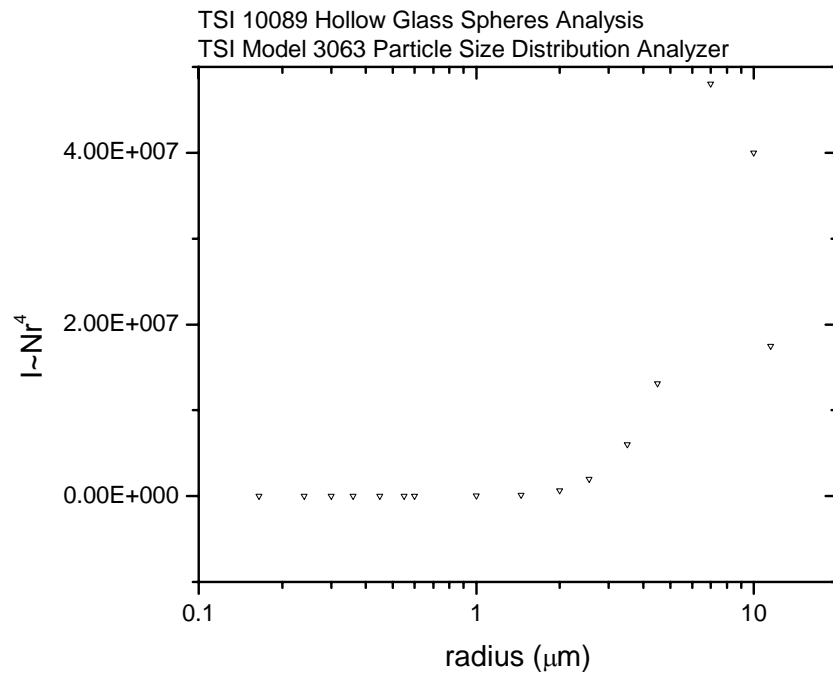


Figure 10.9: Glass Sphere Weighted Distribution to Reflect Scattering Intensity

These data support several important conclusions about the light scattering data. The most important characteristic shown by the data is the strong influence of size on light scattering. In the presence of large particles, small particles are insignificant unless their number concentration is 6 to 7 orders of magnitude higher than the large particles. This data also provides a check of accuracy in the light scattering measurements. Quasi-monodisperse aerosols can be measured but the results must be interpreted carefully to assure proper conclusions are drawn from the data.

10.3.4 Arizona Road Dust

Arizona Road Dust was aerosolized to determine the effects of varying fluid dynamic forces on its particle size distribution. Figure 10.10 shows scattered intensity versus q . The pressure drop across the orifice was taken at a minimum of 1 psi and a maximum of 15 psi. Data show a change in size distribution as a function of pressure but no signs Mie scattering. This aerosol is super-polydisperse for all pressures.

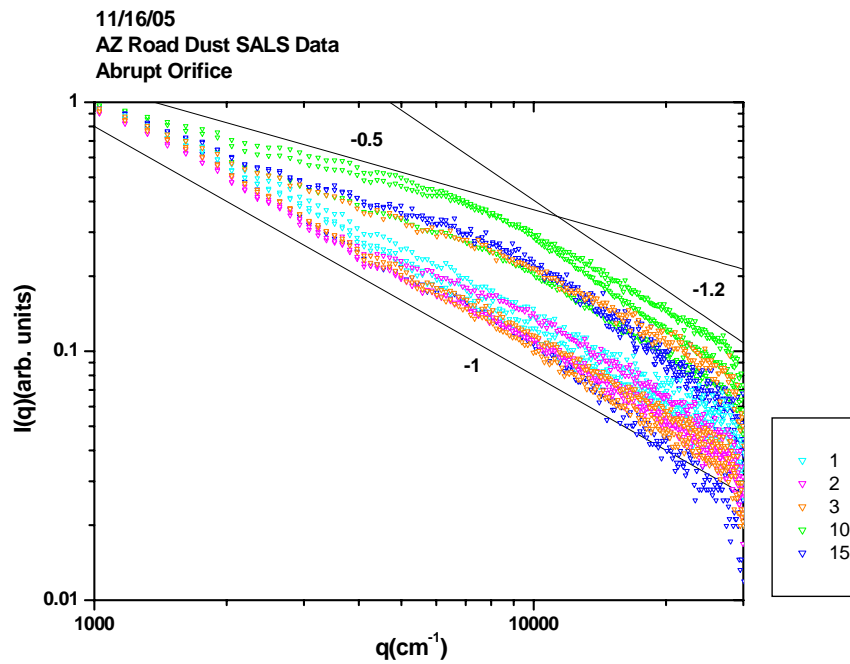


Figure 10.10: Arizona Road Dust SALS Data for Abrupt Orifice

10.3.5 Sodium Bicarbonate

Figure 10.11 shows light scattering intensity versus q for fire extinguisher grade sodium bicarbonate. Similar to the results for Arizona Road Dust, the sodium bicarbonate exhibits increasing polydispersity as a function of pressure drop across the orifice. At pressures of 10 psi and 20 psi there is a larger presence of small particles indicated by higher intensity at larger q . There is a drop in intensity from 0.5 to 1 psi, but this is disregarded since the curves for low pressures have approximately the same slope. Once the pressure is increased to 10 psi there is a significant increase in intensity at higher q . This aerosol is also super-polydisperse. The data show no signs of the Mie scattering envelopes.

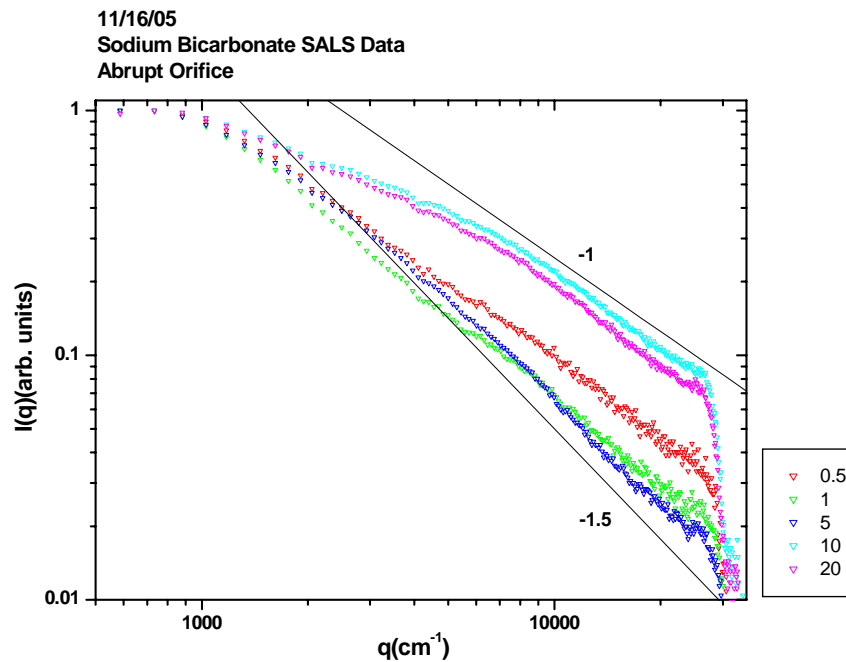


Figure 10.11: Sodium Bicarbonate SALS Data for Abrupt Orifice

10.4 Converging-Diverging Nozzle

The second nozzle used to aerosolize the particles was the converging-diverging nozzle with the same throat area as the abrupt orifice. Other dimensions for the converging-diverging nozzle can be found in Chapter 7. Figure 10.12 shows light scattering data for pressure drops across the orifice from 0.25 to 10 psi. Similar to the abrupt orifice, the converging-diverging nozzle shows increasing polydispersity as a function of pressure.

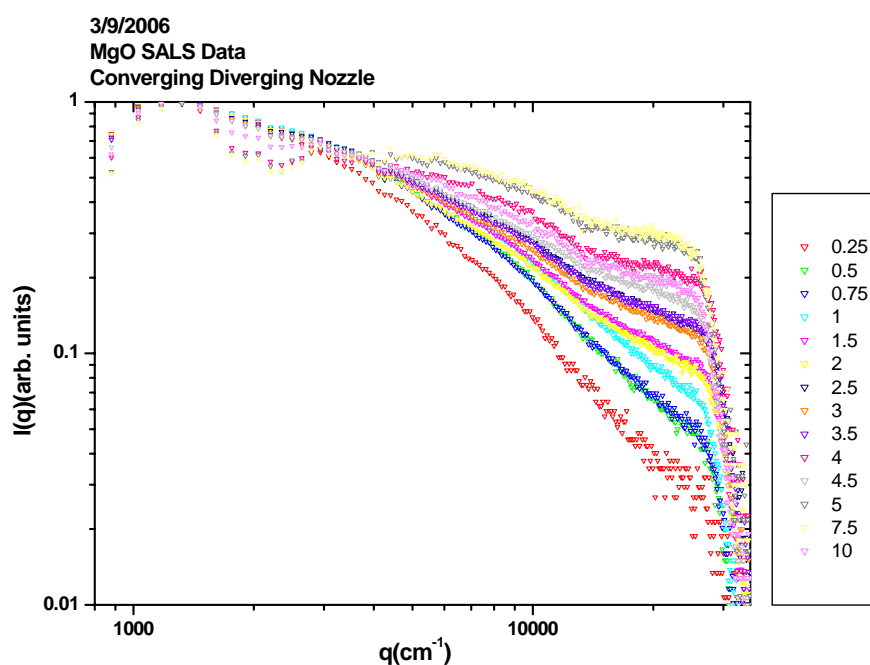


Figure 10.12: NanoActive™ MgO SALS Data for Converging-diverging Nozzle

Figure 10.13 shows the converging-diverging nozzle data fitted with bimodal size distributions. At low pressures the data resemble that of Mie Scattering. As the pressure drop increases the presence of smaller particles increases significantly, producing the characteristic plateau at high q . Data for the light scattering contribution can be found in Table 10.1.

NanoActive™ MgO was the only powder aerosolized with this nozzle. No significant differences in deaggregation were seen between the abrupt orifice and the converging-

diverging nozzle, therefore, it was not deemed necessary to repeat the experiment for NanoActive™ MgO Plus.

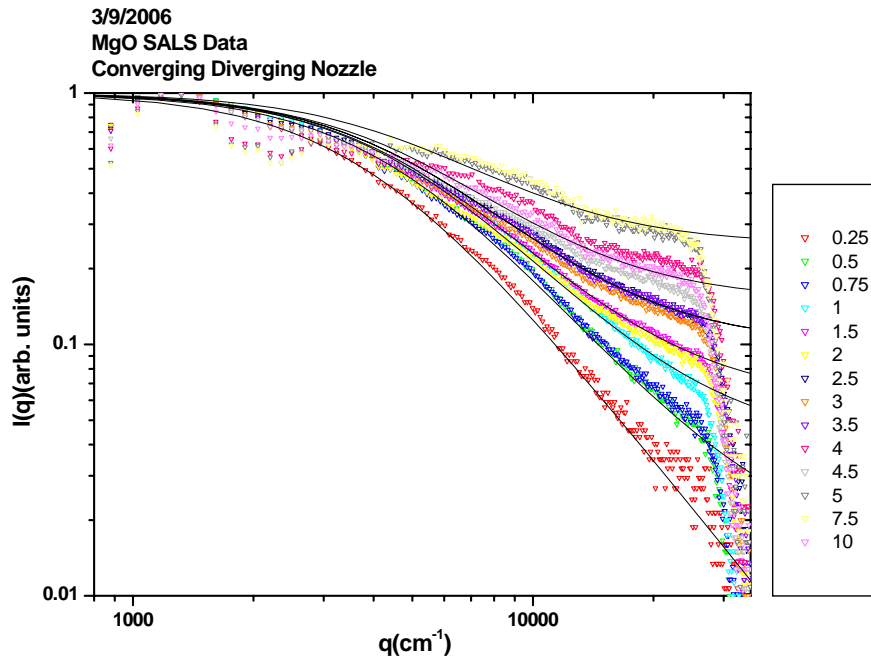


Figure 10.13: NanoActive™ MgO SALS Data for Converging-diverging Nozzle

10.5 Converging Nozzle

A converging nozzle was tested to see if there were significant differences in deaggregation compared to the abrupt orifice and the converging-diverging nozzle. Dimensions for the converging nozzle can be found in Chapter 7. The converging nozzle shows the same general trends seen in the abrupt orifice and the converging-diverging nozzle. As the pressure drop across the nozzle increases the influence of small particles on the scattering intensity increases. Figure 10.14 shows the light scattering data for the converging nozzle.

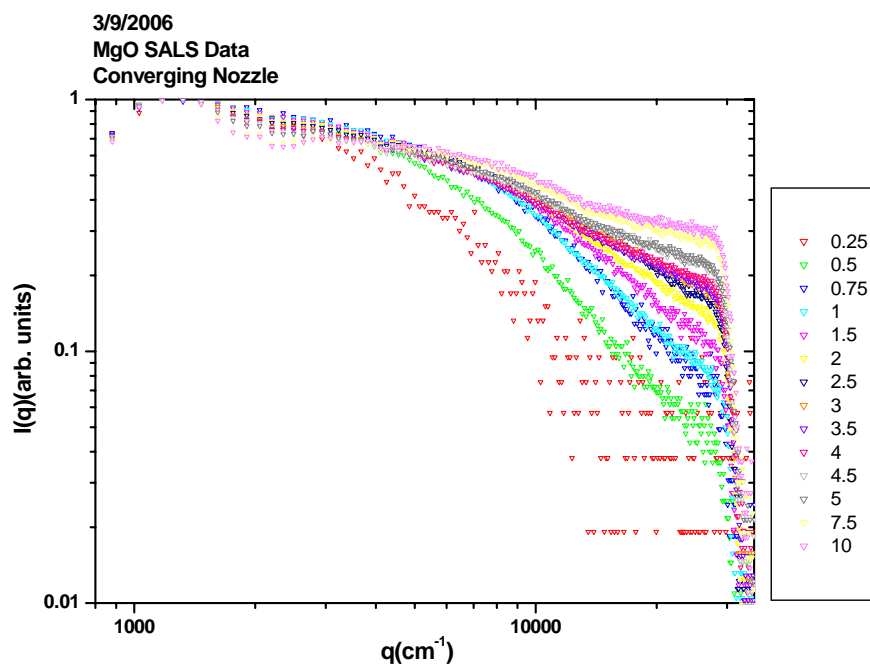


Figure 10.14: NanoActive™ MgO SALS Data for Converging Nozzle

Figure 10.15 shows the data for the converging nozzle once fitted with bimodal distributions. At low pressures, 0.25 and 0.5 psi, the data could be reasonably approximated by Mie Scattering. However, as the pressure increases, scattering from smaller particles makes a significant contribution to the overall scattering. Values for the light scattering contribution from the large particles can be found in Table 10.1.

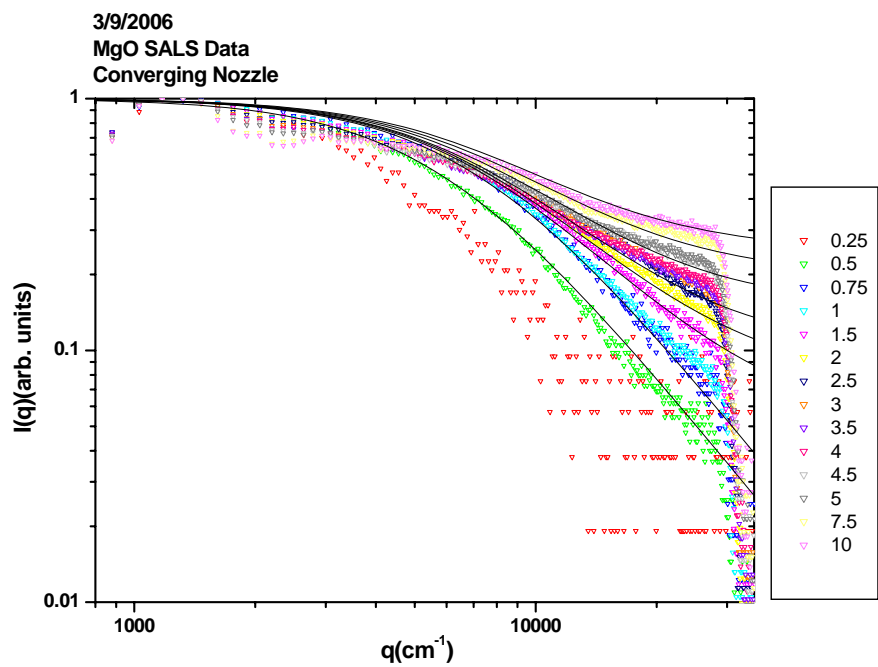


Figure 10.15: NanoActive™ MgO SALS for Converging Nozzle

10.6 Mesh Nozzle

The last nozzle tested was designed to create an environment more conducive to impaction. Three meshes were placed in series in the nipple. The dimensions of the mesh nozzle can be found in Chapter 7. Figure 10.16 shows the light scattering data as a function of pressure drop across the nozzle. No data was taken for 0.25 psi because the scattered intensity was not large enough to measure. Although there does seem to be some dependence on pressure, it is not nearly as distinct as the dependence for the abrupt, converging, and converging-diverging nozzles. The increase in intensity at high q represents an increase in small particles, but the increase in intensity from 0.5 psi to 10 psi is much less than all three of the other nozzles.

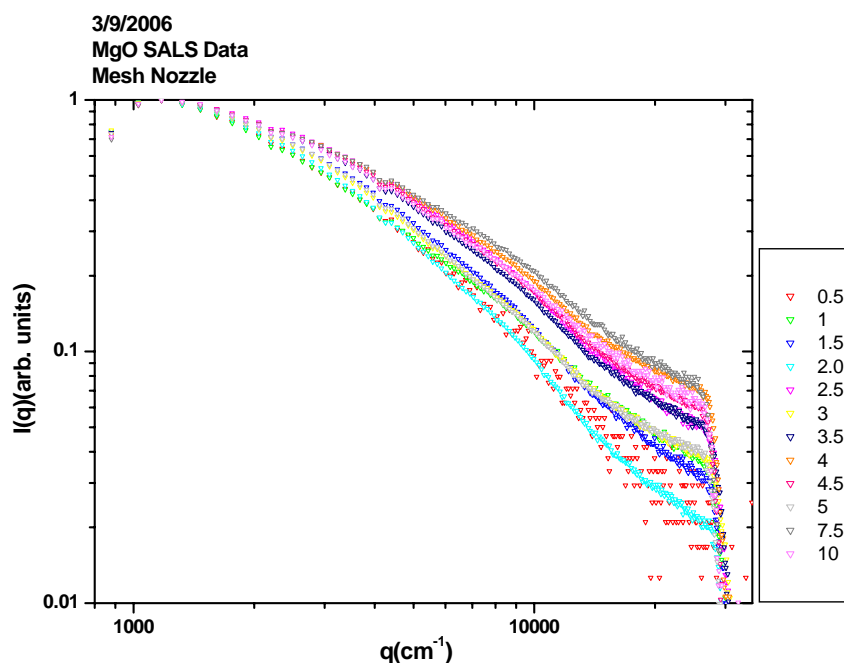


Figure 10.16: NanoActive™ MgO SALS Data for Mesh Nozzle

The data were fit in the same manner as the other nozzles and plotted in Figure 10.17. The light scattering contribution for large and small particles can be found in Table 10.1. NanoActive™ MgO was the only material tested in this nozzle since it seemed less effective than the abrupt, converging-diverging, and converging nozzles.

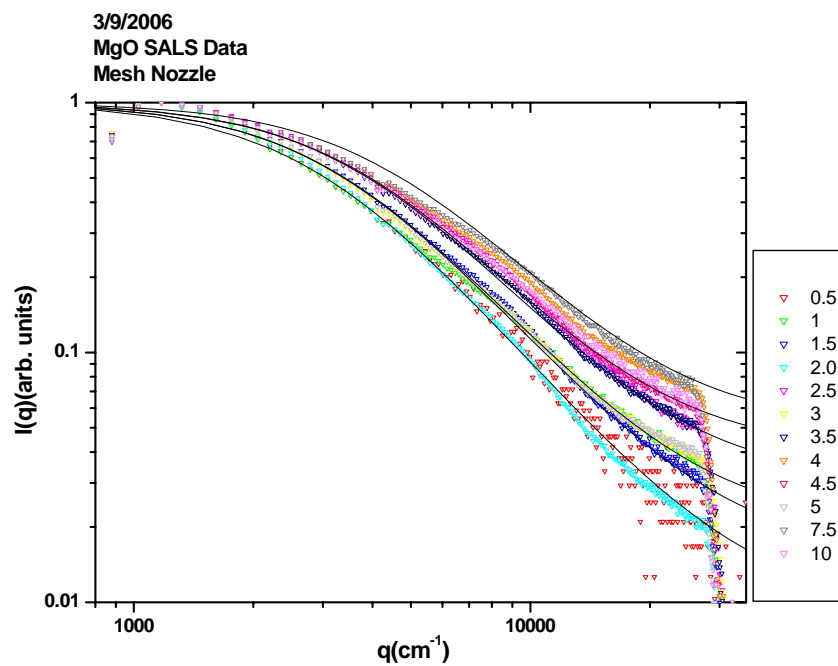


Figure 10.17: NanoActive™ MgO SALS Data for Mesh Nozzle

10.7 Open Nipple

The last aerosol generator configuration had no nozzle at all. The ¼” pipe nipple was left open, without an orifice or nozzle attached. The nipple was a standard aluminum nipple with an inside diameter of 0.36”. Figure 10.18 shows the light scattering data as a function of pressure. No significant changes are seen up to 2.5 psi. Beyond 2.5 psi the flow rate was too high for the exhaust system to handle effectively. NanoActive™ MgO was the only material dispersed through the open nipple. The data show no signs of Mie scattering hence imply this aerosol was super-polydisperse.

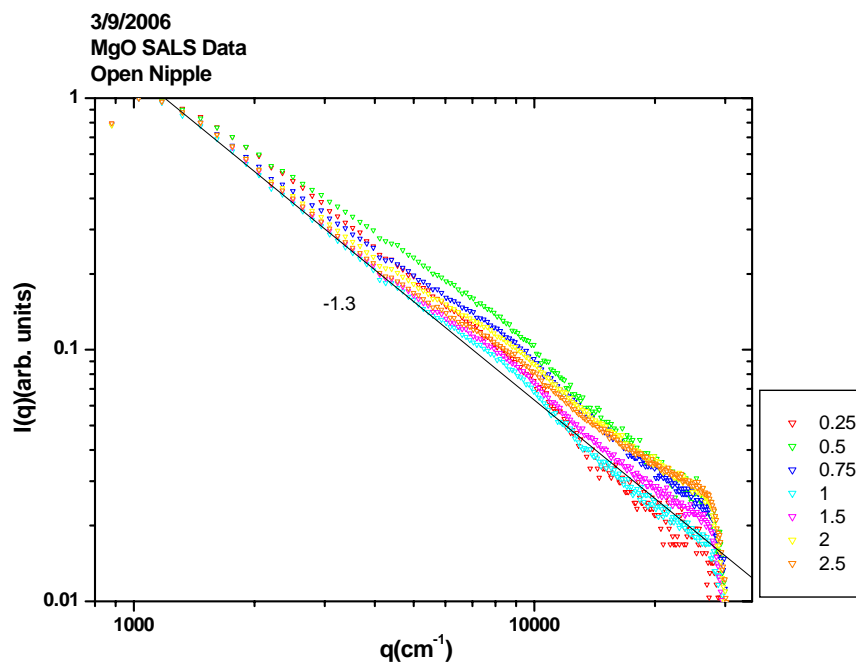


Figure 10.18: NanoActive™ MgO SALS Data for Open Nipple

10.8 Light Scattering Contribution Analysis

The scattering contribution ratios used in the bimodal fits are shown in Table 10.1. For instance, the bimodal curve fit used for the abrupt orifice data at 10 psi is given by

$$I(q) = 0.65 \left[1 + (3 \cdot 10^{-8}) q^2 \right]^{-1} + 0.35. \quad (10.1)$$

The small particle contribution ratio is denoted x in the table, e.g. 0.35 from Equation 10.1. If the data is assumed bimodal, the scattering not attributed to small particles must come from the large particles. Thus, the large particle contribution ratio is $1-x$, e.g. 0.65 in Equation 10.1. The next column in Table 10.1 is the size of the large mode. This size is calculated from the q^2 coefficient from the Guinier Curve Fit Equation, Equation 10.1. The Guinier Equation is given in Equation 8.23, and is repeated here for illustration purposes,

$$I(q) = I_0 \left(1 + q^2 R_g^2 / 3 \right)^{-1}. \quad (10.2)$$

From Equations 10.1 and 10.2,

$$3 \cdot 10^{-8} \text{ cm}^2 = \frac{R_g^2}{3} \quad (10.3)$$

hence, $R_g = 3.0 \mu\text{m}$. The size of the large mode decreases with increasing pressure, indicating deaggregation.

Table 10.1: Scattering Contribution Ratio

Pressure	Abrupt Orifice			Converging-Diverging Nozzle			Converging Nozzle			Mesh Nozzle		
	(1-x)	x	Size of Large Mode (μm)	(1-x)	x	Size of Large Mode (μm)	(1-x)	x	Size of Large Mode (μm)	(1-x)	x	Size of Large Mode (μm)
0.25	1	0	3.46	1	0	4.58	--	--	--	--	--	--
0.5	--	--	--	0.985	0.015	3.87	1	0	3.00	--	--	--
0.75	--	--	--	--	--	--	--	--	--	--	--	--
1	--	--	--	0.96	0.04	3.67	1	0	2.45	0.98	0.02	5.20
1.5	0.9	0.1	3.46	--	--	--	0.95	0.05	2.45	0.985	0.015	5.20
2	--	--	--	0.94	0.06	3.67	0.925	0.075	2.45	0.991	0.009	5.74
2.5	--	--	--	--	--	--	0.9	0.1	2.45	--	--	--
3	0.85	0.15	3.46	0.9	0.1	3.67	--	--	--	--	--	--
3.5	--	--	--	--	--	--	--	--	--	0.97	0.03	4.58
4	0.875	0.125	3.46	0.85	0.15	3.67	--	--	--	--	--	--
4.5	--	--	--	--	--	--	0.85	0.15	2.45	--	--	--
5	0.76	0.24	3.46	--	--	--	--	--	--	--	--	--
7.5	0.7	0.3	3.00	0.75	0.25	3.46	0.8	0.2	2.45	0.95	0.05	3.87
10	0.65	0.35	3.00	--	--	--	0.75	0.25	2.45	0.96	0.04	4.58

Some data are very well represented by the same equation. For this reason not all pressures have a corresponding large and small particle contribution ratio. For instance, in the converging nozzle data set, Figure 10.15, pressures 4.0, 4.5, and 5.0 psi are all well represented by one curve fit. Thus, data were recorded for only one of these pressures. Once the data deviates from that grouping, another curve fit is developed to approximate the next set of pressure measurements.

The large particle contribution ratio versus pressure is plotted in Figure 10.19. This graph represents what proportion of the total scattering can be attributed to scattering from the particles of the largest mode. In the abrupt orifice, at 0.25 psi, 100% of the total scattering is from the large particles. At 10 psi, their contribution to the total scattering drops to 65%, which implies 35% of the total scattering comes from the mode less than 400 nm.

Figure 10.19 shows the data for scattering contribution from the large particle mode as well as linear fits for the data. This is shown merely for the overall trends displayed by the data. As the pressure increases, the light scattered from the small particles increases, which implies a significant increase in the number of those particles. The abrupt, converging-diverging, and converging nozzles all seem to belong in a similar group. The mesh nozzle, however, is different. The data change less as a function of pressure than the other nozzles. Error bars were added based on the human error involved in fitting the data. The error is approximately ± 0.025 , which provides additional support for concluding the abrupt orifice, converging-diverging, and converging nozzles cause similar degrees of deaggregation to NanoActive™ MgO particles.

3/9/2006
MgO Light Scattering Contribution Data

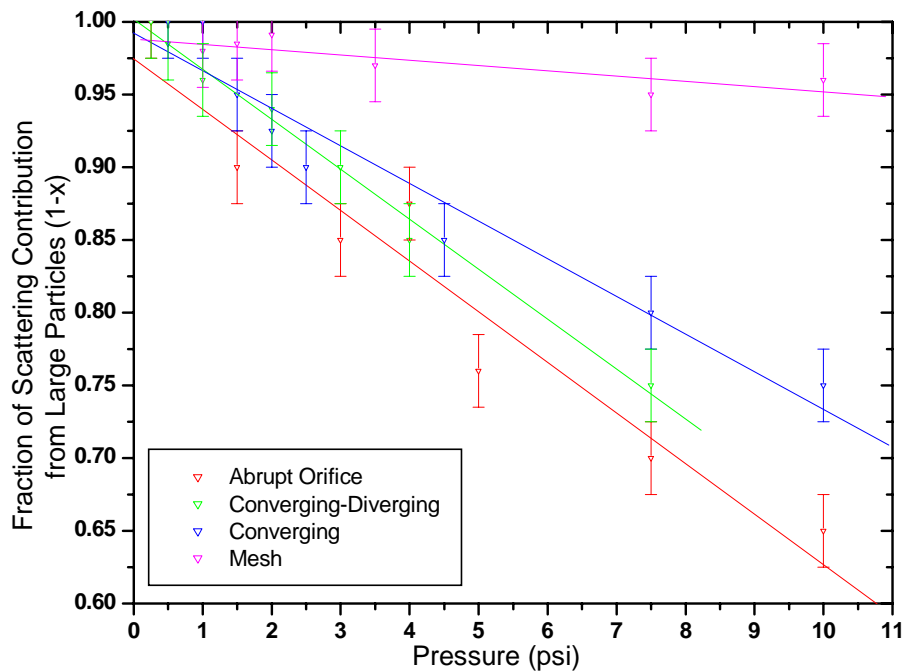


Figure 10.19: Scattering Contribution Analysis

11 DISCUSSION

11.1 Degrees of Polydispersity

The Mie scattering trends seen in Figure 8.5 are derived for a set of monodisperse spherical scatterers. In the real world, very few systems of scatterers are monodisperse with perfectly spherical particles. Light scattering data from several non-spherical, polydisperse systems of scatterers have been collected in this study. We have coined three degrees of polydispersity to describe our data: quasi-monodisperse, bimodal-polydisperse, and super-polydisperse.

Aerosols displaying light scattering trends similar to theoretical Mie Scattering envelopes were termed quasi-monodisperse in this study. These aerosols are not monodisperse but the degree of polydispersity is not great enough to alter the patterns seen in Figure 8.5. The next degree of polydispersity is for aerosols with two or more modes. The light scattering results for this type of aerosol can be thought of as the addition of Mie Scattering patterns for all such modes, individually retaining the patterns seen in Figure 8.5. The last degree of polydispersity was termed super-polydisperse. No signs of Mie Scattering trends were seen in the scattering patterns of such aerosols.

11.2 Entrainment

The turbulent and viscous forces present during particle entrainment can lead to deaggregation (Finlay 2001). The air inlet tube is directed straight down at the powder bed in the experimental aerosol generator. The high velocity jet of air coupled with the geometry of the aerosol generator creates complex flow fields and turbulent eddies within the aerosol chamber. The open nipple experiment was conducted to determine if the deaggregation of NanoActive™ MgO particles was due to entrainment effects or the fluid dynamic forces created by the deaggregation nozzles. Figure 10.18 shows data collected without the use of any deaggregation nozzle on the aerosol generator. The aerosol exited the aerosol chamber through a ¼" NPT nipple. The data show no significant change in particle size distribution with an increase in pressure. This implies no deaggregation is caused by the fluid forces present at entrainment; we conclude that the deaggregation of

NanoActive™ MgO particles as seen in Figures 10.6, 10.13, and 10.15 is due to the presence of deaggregation nozzles at the outlet.

It should be noted that NanoActive™ MgO data for the open nipple configuration, Figure 10.18, were termed super-polydisperse in the data section due to the -1.3 slope. However, if we look back at Figure 10.4, we see another data set for the same configuration. The no orifice data in Figure 10.4 show patterns expected for a quasi-monodisperse aerosol. Although this difference cannot be fully explained, we have a few theories as to why it occurred.

Electrostatic charging could have played a significant role in particle cohesion from day to day. Changes in humidity, powder handling, and other environmental factors could all have affected the cohesiveness of the NanoActive™ MgO powder. In Figure 10.4, the electrostatic charge may have been high, creating more cohesive agglomerates. The electrostatic charge in Figure 10.18 might have been less. This could translate into an aerosol with more small particles, i.e. greater polydispersity, hence the -1.3 slope.

Another possible explanation for this occurrence was a difference in flow rates through the aerosol chamber. Higher flow rates would increase the size range of entrained particles, hence a higher degree of polydispersity. Quasi-monodisperse light scattering data would result from lower flow rates, i.e. a smaller size range of entrained particles. If larger flow rates entrained more particles, the aerosol would then appear super-polydisperse.

11.3 Deaggregation due to Impaction

A particle will deviate from the path of fluid flow given sufficient inertia. The study of this phenomenon and its use in the separation of particles from fluids is called impaction theory.

11.3.1 Other Research

Section 4.4.2 discusses other research regarding impaction. From a theoretical standpoint Kousaka et al. (1979) claim impaction is the most effective deaggregation mechanism.

These researchers claim to have deaggregated sub-micron particles with wire screens. The theory that impaction creates the highest internal particle forces may be accurate, but the probability of impaction is highly unlikely for particles in the sub-micron range. Mendes et al. (2004) show little evidence of deaggregation in the Aerodisperser as a function of increased velocity, i.e. increased impaction at the impaction pin. The particles used in the Mendes study were in the 1-10 μm range. Voss and Finlay (2002) experimented with 60 μm lactose carrier particles. They found no significant deaggregation in a wire mesh deaggregation device of their own design. Intuitively, the particles would have impacted the screen due to their substantial inertia. The studies by Mendes and Voss and Finlay suggest impaction is not a significant source of deaggregation in aerosols due the low probability of impaction in their experimental devices. The conclusions of these three studies are inconsistent. The probability of impaction is dependent on particle size, wire mesh design, and air flow. The devices used in this study will be analyzed without regard to other researcher's findings due to these dependencies.

11.3.2 Impaction Theory

Inertial impaction is often quantified by the particle Stokes number,

$$Stk_p = \frac{U_p \rho_p d_p^2}{18\mu D}, \quad (11.1)$$

where the velocity, density, and diameter of the particle are represented by U_p , ρ_p , and d_p , respectively. The viscosity of the fluid is represented by μ and D is a characteristic dimension of the obstacle in the path of the particle. The particle is likely to impact the obstacle when the Stokes number is greater than 10 (Voss and Finlay 2002).

11.3.3 Mesh Nozzle

The mesh nozzle used in this study consisted of three 26x26 wire meshes. For one of the wires in the mesh nozzle, $D = 1.91 \cdot 10^{-4} \text{m}$, and $\mu = 1.81 \cdot 10^{-5} \text{kg} / \text{m} \cdot \text{s}$. In the particular case of NanoActive™ MgO particles, $\rho_p = 600 \text{kg} / \text{m}^3$. This density is the bulk density of the powder. The bulk density accounts for the porous structure of the aggregates, i.e.

trapped air. The mean aggregate size for NanoActive™ MgO is $d_p = 3.3 \cdot 10^{-6} m$. To ensure impaction, the Stokes number must be greater than 10 (Voss and Finlay 2002). Rearranging Equation 11.1 and solving for the critical particle velocity, $U_p = 95 m/s$. This result suggests that any 3.3 μm particle traveling at a speed of 95 m/s will impact the wire mesh. The particle will follow the flow, i.e. not impact the mesh, if it is moving slower than this critical velocity. The critical velocity will decrease as the size of the particle increases because additional mass means greater inertia.

The true density of an individual NanoActive™ MgO particle is closer to 3,200 kg/m³. The true density does not consider the porous voids in each particle. The critical velocity would decrease as the density shifted toward the true density. A slight increase in density might make the critical velocity calculation more accurate. At a density of 1,000 kg/m³, the critical velocity for a 3.3 μm NanoActive™ MgO particle would be $U_p = 57 m/s$.

When particles become small, less than 1 μm , an adjustment is made to the Stokes number. When particles become small, the drag force is reduced by the breakdown of the no-slip boundary condition. As the flow changes direction to move around an obstacle the particle is less likely to follow the flow because of reduced drag forces. The slip corrected Stokes is given by

$$Stk_p = \frac{U_p \rho_p d_p^2 C_c}{18 \mu D} \quad (11.2)$$

where C_c is the Cunningham Slip Correction Factor. The slip correction factor is given by

$$C_c = 1 + \frac{\lambda}{d} \left[2.34 + 1.05 \cdot e^{-0.39(d/\lambda)} \right] \quad (11.3)$$

where λ and d are the mean free path of the gas and the particle diameter, respectively (Hinds 1999). For the NanoActive™ MgO calculations above, $d_p = 3.3 \cdot 10^{-6} m$, the slip correction increases the Stokes number by less than 5%, thus will be neglected.

Figure 10.17 shows the data collected for the mesh deaggregation nozzle. Some deaggregation is seen as the pressure increases. Particles greater than 10 μm in diameter could be impacting the mesh at higher pressures. Figure 10.19 shows the level of deaggregation for the mesh nozzle with respect to other nozzles. The data suggest the mesh nozzle was not as effective as the abrupt orifice, converging-diverging, or converging nozzles. Some deaggregation can be seen and is attributed to the impaction of the largest particles, greater than 10 μm , in the aerosol. Inertial impaction seems to be less significant when the particle size is less than 5 μm .

11.3.4 Abrupt Orifice

Kousaka et al. (1979) suggest impaction was a possible cause of deaggregation in orifice flow. Impaction theory can be applied to determine whether Kousaka's suggestion is accurate for the abrupt orifice used in our experiments.

The aerosol velocity in the nipple must be known to apply Stokes theory for impaction. The flow must be considered compressible due to the high velocities of the aerosol stream at the outlet. Inertial impaction increases as velocity increases, therefore, the best case scenario for impaction occurs when the flow goes sonic. It is highly doubtful the flow went supersonic in any of the trials due to the rough construction of the abrupt orifice and lack of a diverging section. Supersonic flows will be neglected in this analysis.

The air will be modeled as an ideal gas and the expansion process will be considered isentropic to find the aerosol velocity in the nipple. The boundary conditions and geometry of the nozzle, modeled as converging, are shown in Figure 11.1. The reservoir section is analogous to the compressed air tank. The nipple in this model is the actual nipple attached to the abrupt orifice. The air passes through the orifice into open atmosphere.

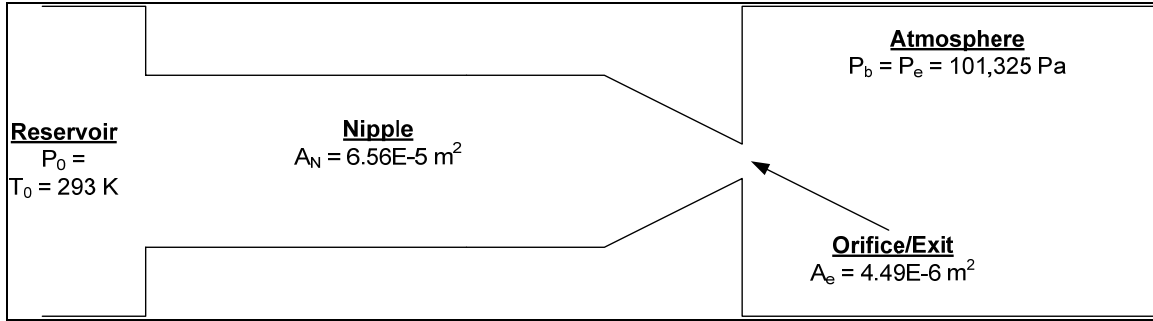


Figure 11.1: Model of Compressible Flow in Abrupt Orifice Nozzle

In this study the orifice diameter was 3/32" (2.38E-3 m) and the inside diameter of the nipple was 0.36" (9.14E-3 m). The areas are calculated and shown in Figure 11.1. The back pressure, P_b , is atmospheric pressure. The reservoir temperature is taken at 20°C or 293 K. The reservoir pressure is considered unknown for the moment.

Maximum flow occurs when the Mach number at the orifice exit is 1, i.e. sonic. The flow will reach a sonic condition and then become choked with any further increase in pressure. Any additional increase in pressure drop across the orifice will not increase the mass flow rate, hence, choked flow.

At the onset of choked flow, assuming isentropic expansion of an ideal gas, the pressures are related by

$$\frac{P_e}{P_0} = \left(\frac{2}{k+1} \right)^{k/(k+1)} \quad (11.4)$$

where k is the ratio of specific heats. For air, $k = 1.4$. When the flow is sonic at the exit plane, the back pressure equals the pressure at the exit plane, P_e . Therefore,

$$\frac{P_b}{P_0} = 0.5283. \quad (11.5)$$

Since the back pressure is known, the reservoir pressure can be found. At the onset of choked flow, $P_0 = 191,840 \text{ Pa (abs)} = 27.82 \text{ psia} = 13.12 \text{ psig}$. This means that the flow becomes choked when the pressure drop across the orifice is 13.12 psi. If the pressure drop is increased beyond this critical value, the mass flow rate will not increase.

For choked flow, the mass flow rate is given by

$$\dot{m}_{choked} = A_e P_0 \sqrt{\frac{k}{RT_0}} \left(\frac{2}{k+1} \right)^{(k+1)/2(k-1)}, \quad (11.6)$$

where R is the universal gas constant divided by the molecular weight of the ideal gas ($R_{air} = 287 \text{ J / kg} \cdot \text{K}$). For air, Equation 11.6 reduces to

$$\dot{m}_{choked} = \frac{0.04 A_e P_0}{\sqrt{T_0}}. \quad (11.7)$$

In Equation 11.7, the mass flow rate, area, pressure, and temperature are given in kg/s, m^2 , Pa, and Kelvin, respectively. Substituting for the exit area, reservoir temperature, and reservoir pressure at the onset of choked flow, $\dot{m}_{choked} = 1.99 \cdot 10^{-3} \text{ kg / s}$.

The ideal gas equation states

$$P = \rho RT. \quad (11.8)$$

This equation can be used to determine the density of air in the reservoir at the pressure corresponding to the onset of choked flow, P_0 . Rearranging Equation 11.8 and substituting the known values of pressure and temperature gives $\rho_0 = 2.28 \text{ kg / m}^3$.

Assume the air density in the nipple, ρ_N , is the same as the air density in the reservoir.

The conservation of mass states that

$$\dot{m}_{choked} = \dot{m}_N = \rho_N V_N A_N. \quad (11.9)$$

Solving Equation 11.9 gives $V_N = 13.3 \text{ m / s}$. The density assumption made previously is reasonable at this nipple velocity.

If the exit velocity was considered sonic, $V_e = 340 \text{ m / s}$, and the simple incompressible model of the conservation of mass was used, i.e. constant density, the nipple velocity would be found to be $V_N = 23.3 \text{ m / s}$. The compressibility of the air actually reduces the result for the nipple velocity. This occurs because the density of the air in the nipple is much higher than the density at atmospheric pressure. As the density increases, the velocity must decrease to satisfy the continuity equation.

Now that the nipple velocity, $V_N = 13.3 \text{ m/s}$, is known, the size of a particle that would impact the orifice due to inertial effects can be calculated. The Stokes number for orifice flow is given by

$$Stk_p = \frac{U_p \rho_p d_p^2}{18 \mu D} \quad (11.10)$$

where D is the diameter of the orifice. Rearranging Equation 11.10 for particle diameter gives

$$d_p = \sqrt{\frac{18 \mu D \cdot Stk_p}{\rho_p U_p}}. \quad (11.11)$$

Voss and Finlay (2002) suggest impaction occurs when $Stk_p > 10$. The maximum nipple velocity is substituted for the particle velocity, U_p , and $\rho_p = 600 \text{ kg/m}^3$. Solving for the particle diameter gives $d_p = 31 \mu\text{m}$. This calculation suggests that no particle less than $31 \mu\text{m}$ would impact the orifice. In fact, no particle less than $31 \mu\text{m}$ would ever impact since the choked flow condition produced the highest flow rate possible. At lower pressures the air velocity in the nipple would be lower, resulting in larger particles being able to pass through the orifice without impacting the surface. The density of air in the nipple would increase at pressures beyond the critical pressure. To satisfy the continuity equation the nipple air velocity would then decrease.

The degree of deaggregation seen in Figure 10.6 is high for pressures below 10 psi. Some of the largest particles, greater than $31 \mu\text{m}$, may be impacting at the orifice. The mean particle size, $d_{50} = 3.3 \mu\text{m}$, suggests few particles exist in this range. The results from the impaction calculations coupled with the data for the mesh nozzle, Figure 10.17, suggest impaction is not a significant source of deaggregation in the abrupt orifice.

11.4 Deaggregation Stresses within a Single Spherical Particle

Deaggregation stresses within a single spherical particle will be calculated in this section. The CFD simulated flow data as well as theory from Bagster and Tomi (1974) and

Kousaka et al. (1979) will be used to make these calculations. The MathCAD worksheet with further details of the calculations can be found in Appendix C.

11.4.1 Stresses within a Single Spherical Particle in Uniform Flow

Bagster and Tomi (1974) derived the maximum stresses in the mid-plane of a single spherical particle in uniform flow. Equation 4.1 represents the theoretical maximum tensile stress, σ_{\max} , and maximum shear stress, τ_{\max} , in the mid-plane. The stresses are considered maximum when the particle is initially put into the flow. The values of mean velocity, u_r , were taken as the maximum velocities from Figure 7.2. The maximum velocities correspond to the velocities in the 3/32" diameter region of each nozzle. The particle diameter used in the calculations was $d = 0.5 \cdot 10^{-6} m$. The stress values for a single spherical particle in uniform flow can be found in Table 11.1.

Table 11.1: Mid-Plane Stresses in a Single Spherical Particle in Uniform Flow

Nozzle	u_r Figure 7.2 (m/s)	$\sigma_{\max}=\tau_{\max}$ Eqn. 4.1 (Pa)
Abrupt	75.3	8.18E+03
Converging-Diverging	151.3	1.64E+04
Converging	75.3	8.18E+03

11.4.2 Stresses within a Single Spherical Particle in Shear Flow

Many experimental studies suggest shear is a significant cause of particle deaggregation. Some authors attribute the deaggregation of particles to this type of flow but do not attempt to quantify the internal forces generated within such particles.

Bagster and Tomi (1974) derived the theoretical maximum tensile stress, σ_{\max} , and maximum shear stress, τ_{\max} , in the mid-plane of a single spherical particle in shear flow. The stresses are maximum when the particle is initially put into the flow. These stresses are represented by Equations 4.2 and 4.3. Interestingly, both of these equations are independent of particle size. The maximum strain rates, γ_{\max} , for each nozzle, were taken from Figure 7.8. The resulting stresses for each nozzle are given in Table 11.2.

Table 11.2: Mid-Plane Stresses in a Single Spherical Particle in Shear Flow

Nozzle	γ_{\max} Figure 7.8 (1/s)	σ_{\max} Eqn. 4.2 (Pa)	τ_{\max} Eqn. 4.3 (Pa)
Abrupt	1.20E+05	10.9	18.5
Converging-Diverging	1.50E+05	13.6	23.1
Converging	1.40E+05	12.7	21.5

11.4.3 Stresses within a Single Spherical Particle in Accelerating Flow

The bulk acceleration of the flow in each experimental nozzle was determined from CFD simulations. These values can be found in Figure 7.4. Newton's Second Law states

$$F = ma . \quad (11.12)$$

The forces that cause the particles to accelerate can be found for one primary NanoActive™ MgO particle, assumed spherical, $d_p = 0.5 \mu m$. The mass of the particle is given by

$$m_p = \frac{\pi \rho_p d_p^3}{6} . \quad (11.13)$$

Assuming $\rho_p = 3,200 \text{ kg} / \text{m}^3$ because a primary particle is not porous,

$m_p = 2.09 \cdot 10^{-16} \text{ kg}$. Table 11.3 shows the resulting acceleration forces calculated from Equation 11.12.

These forces cannot be compared to the stresses calculated in previous sections without knowing the area over which the force is distributed. All previous stress calculations were made in the mid-plane of a spherical particle therefore this force will be divided by the mid-plane area. The stress in the mid-plane, due to the acceleration force, is also given in Table 11.3.

Table 11.3: Mid-Plane Stress in a Single Spherical Particle due to Acceleration

Nozzle	a Figure 7.4 (m/s ²)	F Eqn. 11.12 (N)	$\sigma_{\text{midplane area}}$ $\sigma = F/A$ (Pa)
Abrupt	6.60E+06	1.38E-09	7.04E+03
Converging-Diverging	1.05E+07	2.20E-09	1.12E+04
Converging	1.15E+06	2.41E-10	1.23E+03

11.4.4 Stresses within a Single Spherical Particle in Turbulent Flow

Deaggregation is also attributed to energy transferred to aggregates through turbulence. Kousaka et al. (1979) derive expressions for the mid-plane stresses found in spherical particles in turbulence. These theoretical stresses are given by Equations 4.10 through 4.12. Each of these equations contains the symbol ε that represents the turbulent energy dissipation rate. It can be considered as the energy transferred to a particle through turbulent eddies. The values for energy dissipation can be found for the three experimental nozzles in Figure 7.9. Plugging in the values of ε , $\rho_f = 1.2 \text{ kg/m}^3$, $\nu = 1.5E-5 \text{ m}^2/\text{s}$, $c_1 = 1$, and $d_p = 0.5 \mu\text{m}$, into Equations 4.10 through 4.12 give the stresses shown in Table 11.4.

Table 11.4: Mid-Plane Stresses in a Spherical Particle in Turbulent Flow

Nozzle	ε Figure 7.9 (m^2/s^3)	$\tau_{\text{max,large particle}}$ Eqn. 4.10 (Pa)	$\tau_{\text{max,small particle}}$ Eqn. 4.11 (Pa)	$\sigma_{\text{max, bending, small particle}}$ Eqn. 4.12 (Pa)
Abrupt	3.00E+06	5.53E-01	2.50E+01	8.69E+01
Converging-Diverging	7.00E+06	9.73E-01	3.81E+01	1.33E+02
Converging	5.00E+06	7.78E-01	3.22E+01	1.12E+02

The stresses given in Table 11.4 are for the mid-plane of a spherical particle in turbulent flow. The subscripts, large particle and small particle, refer to the size of the particle relative to the turbulent size scale. A large particle in this case means the particle is large compared to the turbulent size scale. Small particle suggests the size of the particle is similar to the turbulent size scale.

11.4.5 Comparison of Stresses within a Single Spherical Particle

The previous four sections have been used to calculate the maximum mid-plane stresses in a single spherical particle in uniform, shear, accelerating, and turbulent flow. Table 11.5 shows all of these stresses together for the purpose of comparison.

Table 11.5: Comparison of Stresses within a Single Spherical Particle

Nozzle	Uniform Flow, i.e. acceleration	Shear Flow	Turbulent Flow
--------	---------------------------------	------------	----------------

	$\sigma_{\max}=\tau_{\max}$ Eqn. 4.1 (Pa)	σ_{\max} Eqn. 11.12 (Pa)	σ_{\max} Eqn. 4.2 (Pa)	τ_{\max} Eqn. 4.3 (Pa)	$\tau_{\max, \text{large part.}}$ Eqn. 4.10 (Pa)	$\tau_{\max, \text{small part.}}$ Eqn. 4.11 (Pa)	$\sigma_{\max, \text{bending, small part.}}$ Eqn. 4.12 (Pa)
Abrupt	8.18E+03	7.04E+03	1.09E+01	1.85E+01	5.53E-01	2.50E+01	8.69E+01
Converging-Diverging	1.64E+04	1.12E+04	1.36E+01	2.31E+01	9.73E-01	3.81E+01	1.33E+02
Converging	8.18E+03	1.23E+03	1.27E+01	2.15E+01	7.78E-01	3.22E+01	1.12E+02

The two stresses under uniform flow, i.e. accelerating flow, show excellent agreement. This makes sense. The first compressive stress was derived by Bagster and Tomi (1974) for a particle initially put into uniform flow. The uniform flow velocities from the CFD simulations were used in this calculation. The second stress is based on the CFD calculated acceleration, which is then coupled with Newton's second law to give a force. Both stresses are distributed over the mid-plane area of the spherical particle.

The mid-plane stresses in uniform flow, i.e. accelerating flow, are nearly two orders of magnitude larger than any other stress in the table. The second largest stress is in turbulent flow when the particle is on the same size scale as the turbulent structure. Acceleration will be concluded the most significant cause of internal stress in the mid-plane of a single spherical particle.

11.5 Deaggregation Stresses in an Aggregate

Kousaka et al. (1979) also derived expressions for the theoretical stresses developed in aggregates of two spherical particles in shear and uniform flow. These stresses will be calculated in this section utilizing CFD simulated flow data. Calculations can be found in greater detail in Appendix C.

11.5.1 Stresses within an Aggregate in Uniform Flow

Kousaka et al. calculated theoretical stresses for aggregates in uniform flow. The internal stresses in the aggregate are caused by a differential drag force. The large particle is subjected to a larger drag force and thus an internal force is required to maintain equal acceleration between the two particles. This scenario is depicted in Figure 4.1.

Assuming a particle size ratio of 2:1, e.g. $d_{pB} = 0.5 \mu m$ and $d_{pA} = 0.25 \mu m$, the interaction force, F , maximum tensile stress, $\sigma_{\max, \text{tensile}}$, maximum shear stress, τ_{\max} , and maximum bending stress, $\sigma_{\max, \text{bending}}$, for an aggregate in uniform flow can be calculated with Equations 4.5 through 4.7. These stresses are shown in Table 11.6 assuming $c_1 = 1$. Figure 11.2 shows the aggregate for which $c_1 = 1$. The contact area is equal to the mid-plane area of particle A.

Table 11.6: Stresses within an Aggregate in Uniform Flow

Nozzle	u_r Figure 7.2 (m/s)	F Eqn. 4.5 (N)	$\tau_{\max} = \sigma_{\max, \text{tensile}}$ Eqn. 4.6 (Pa)	$\sigma_{\max, \text{bending}}$ Eqn. 4.7 (Pa)
Abrupt	75.3	2.14E-09	4.36E+04	1.75E+05
Converging-Diverging	151.3	4.30E-09	8.76E+04	3.51E+05
Converging	75.3	2.14E-09	4.36E+04	1.75E+05

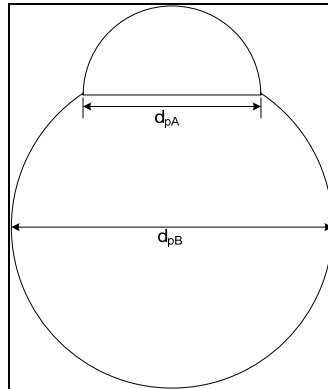


Figure 11.2: Aggregate for which the Adhesion Constant is Unity

Remember, c_1 is a constant that varies from zero to unity depending on the manner of adhesion. If the constant is reduced from unity, the stresses get larger. Reducing the constant from unity may be thought of as reducing the area of contact. The bending stress would be infinite as the area of contact approaches zero. This implies the values of the stresses in Table 11.6 are the minimum stresses for aggregates in uniform flow.

11.5.2 Stresses within an Aggregate in Shear Flow

Kousaka et al. (1979) derived the bending stress produced in an aggregate in simple shear flow. They claimed it is much greater than the shearing stress produced in shear flow. Therefore, the shearing stress will not be calculated. Equation 4.8,

$$\sigma_{\max} \approx \frac{93\mu\gamma}{\pi c_1^3}, \quad (11.14)$$

is an approximation for the bending stress in an aggregate in a simple shear flow. The strain rates for each experimental nozzle, γ , are taken from Figure 7.8.

Assuming $c_1 = 1$, the bending stress, σ_{\max} , produced in an aggregate in shear flow is given in Table 11.7. The value of the constant is unity. This implies the values in Table 11.7 are the minimum values of bending stress.

Table 11.7: Bending Stress Produced in an Aggregate in Simple Shear Flow

Nozzle	γ_{\max} Figure 7.8 (1/s)	σ_{\max} Eqn. 4.8 (Pa)
Abrupt	1.20E+05	64.3
Converging-Diverging	1.50E+05	80.4
Converging	1.40E+05	75.0

11.5.3 Comparison of Stresses in an Aggregate

Tables 11.6 and 11.7 are simplified and combined into Table 11.8 to show the relative magnitudes of stresses within aggregates in shear and uniform flow.

Table 11.8: Comparison of Deaggregation Stresses in an Aggregate of Two Particles

Nozzle	Uniform Flow		Shear Flow
	$\tau_{\max} = \sigma_{\max, \text{tensile}}$ Eqn. 4.6 (Pa)	$\sigma_{\max, \text{bending}}$ Eqn. 4.7 (Pa)	σ_{\max} Eqn. 4.8 (Pa)
Abrupt	4.36E+04	1.75E+05	6.43E+01
Converging-Diverging	8.76E+04	3.51E+05	8.04E+01
Converging	4.36E+04	1.75E+05	7.50E+01

The theory developed by Kousaka et al. (1979) suggest that aggregates in uniform flow experience much greater internal forces than aggregates in simple shear flow. Table 11.8 shows a three to four order of magnitude difference between the maximum bending stresses in an aggregate in uniform flow and an aggregate in shear flow. Acceleration of aggregate particles will be concluded as the dominant cause of deaggregation from these calculations.

11.6 Surface Interaction Energies and Forces

The van der Waals forces between NanoActive™ MgO particles will be considered in this section. Derivations for surface interaction energies and forces made by Israelachvili (1985) will be used to quantify the van der Waals interactions between particles.

11.6.1 Calculation of London Dispersion Coefficient

The London Dispersion Coefficient is given by Equation 3.6 and repeated here,

$$C = \frac{3}{4} \frac{\alpha_o^2 h\nu}{(4\pi\epsilon_o)^2}. \quad (11.15)$$

The Clausius-Mossotti Equation gives

$$\frac{\alpha_o}{4\pi\epsilon_o} = \frac{3}{4\pi N} \left(\frac{\kappa - 1}{\kappa + 2} \right), \quad (11.16)$$

where N is the number density of the solid and κ is the dielectric constant (Ashcroft and Mermin 1976). The dielectric constant for MgO can be found in the CRC Handbook of Chemistry and Physics, $\kappa_{MgO} = 9.65$. The number density of MgO can be found using the density, molecular weight, and Avagadro's Number,

$$N = \frac{3.58 \cdot 10^6 \text{ g} / \text{m}^3}{40.3 \text{ g} / \text{mol}} \cdot 6.023 \cdot 10^{23} \frac{\text{molecules}}{\text{mol}} = 5.35 \cdot 10^{28} \frac{\text{molecules}}{\text{m}^3}. \quad (11.17)$$

Plugging the result from Equation 11.17 into Equation 11.16 gives $\frac{\alpha_o}{4\pi\epsilon_o} = 3.31 \cdot 10^{-30} \text{ m}^3$.

The first ionization potential of MgO can also be found in the CRC Handbook of Chemistry and Physics, $h\nu = 1.403 \cdot 10^{-18} \text{ J}$. Finally, Equation 11.15 can be solved for the London Dispersion Coefficient of MgO, $C = 116 \cdot 10^{-79} \text{ J} \cdot \text{m}^6$. The surface interaction energies presented in Chapter 3 may now be calculated using this result.

11.6.2 Energy and Force Calculations

Some of the interaction energies that arise between NanoActive™ MgO particles due to van der Waals forces will be approximated in this section. Additional details of the calculations can be found in Appendix C.

A separation distance must be known to use the equations presented in Chapter 3. The smallest possible separation, yielding the largest interaction energies, is the interatomic spacing. The interatomic spacing for MgO is $D = 2.1 \cdot 10^{-10} \text{ m}$. The number density, ρ , in Equations 3.5 through 3.8 is the same as N , calculated in the previous section. The primary particles of NanoActive™ MgO are approximately $0.5 \text{ }\mu\text{m}$ in diameter. All models will be based on this dimension.

11.6.2.1 Spherical Particle Interacting with an Infinite Plane

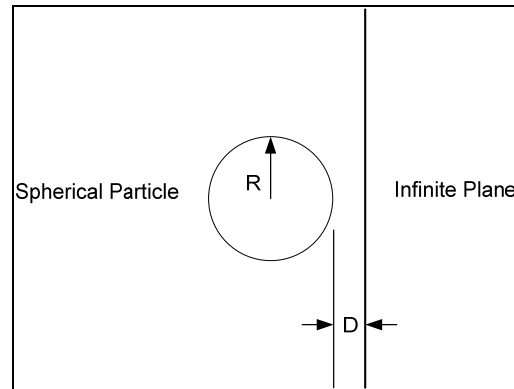


Figure 11.3: Spherical Particle Interacting with an Infinite Plane

Figure 11.3 depicts the scenario of a spherical particle interacting with an infinite plane. The energy of interaction, $W(D)$, for a spherical particle, $R = 0.25 \cdot 10^{-6} \text{ m}$, with an infinite planar surface is $W(D) = -6.5 \cdot 10^{-17} \text{ J}$. This energy is calculated from Equation 3.7. To find the interaction energy between two spheres of equal radii, $R = 0.25 \cdot 10^{-6} \text{ m}$, the result from Equation 3.7 is divided by 2, $W(D) = -3.25 \cdot 10^{-17} \text{ J}$.

11.6.2.2 Planar Area Interacting with an Infinite Plane

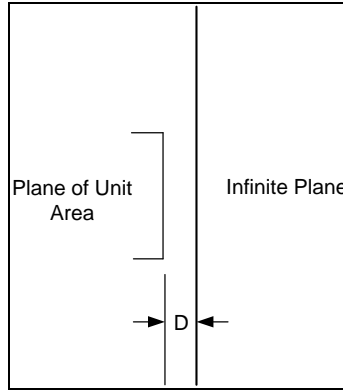


Figure 11.4: Plane of Unit Area Interacting with an Infinite Plane

The interaction energy between a planar surface of finite dimension with an infinite planar surface, given by Equation 3.8, is $W(D)_{\text{per unit area}} = -0.197 J / m^2$. This result is true as long as the lateral dimensions of the plane are much greater than the separation distance. For a square plane of dimension $L = 0.5 \cdot 10^{-6} m$, the interaction energy is $W(D) = -4.9 \cdot 10^{-14} J$. This interaction energy is three orders of magnitude larger than the interaction energy of two spheres of similar size.

11.6.2.3 Derjaguin Approximation for Force Between Two Spheres

It is useful to know the interaction force rather than energy. The Derjaguin Approximation, Equation 3.9, relates the interaction force between two spherical particles to the planar interaction energy at a given separation distance. For $R_1 = 0.25 \cdot 10^{-6} m$, and $R_2 = 0.125 \cdot 10^{-6} m$, Equation 3.9 yields $F(D) = -1.0 \cdot 10^{-7} N$. For two spheres of equal radii, $R = 0.25 \cdot 10^{-6} m$, the interaction force is $F(D) = -1.6 \cdot 10^{-7} N$. To compare this to the deaggregation stresses calculated in previous sections, this force will be put into units of stress. It will be divided by the mid-plane area of a sphere of radius $R = 0.25 \cdot 10^{-6} m$. The resulting force per unit area is $F_{\text{per unit area}}(D) = -7.9 \cdot 10^5 Pa$.

11.7 Comparison of Deaggregation and Cohesive Forces

Theoretical stresses derived by Kousaka et al. and Bagster and Tomi were coupled with CFD results to obtain numerical values for stresses within NanoActive™ MgO particles

and aggregates. The stresses produced by simple shear flow were the smallest. The next largest deaggregation stresses were caused by turbulence. By far, the highest numerical results for internal aggregate and particle stresses were for accelerations in uniform flow. The Derjaguin Approximation yielded an attractive force per unit area of $8 \cdot 10^5 Pa$ for two spheres of radii $0.25 \mu m$. The only deaggregation stresses that approach this interaction energy are those induced by acceleration.

11.8 Deaggregation as a Function of Particle Size and Structure

It seems intuitive that deaggregation and cohesion are dependent upon particle geometry and structure. However, quantifying that geometrical and structural dependence can be difficult. The study by Froeshke et al. (2003) suggests that fractal aggregate strength increases as primary particle size decreases. Similar results have been found in this study for NanoActive™ MgO and MgO Plus aggregates although they have a non-fractal morphology.

Figure 10.6 shows the light scattering data for an aerosol of NanoActive™ MgO. The data show a significant increase in deaggregation as a function of pressure. Figure 10.7 shows light scattering data for an aerosol of NanoActive™ MgO Plus subjected to the same aerodynamic deaggregation forces. There is no dependence of the NanoActive™ MgO Plus size distribution on pressure. The aerosol particles are made of the same chemical compound and exposed to the same forces. The only thing that can explain the difference in deaggregation is the structure of the particles. NanoActive™ MgO primary particles are microcrystalline platelets, roughly 0.25 to $0.5 \mu m$ in diameter and $8 nm$ thick, that come together to form aggregates and agglomerates. NanoActive™ MgO Plus primary particles are nanocrystalline cubes on the order of $5 nm$. These cubes form chains and the chains form agglomerates that resemble cotton balls. The deaggregation forces as well as the cohesive interactions will be explored in this section in an effort to explain the dependence of deaggregation on primary particle size and structure.

11.8.1 Deaggregation

For this discussion consider acceleration the only cause of deaggregation. Assume two aggregates: one NanoActive™ MgO aggregate with particle diameters $d_{pA} = 0.5 \mu m$ and $d_{pB} = 0.55 \mu m$, and one NanoActive™ MgO Plus aggregate with $d_{pA} = 5 nm$ and $d_{pB} = 5.5 nm$. Both sets of aggregate particles are 10% different in size.

Following Kousaka's theory for aggregates in uniform flow, the NanoActive™ MgO Plus aggregate experiences internal stresses two orders of magnitude larger than the NanoActive™ MgO aggregate. See calculations in Appendix C for additional details.

Now consider the theories for a single spherical particle in uniform and accelerating flow. The NanoActive™ MgO spherical particle will have a diameter of $0.5 \mu m$ and the NanoActive™ MgO Plus spherical particle will have a diameter of $5 nm$. The NanoActive™ MgO Plus particle will experience an internal stress two orders of magnitude larger than the NanoActive™ MgO particle using the equation for mid-plane stress from Bagster and Tomi.

Now apply the bulk acceleration analysis that utilizes Newton's second law and the mid-plane area of the sphere. This theory for mid-plane stress in a spherical particle suggests that a NanoActive™ MgO particle experiences internal stresses two orders of magnitude higher than the NanoActive™ MgO Plus particle. This result contradicts the theories presented by Bagster and Tomi and Kousaka et al. These calculations may also be found in Appendix C.

These results contradict each other and do not seem to present any definite answers as to why experiments show aggregates consisting of small primary particles are stronger than those consisting of larger particles. Both Kousaka et al. and Bagster and Tomi imply the MgO Plus aggregate experiences larger internal stresses. The results for NanoActive™ MgO Plus particles are somewhat questionable due to the size of the particles. At $5 nm$

the assumptions made in the derivations made by Kousaka et al. and Bagster and Tomi may not hold.

Our experiments show NanoActive™ MgO Plus aggregates are stronger than NanoActive™ MgO aggregates. The comparison, above, of the deaggregation stresses in aggregates of NanoActive™ MgO and MgO Plus was inconclusive. The cohesive interactions and agglomerated structures will now be considered as the source of strength of aggregates with smaller primary particles.

11.8.2 Cohesion

Equation 3.7 clearly indicates the energy of interaction is proportional to the size of the two spheres. The NanoActive™ MgO aggregate would experience a greater vdW force of interaction than a NanoActive MgO Plus aggregate if aggregates of two primary particles were considered. This also seems to contradict the results. There must be something causing a greater cohesive force in the NanoActive™ MgO Plus particle for it to maintain its agglomerated structure during the dispersion process. The first obvious point of contention is that the particles are not spheres.

The separation distance was crucial to the calculations for interaction energies. Assuming the NanoActive™ MgO Plus primary particles are separated by one interatomic distance may be accurate due to the structure of the primary particles. The primary particles are small enough to be highly-ordered crystalline structures. The faces are assumed very flat with small surface asperities. The primary particles have been imaged by a high resolution TEM and can be seen in Figure 2.1.

It is doubtful this is the case for NanoActive™ MgO particles. Even though the NanoActive™ MgO particles are described as platelets, surface asperities of unknown magnitude make it difficult to approximate surface separations and areas of contact. This, potentially, could be a major difference in strength between NanoActive™ MgO and MgO Plus particles.

The van der Waals forces become maximum as the separation distance approaches the interatomic distance. It is also thought that separation distances of this magnitude may allow for some ionic bonding of NanoActive™ MgO Plus primary particles. This would dramatically increase the strength of such aggregates.

It must also be considered that the agglomerated structure of NanoActive™ MgO Plus provides additional strength. Imagine a cotton ball. One fiber of the cotton ball may be weak by itself. However, when many fibers are combined, intertwined and woven together, they possess strength much greater than any individual fiber. This is analogous to the structure of a NanoActive™ MgO Plus agglomerate. Consider one aggregate, 5 nm cubes that form a tenuous chain. The vdW forces of interaction are potentially smaller than that of an agglomerate of NanoActive™ MgO primary particles due to their small size. This aggregate may possess very little strength to withstand the forces of deaggregation. When these chains come together to form an agglomerate they potentially possess great strength. Any force applied to the overall structure could be distributed throughout the agglomerate due to its interdependent structure. The opposite is true for NanoActive™ MgO agglomerates. The loosely packed primary particles occupy space in whatever fashion geometrically possible. The agglomerate is comprised of primary particles at odd angles with each other, limiting the interaction area, making them easier to break apart.

12 CONCLUSION

NanoActive™ metal oxide powders have been developed that possess very high specific surface areas as well as large concentrations of highly reactive edge and defect sites. These two characteristics make them ideal chemical adsorbents. They can be used to destroy hazardous waste materials as well as chemical and biological weapons agents. The dispersion of these powders as aerosols is being engineered to remediate contaminated environments as well as counteract foreign and domestic terrorist attacks.

The particle size distributions within these aerosols are key to their effective use in different situations. Some applications may require larger particles while others are more aptly suited by the smallest of particles. An understanding of particle cohesion and deaggregation is essential to engineering devices used in such applications.

Particle cohesion is mainly caused by capillary, electrostatic, and van der Waals forces of interaction. These forces were studied in this thesis to gain a better understanding of the cohesive nature of aerosol particles. Van der Waals forces of interaction were concluded the most likely cause of particle cohesion in the powders used in this study. The van der Waals interactions were then quantified with models of simple geometries like spheres and planes.

Aerosol particles may also deaggregate during the dispersion process because of aerodynamic forces or impacting obstacles in the flow. Past research suggests four main deaggregation mechanisms: particle acceleration in uniform flow, particles in shear flow, particles in turbulence, and particles impacting objects in the flow. These deaggregation mechanisms were explored experimentally and theoretically in this study to determine which, if any, were the dominant cause of deaggregation of aerosol particles.

Four nozzles were designed to experimentally determine which of the four deaggregation mechanisms were the dominant cause, or causes, of particle deaggregation. A nozzle with three wire meshes was designed to create an environment conducive to impaction.

A nozzle with an abrupt orifice in the flow seemed to possess all four deaggregation mechanisms, thus, was broken down into two similar nozzles. The third nozzle was a converging-diverging nozzle. This nozzle was designed to eliminate the possibility of impaction occurring at the orifice face. The converging-diverging nozzle throat area was the same as the abrupt orifice. The exiting aerosol was somewhat shielded from the turbulent effects that were present at the abrupt orifice exit. Another nozzle was created to eliminate the possibility of impaction but retain the exit effects, large velocity gradients and turbulence, seen in the abrupt orifice. NanoActive™ MgO and other materials were dispersed through all four nozzles to determine which of the nozzles were most effective at deaggregating aerosol particles.

The abrupt orifice, converging-diverging nozzle, and converging nozzle all seemed to effectively break up the NanoActive™ MgO particles as the pressure drop across the nozzle increased. No significant differences in the degrees of deaggregation, between the nozzles, were seen from light scattering data. The data suggested the NanoActive™ MgO aerosols consisted of two modes: one of large particles, roughly 5 μm in diameter, and another roughly 0.5 μm in diameter. A significant increase in the number of small particles was seen as the pressure increased. The small particles were assumed to be primary particles of NanoActive™ MgO.

The experiment was repeated for the mesh nozzle. The degree of deaggregation was less significant in this nozzle and attributed to the lack of impaction and smaller particle acceleration. With particles smaller than 10 μm , the air velocities in this experiment were not high enough to cause impaction. Coupling this result with Stokes impaction theory for orifice flow, impaction in the orifice was ruled out as a significant cause of deaggregation.

Fluent simulations for each of the nozzles were performed at 0.5 psi pressure drop across the nozzle. Maximum accelerations, strain rates, and turbulent energy dissipation rates were acquired to quantify the theoretical internal stresses in particles corresponding to the remaining deaggregation mechanisms: shear flow, turbulent flow, and accelerating flow.

The internal stresses presented by Kousaka et al. (1979) and Bagster and Tomi (1974) were calculated utilizing the data gathered from CFD simulations. According to theory, the acceleration of particles creates internal stresses nearly 3 orders of magnitude higher than shear flow and turbulent flow. Without the presence of impaction in the flow, acceleration was concluded the most likely cause of deaggregation in this set of experiments.

Another set of measurements was taken for an aerosol of NanoActive™ MgO Plus. No deaggregation was seen for the entire range of pressures. The materials are chemically identical. However, NanoActive™ MgO and MgO Plus are distinctly different when viewed on the structural level. Due to the differences in their production, NanoActive™ MgO Plus primary particles are 5 nm cubes whereas NanoActive™ MgO primary particles are platelets less than 500 nm in diameter and 10 nm thick. This structural difference was seen as a major contributor to the strength of NanoActive™ MgO Plus particles.

The aggregates of NanoActive™ MgO did not appear to have significant structural order. For lack of a better term, they were hunks of NanoActive™ MgO primary particles that had come together in whatever way geometrically possible. This random order seemed to reduce the area of contact between the primary particles, i.e. limit the van der Waals forces of interaction. On the other hand, the NanoActive™ MgO Plus particles appeared to be highly ordered. The flat surfaces of the individual nanocrystals allowed for substantial vdW forces of interaction. The nanocrystals formed aggregates analogous to individual fibers in a cotton ball. The overall agglomerate of NanoActive™ MgO Plus was a highly interdependent structure of woven and intertwined aggregates. The significant strength of NanoActive™ MgO Plus agglomerates was attributed to this structure.

The lessons learned during the course of this study make particle control seem less practical than originally perceived. NanoActive™ MgO particles could be broken down into their constituent primary particles, but there was no middle ground. Either the

particles were large or the particles were small. These particles appear to be nearly completely deaggregated at even small pressures. NanoActive™ MgO Plus is at the other extreme. No matter how vigorous of aerodynamic forces the particles were exposed to, none seemed to deaggregate. In this case it seems no degree of control is achievable due to the structural properties of the aggregates and agglomerates. In summary, universal control appears to be more of an ideal than reality. Materials must be evaluated on a case by case basis to determine if particle size control is reasonable. Primary particle size and shape, agglomerated structure, and chemical and physical properties must all be considered when evaluating potential particle deaggregation.

Additional experiments could provide greater understanding of some of the topics discussed in this thesis. Impaction was ruled out as a significant cause of deaggregation in these experiments. Some authors suggest impaction creates much higher internal stresses than acceleration. Other devices could be designed to maximize the occurrence of particles hitting obstacles in the flow. These forces could be large enough to break apart NanoActive™ MgO Plus particles. Another idea for future experimentation is to create a supersonic flow with a shock wave in the exit region. A shock wave, theoretically, would be the most violent region for aerosol particles to pass through. It would be interesting to see the degree of deaggregation of aerosol particles passing through a shock wave and on to supersonic flows.

REFERENCES

- Adrian, R.J. (2005). Twenty Years of Particle Image Velocimetry, *Experiments in Fluids* 39:159-169.
- Ashcroft, N.W., Mermin, N.D. (1976). *Solid State Physics*. Holt, Rinehart and Winston, New York, pp. 826.
- Bagster, D.F., Tomi, D. (1974). Stresses within a Sphere in Simple Flow Fields, *Chemical Engineering Science* 29:1773-1783.
- Bailey, A.G. (1993). Charging of Solids and Powders, *Powder Technology* 30:167-180.
- Bailey, A.G. (1983). Electrostatic Phenomena During Powder Handling, *Powder Technology* 37:71-85.
- Begat, P., et al. (2004). The Cohesive-Adhesive Balances in Dry Powder Inhaler Formulations I: Direct Quantification by Atomic Force Microscopy, *Pharmaceutical Research* 21(9):1591-1597.
- Begat, P, et al. (2004). The Cohesive-Adhesive Balances in Dry Powder Inhaler Formulations II: Direct Quantification by Atomic Force Microscopy, *Pharmaceutical Research* 21(10):1826-1833.
- Bentham, A.C., et al. (2004). Fluidised-Bed Jet Milling of Pharmaceutical Powders, *Powder Technology* 141:233-238.
- Berg, M.J., et al. (2005). Patterns in Mie scattering: Evolution when normalized by the Rayleigh cross section, *Applied Optics* 44:7487-7493.
- Ferri, F. (1997). Use of a Charge Coupled Device Camera for Low-Angle Elastic Light Scattering, *Review of Scientific Instruments* 68:2265-2274.
- Finlay, W.H. (2001). *The Mechanics of Inhaled Pharmaceutical Aerosols: An Introduction*, Academic Press, San Diego, pp. 221-275.
- Froeschke, S., et al. (2003). Impact Fragmentation of Nanoparticle Agglomerates, *Journal of Aerosol Science* 34: 275-287.
- Giancoli, D.C. (1998). *Physics, 5th ed.* Prentice Hall, Upper Saddle River, New Jersey, pp. 667.
- Han, R., et al. (2002). Flow Field Measurement Inside the Mouthpiece of the Spiros Inhaler Using Particle Image Velocimetry, *Aerosol Science and Technology* 36: 329-341.

- Hart, D.P. (1999). Super-Resolution PIV by Recursive Local-Correlation, *Journal of Visualization* 10:1-10.
- Hickey, A.J., et al. (1994). Factors Influencing the Dispersion of Dry Powders as Aerosols, *Pharmaceutical Technology* 18:58-82.
- Hinds, William C. (1999). *Aerosol Technology*. John Wiley and Sons, New York, pp. 483.
- Israelachvili, J.N. (1985). *Intermolecular and Surface Forces*. Academic Press, New York, pp. 296.
- Keane, R.D., and Adrian, R.J. (1992). Theory of Cross-Correlation Analysis of PIV Images, *Applied Scientific Research* 49:191-215.
- Klabunde, K.J., et al. (1996). Nanocrystals as Stoichiometric Reagents with Unique Surface Chemistry, *Journal of Physical Chemistry* 100:12142-12153.
- Kousaka, Y., et al. (1979). Dispersion Mechanism of Aggregate Particles in Air, *Journal of Chemical Engineering of Japan* 12(2):152-159.
- Kwetkus, B.A. (1998). Particle Triboelectrification and its Use in the Electrostatic Separation Process, *Particulate Science and Technology* 16:55-68.
- Laitinen, N., Juppo, A. (2003). Measurement of Pharmaceutical Particles Using a Time-of-Flight Particle Sizer, *European Journal of Pharmaceutics and Biopharmaceutics* 55: 93-98.
- Lide, D.R. ed. (1996). *CRC Handbook of Chemistry and Physics*. CRC Press, New York.
- Lucas, E., et al. (2001). Nanocrystalline Metal Oxides as Unique Chemical Reagents/Sorbents, *Chemistry – A European Journal* 7:2505-2510.
- Lucas, E., and Klabunde, K.J. (1999). Nanocrystals as Destructive Adsorbants for MIMCS of Chemical Warfare Agents. *Nanostructured Materials* 12:179-182.
- Lumme, K., Rahola, J. (1998). Comparison of Light Scattering by Stochastically Rough Spheres, Best Fit Spheroids and Spheres, *Journal of Quantitative Spectroscopy and Radiative Heat Transfer* 60:439-450.
- Mel'gunov, M.S., et al. (2003). Textural Changes during Topochemical Decomposition of NanoCrystalline Mg(OH)₂ to MgO, *The Journal of Physical Chemistry B* 107(11): 2427-2434.

- Melling, A. (1997). Tracer Particles and Seeding for Particle Image Velocimetry, *Measurement Science and Technology* 8(12): 1406-1416.
- Mendes, P.J., et al. (2004). Sizing of Powders in Inhalers with an Aerosizer According to a Mixed Experimental Factorial Design, *Journal of Aerosol Science* 35: 509-527.
- Murtomaa, M., et al. (2005). A Device for Aerosol Charge Measurement and Sampling, *Journal of Electrostatics* 63:571-575.
- NanoScale Materials Inc. 2005 August 18. Material Data Information. Website. <<http://www.nanoactive.com>>.
- Nomura, T., et al. (2003). The Environment Humidity Effect on the Tribo-Charge of Powder, *Powder Technology* 135:43-49.
- Powder Technology Inc. 2006 May 5. Powder Technology Inc. Website. <<http://www.powdertechologyinc.com>>.
- Raffel, M., et al. (1998). *Particle Image Velocimetry: A Practical Guide*. Springer, Berlin, New York, pp. 253.
- Rajagopalan, S., et al. (2002). Nanocrystalline Metal Oxides as Destructive Adsorbents for Organophosphorous Compounds at Ambient Temperatures, *Chemistry – A European Journal* 8(11):2602-2607.
- Sorensen, C.M., Fishchbach, D.J. (2000). Patterns in Mie Scattering, *Optics Communications* 173:145-153.
- Sorensen, C.M. (2003). *Handbook of Surface and Colloid Chemistry*, K.S. Birdi ed., CRC Press, New York, 623-652.
- Sorensen, C.M. (2001). *Aerosol Measurement: Principles, Techniques, and Applications*, Baron and Willeke eds., Wiley, New York, 705-725.
- Sorensen, C.M., Shi, D. (2000). Guinier Analysis for Homogeneous Dielectric Spheres of Arbitrary Size, *Optics Communications* 178:31-36.
- Tsubaki, J., Jimbo, G. (1979). Mechanism of the Failure of Aggregates in Flow Field, *Journal of Chemical Engineering of Japan* 12(3):250-251.
- Utamapanya, S., et al. (1991). Nanoscale Metal Oxide Particles/Clusters as Chemical Reagents Synthesis and Properties of Ultrahigh Surface Area Magnesium Hydroxide and Magnesium Oxide, *Chemistry of Materials* 3:175-181.
- Velander, N. (2005 July 8). 10089 Hollow Glass Spheres Specs [Personal Email].

Voss, A., Finlay, W.H. (2002). Deagglomeration of Dry Powder Pharmaceutical Aerosols, *International Journal of Pharmaceutics*, 248:39-50.

Wurm, G., et al. (2004). Light Scattering Experiments with Micron-Sized Dust Aggregates: Results on Ensembles of SiO₂ Monospheres and of Irregularly Shaped Graphite Particles, *Journal of Quantitative Spectroscopy and Radiative Heat Transfer* 89:371-384.

Yoshida, T., et al. (1979). *Aerosol Science for Engineers – Condensation, Coagulation, and Dispersion*. Power Co., Tokyo, pp. 159-193.

Zerull, R.H., et al. (1977). Scattering Measurements of Irregular Particles vs. Mie Theory, *Optical Polarimetry* 112:191-199.

APPENDIX A: AEROSOL GENERATOR DRAWINGS

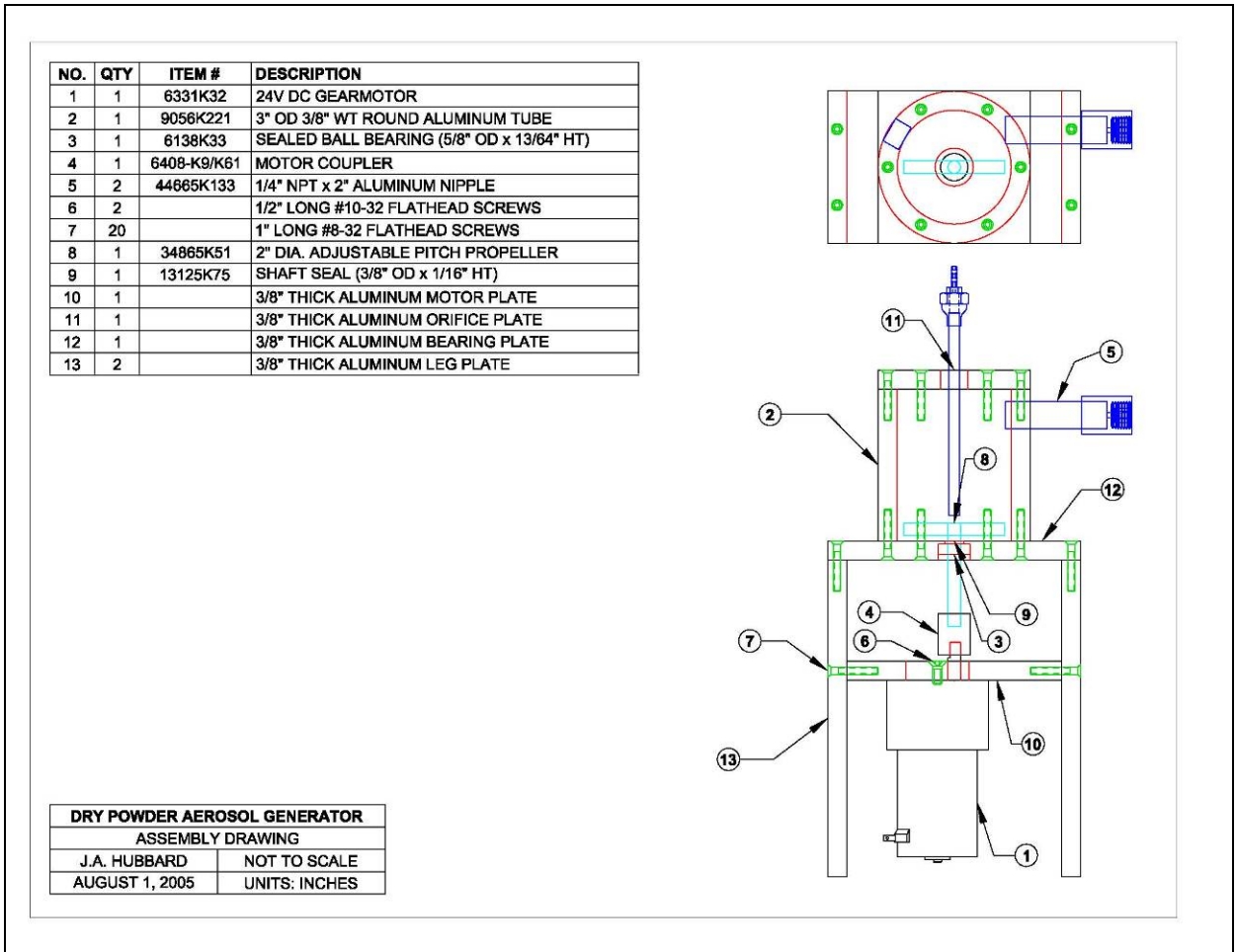


Figure A. 1: Aerosol Generator Assembly Drawing

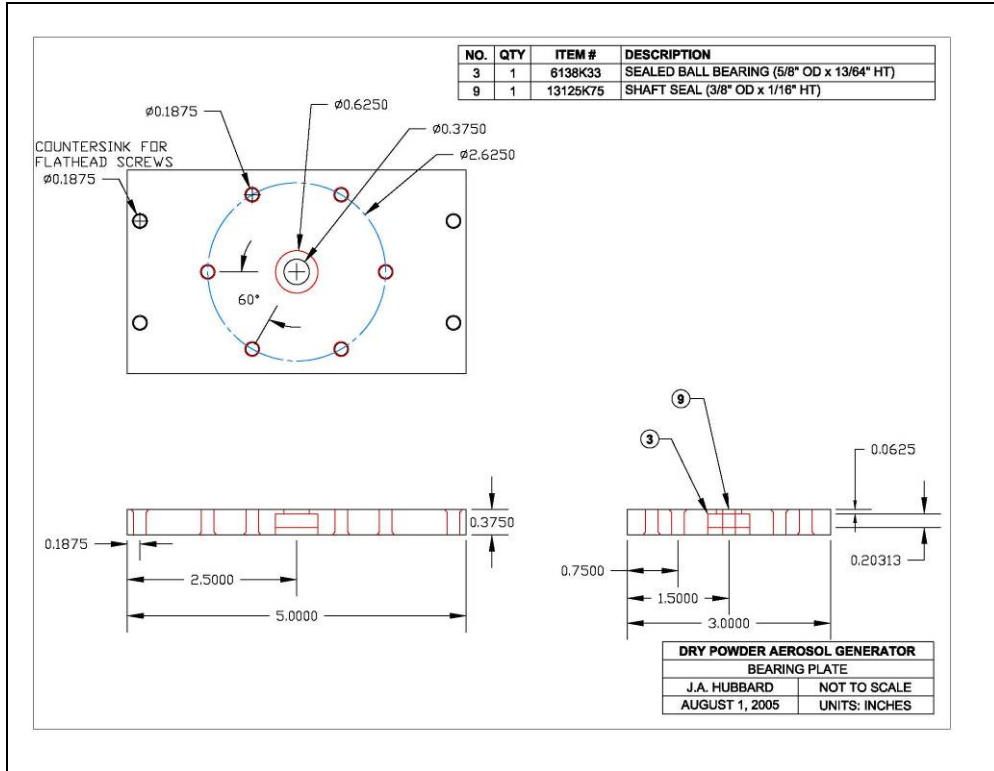


Figure A. 2: Aerosol Generator Bearing Plate

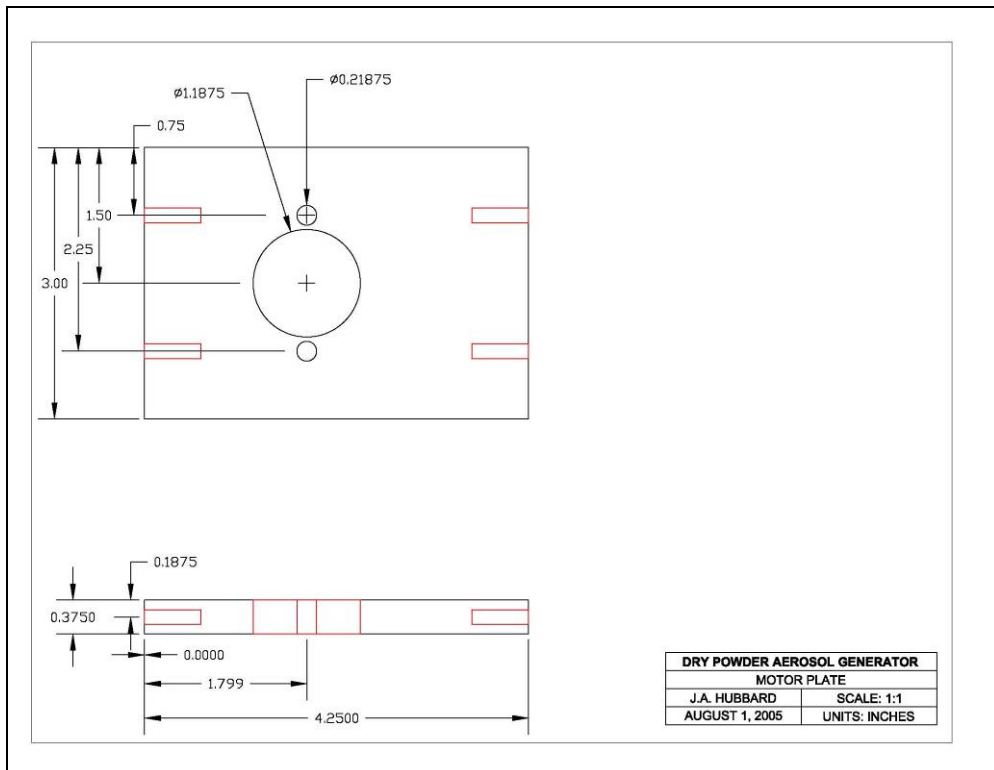


Figure A. 3: Aerosol Generator Motor Plate

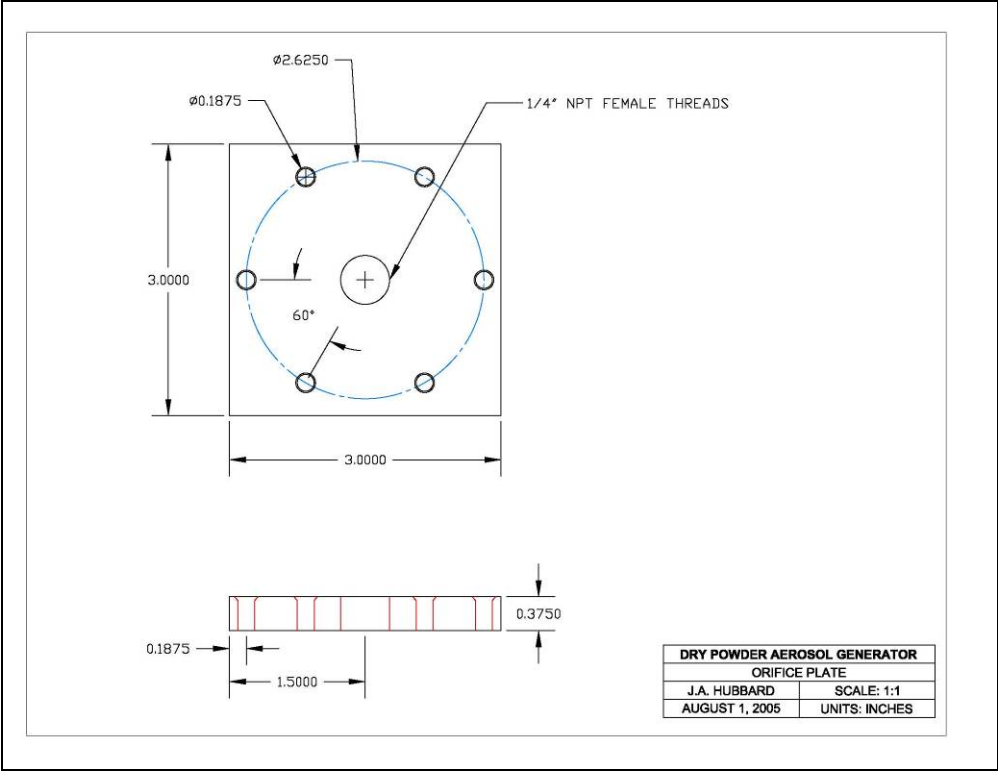


Figure A. 4: Aerosol Generator Orifice Plate

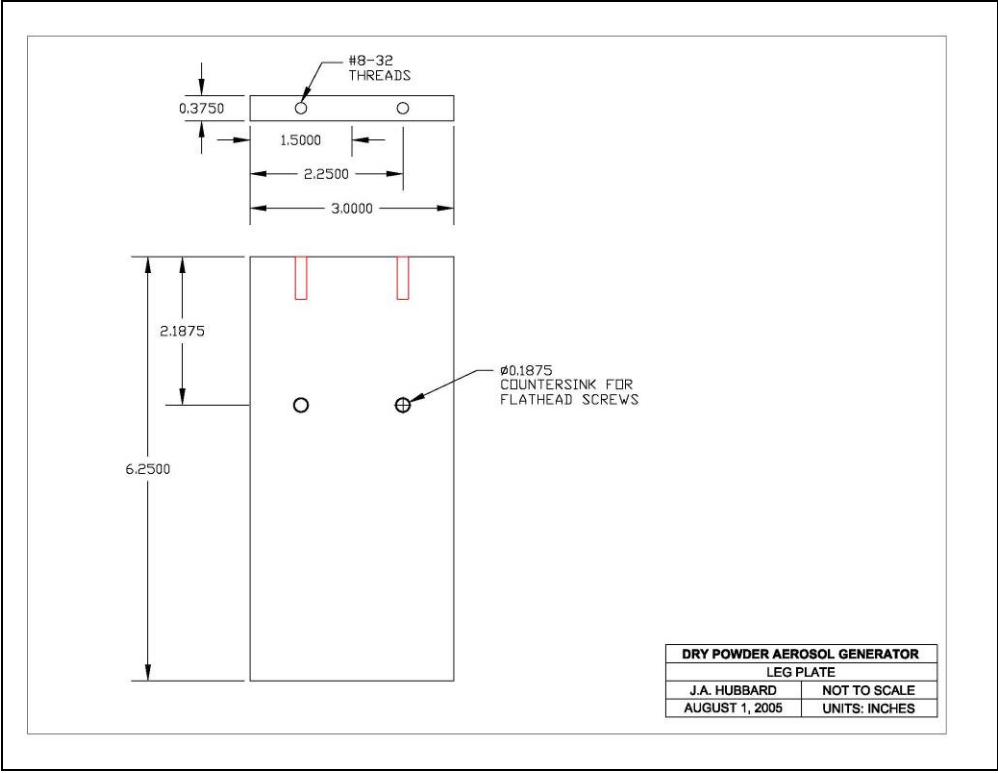


Figure A. 5: Aerosol Generator Leg Plate

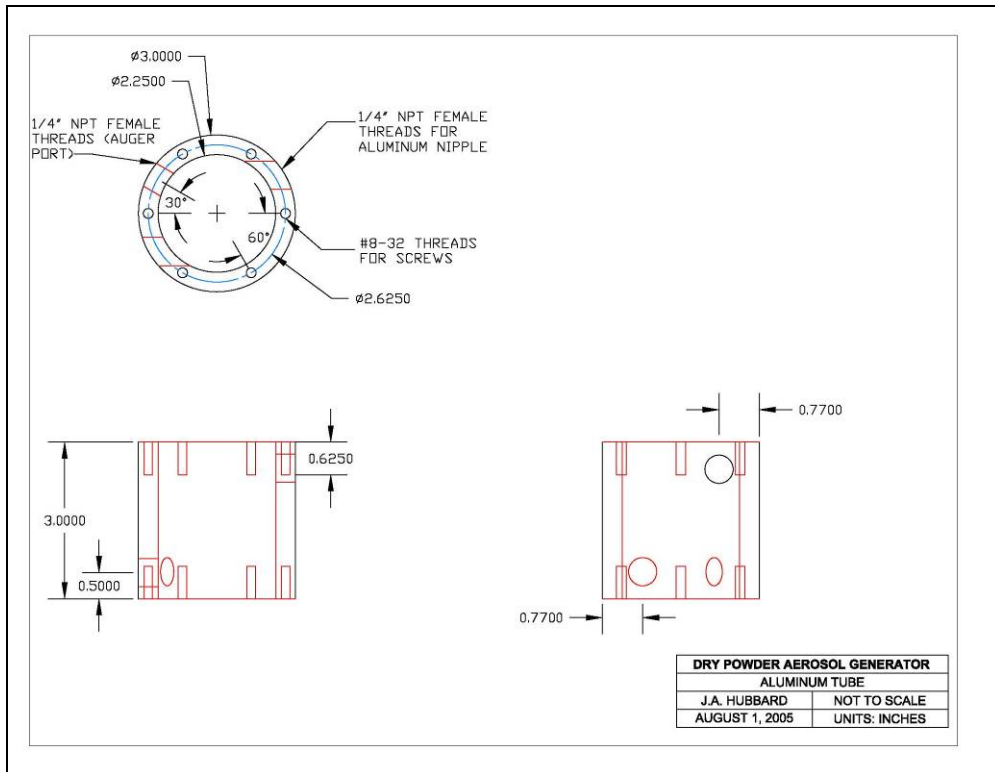


Figure A. 6: Aerosol Generator Aluminum Tube

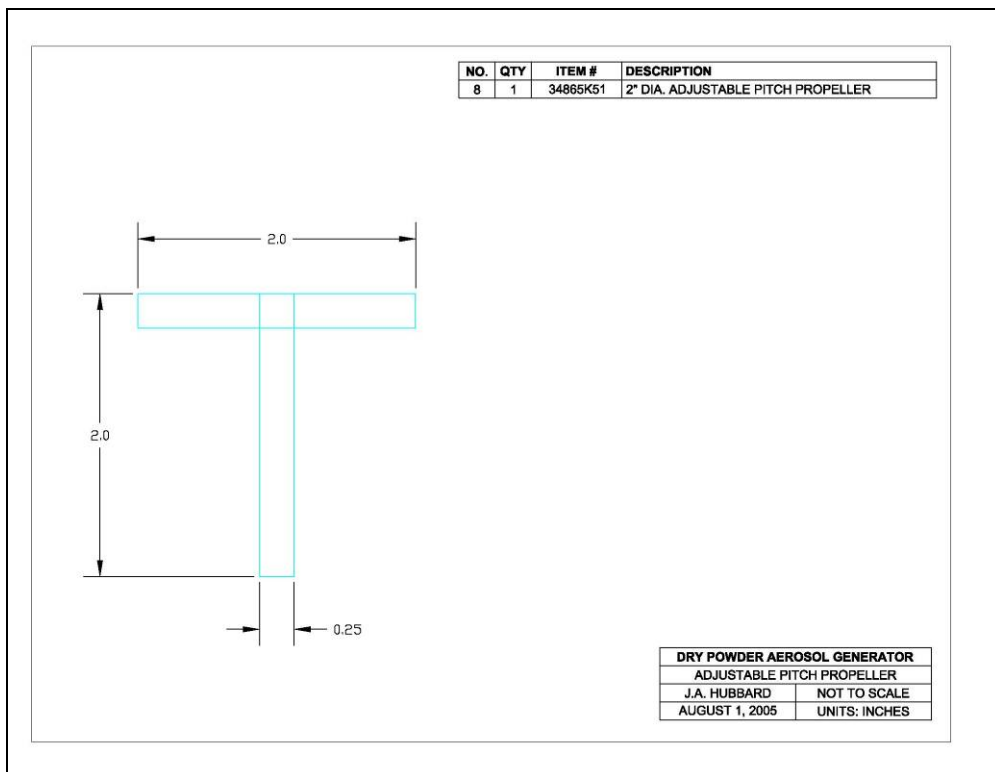


Figure A. 7: Aerosol Generator Propeller

APPENDIX B: PIV CONTOUR PLOTS

Velocity

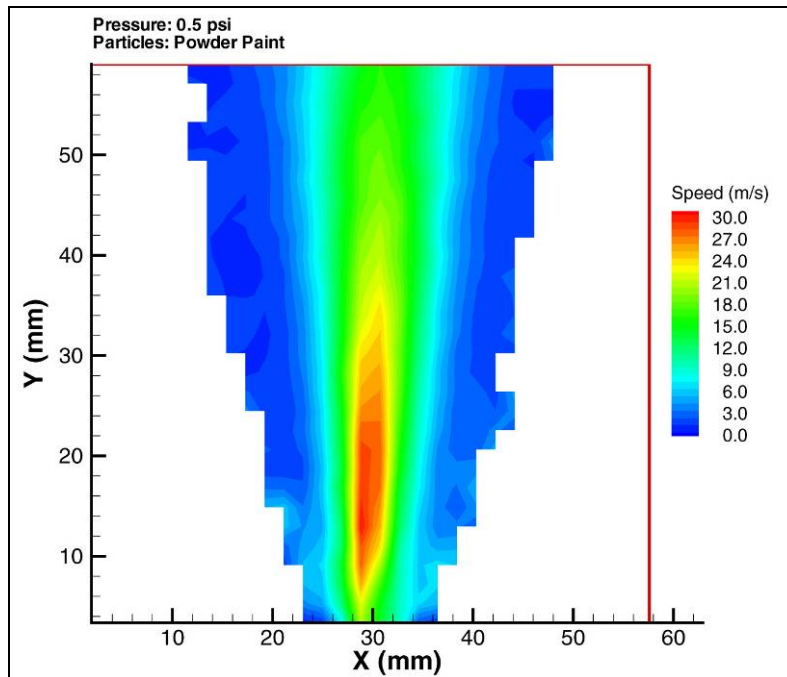


Figure B. 1: PIV Velocity Plot for Abrupt Orifice 0.5 psi

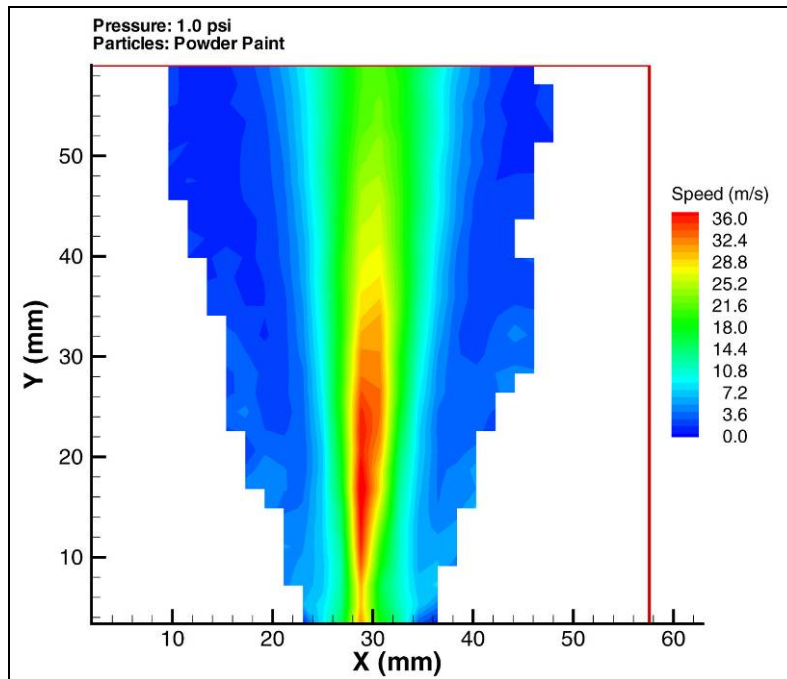


Figure B. 2: PIV Velocity Plot for Abrupt Orifice 1.0 psi

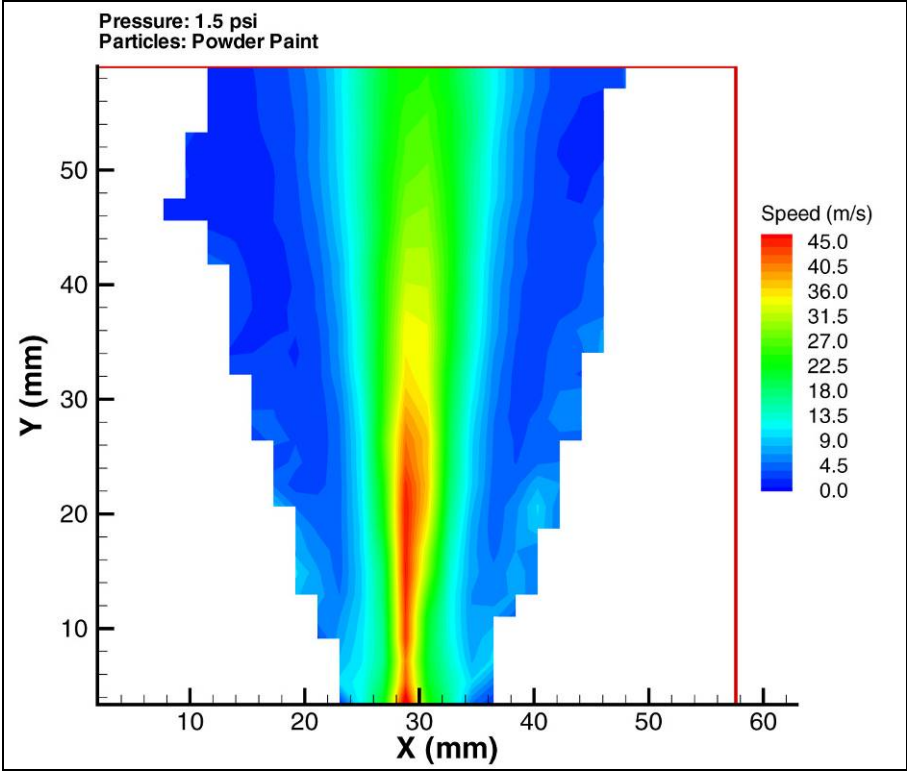


Figure B. 3: PIV Velocity Plot for Abrupt Orifice 1.5 psi

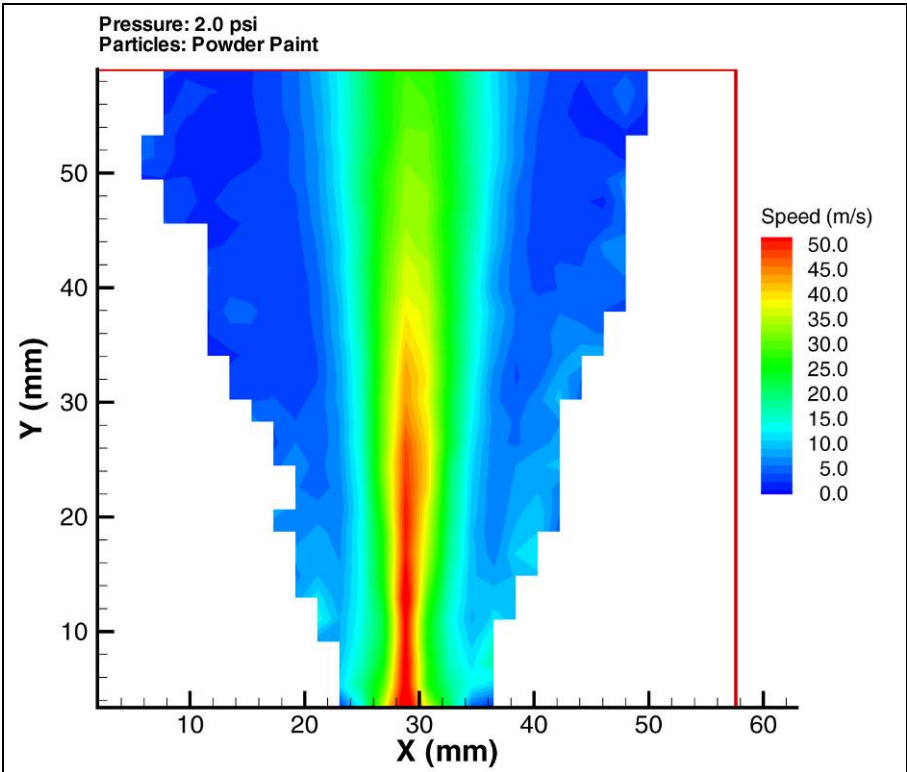


Figure B. 4: PIV Velocity Plot for Abrupt Orifice 2.0 psi

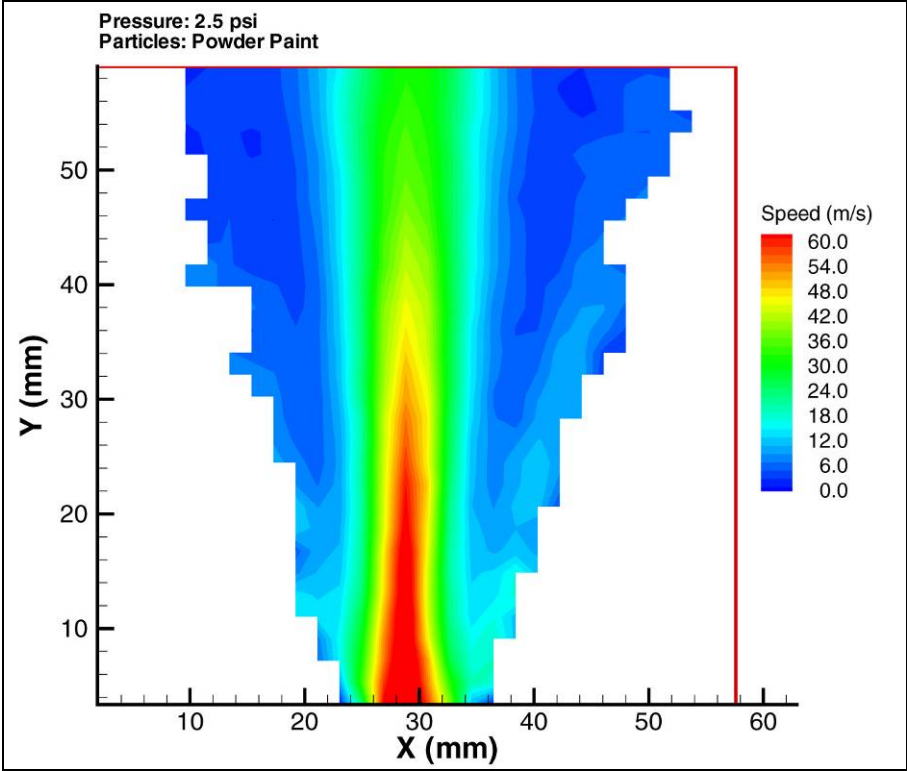


Figure B. 5: PIV Velocity Plot for Abrupt Orifice 2.5 psi

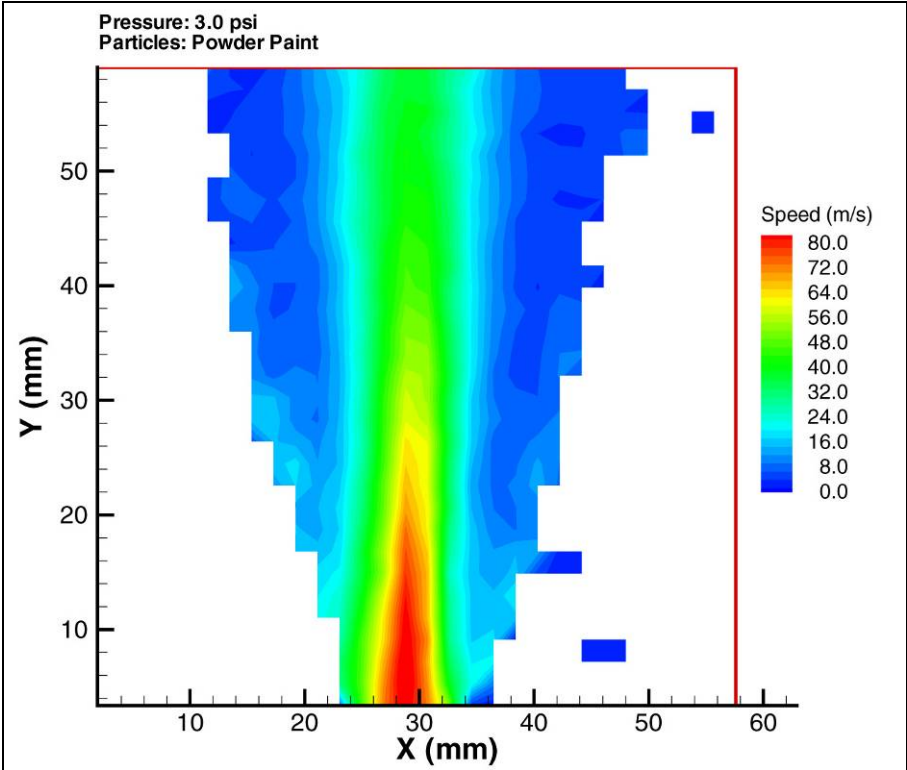


Figure B. 6: PIV Velocity Plot for Abrupt Orifice 3.0 psi

Shear Stress

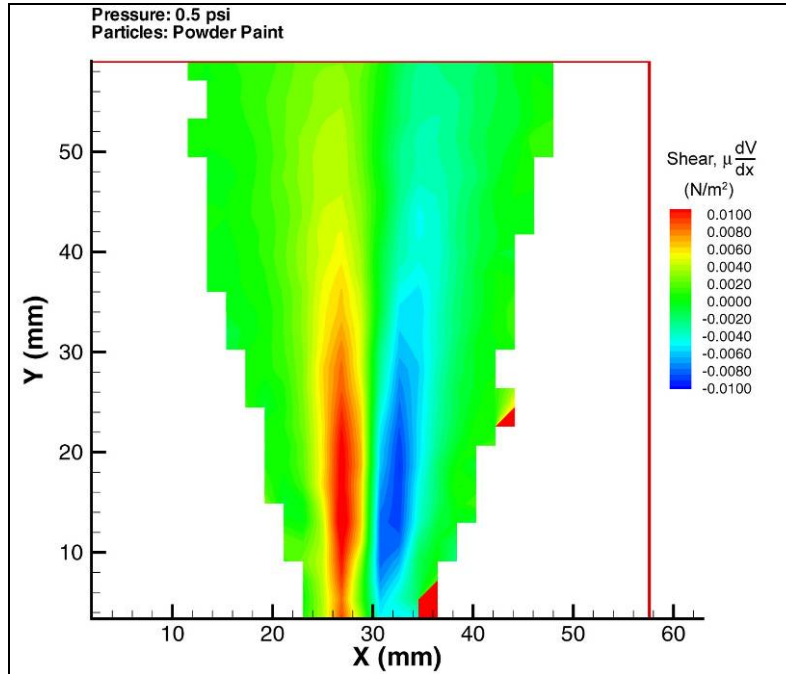


Figure B. 7: PIV Shear Stress Plot for Abrupt Orifice 0.5 psi

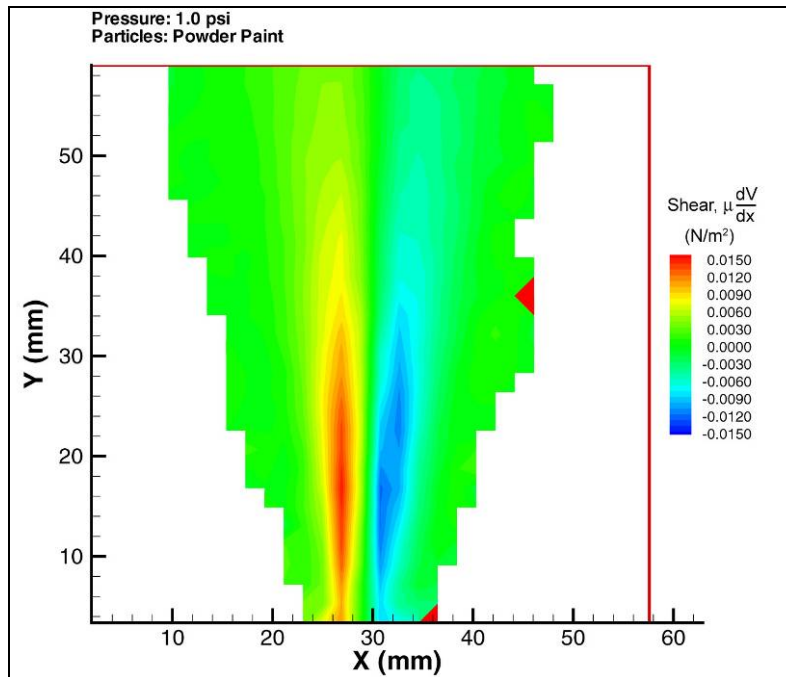


Figure B. 8: PIV Shear Stress Plot for Abrupt Orifice 1.0 psi

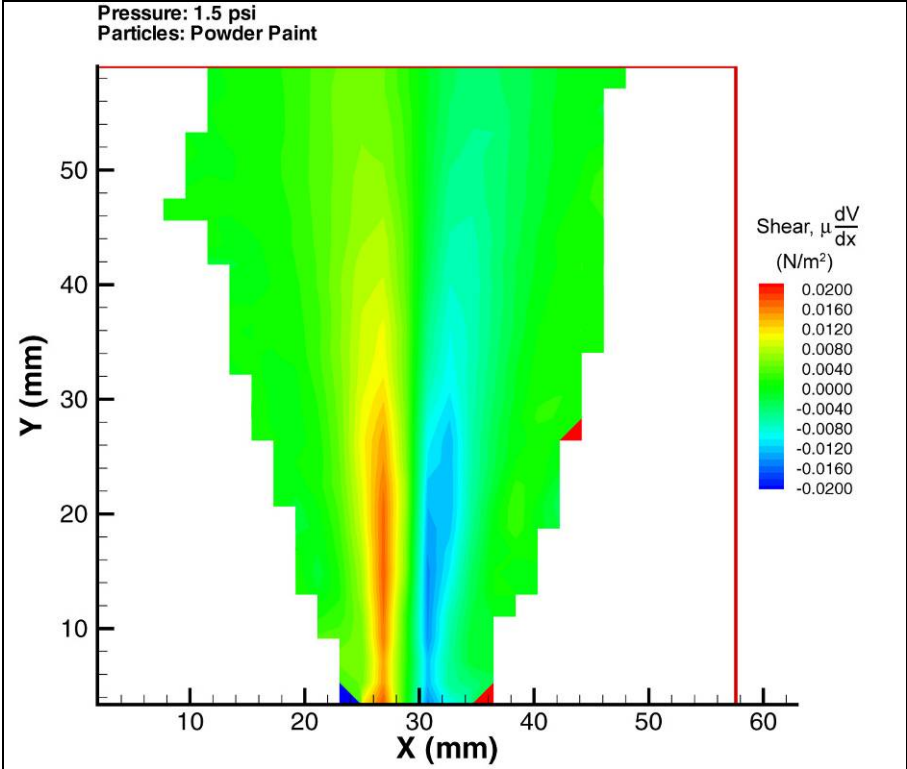


Figure B. 9: PIV Shear Stress Plot for Abrupt Orifice 1.5 psi

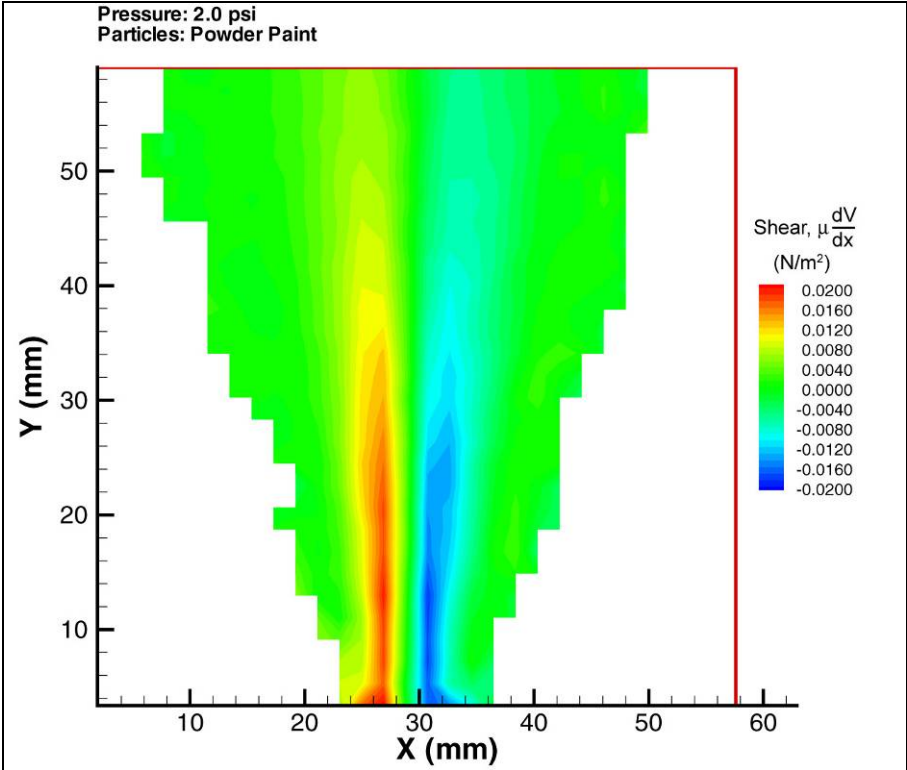


Figure B. 10: PIV Shear Stress Plot for Abrupt Orifice 2.0 psi

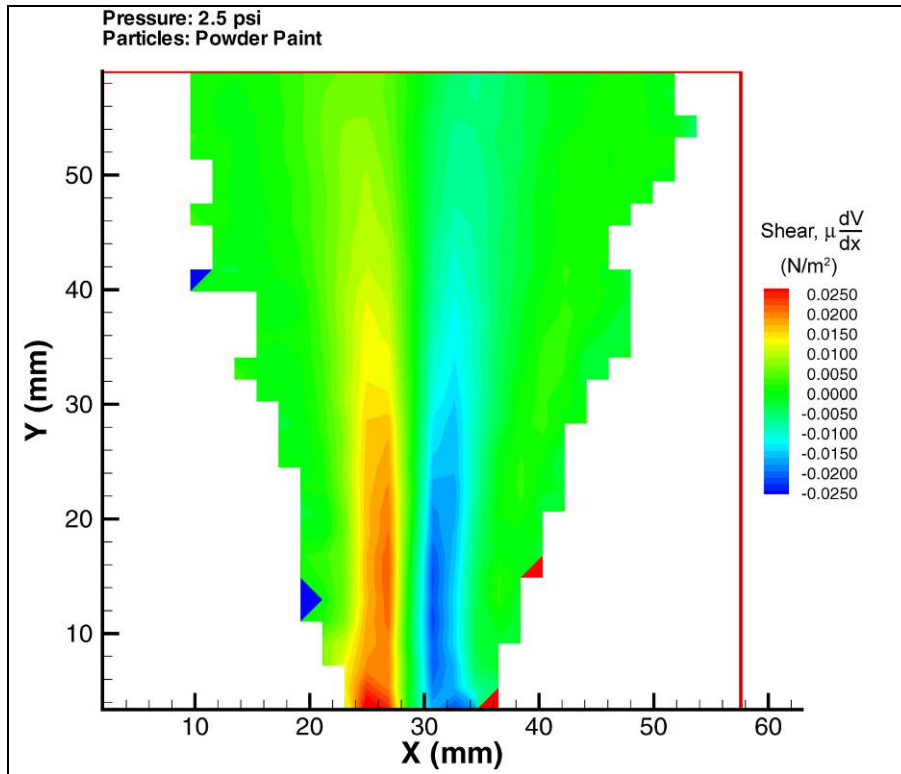


Figure B. 11: PIV Shear Stress Plot for Abrupt Orifice 2.5 psi

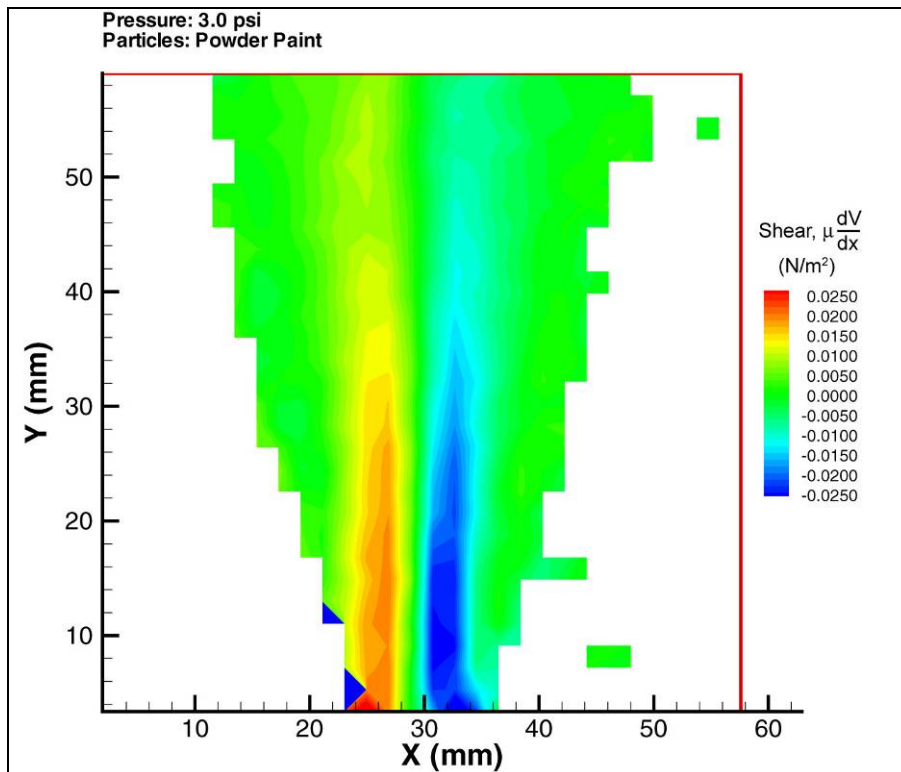


Figure B. 12: PIV Shear Stress Plot for Abrupt Orifice 3.0 psi

Turbulent Kinetic Energy

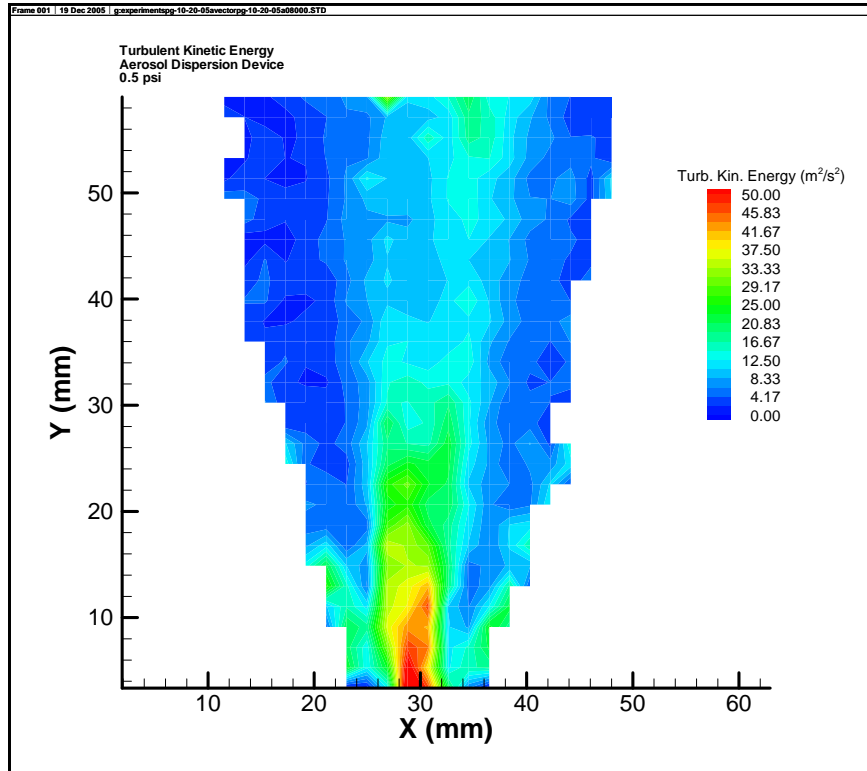


Figure B. 13: PIV Turbulent Kinetic Energy Plot for Abrupt Orifice 0.5 psi

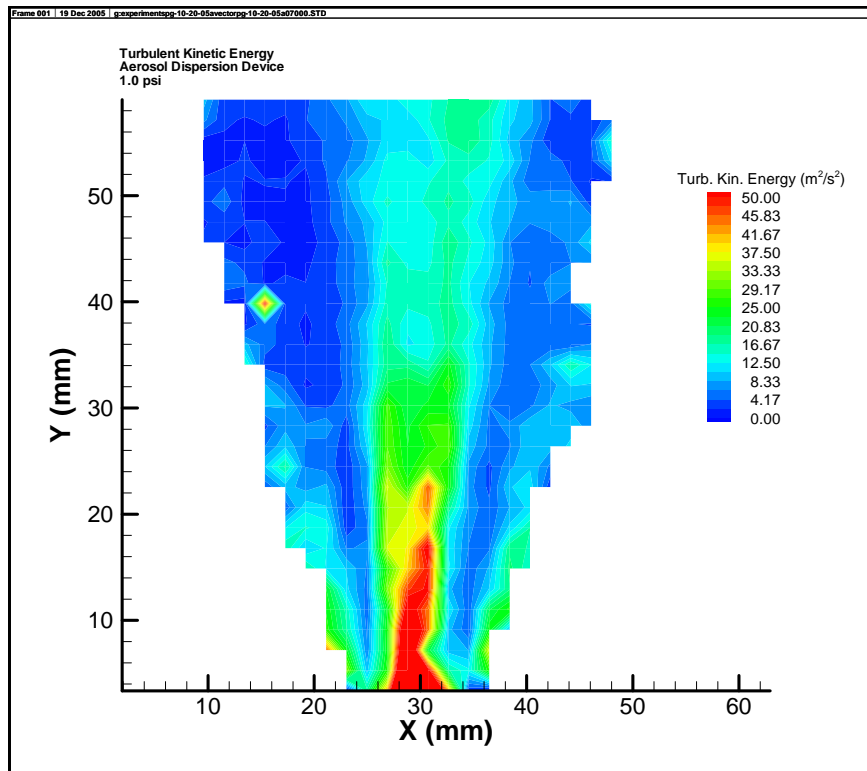


Figure B. 14: PIV Turbulent Kinetic Energy Plot for Abrupt Orifice 1.0 psi

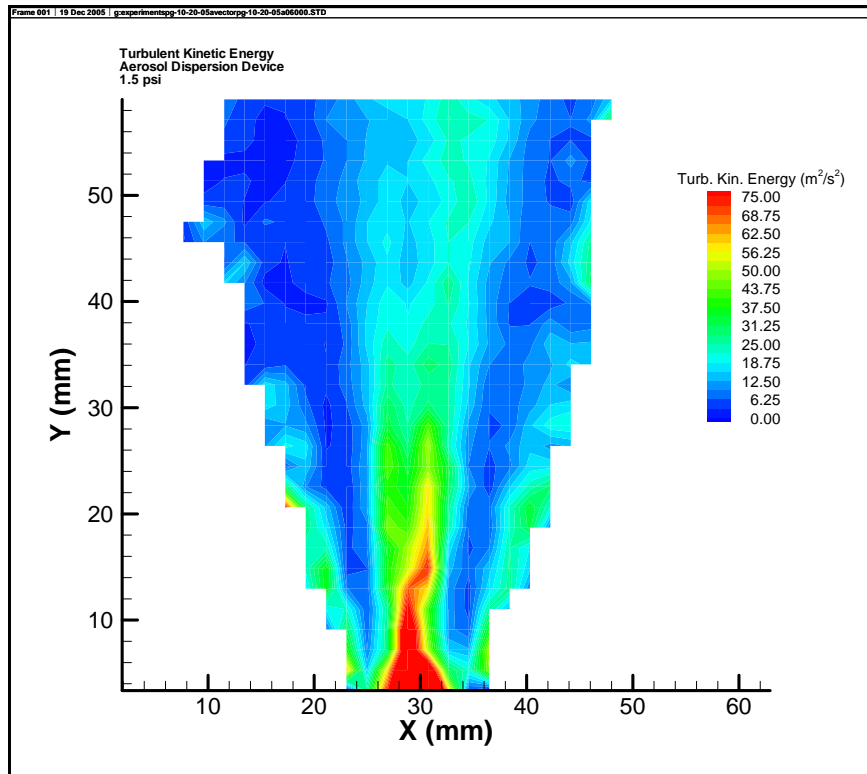


Figure B. 15: PIV Turbulent Kinetic Energy Plot for Abrupt Orifice 1.5 psi

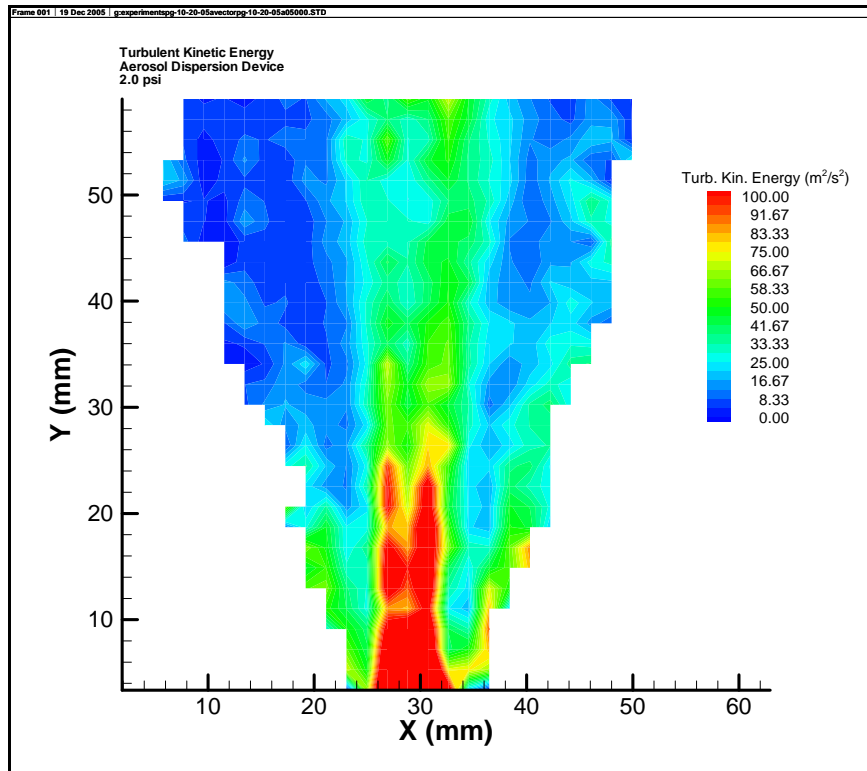


Figure B. 16: PIV Turbulent Kinetic Energy Plot for Abrupt Orifice 2.0 psi

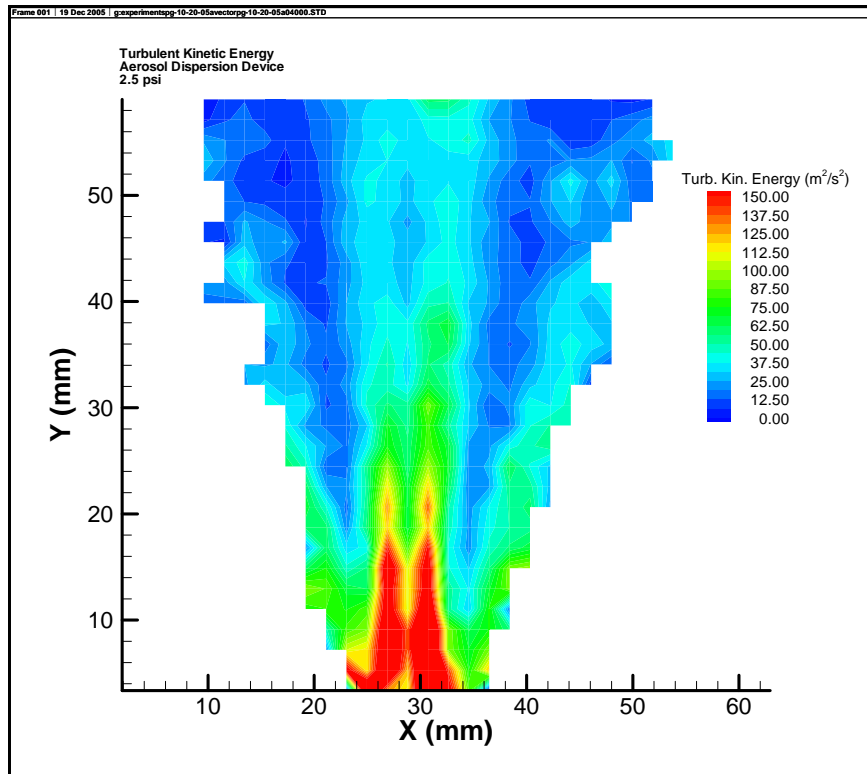


Figure B. 17: PIV Turbulent Kinetic Energy Plot for Abrupt Orifice 2.5 psi

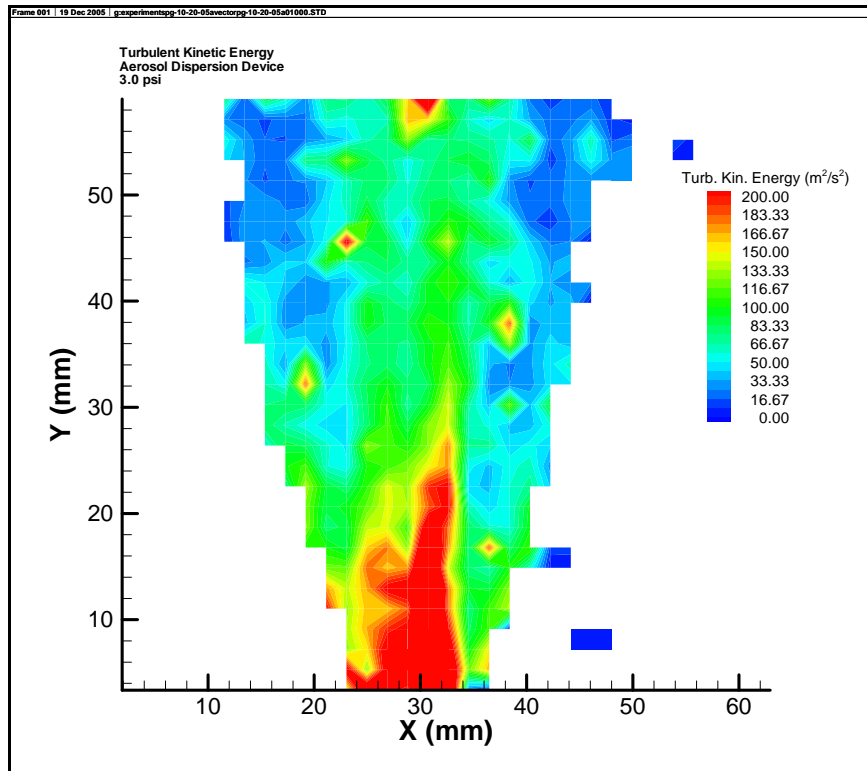


Figure B. 18: PIV Turbulent Kinetic Energy Plot for Abrupt Orifice 3.0 psi

APPENDIX C: THEORETICAL STRESS AND FORCE CALCULATIONS

11.4.1: Stresses Within A Spherical Particle In Uniform Flow

Max'm Velocities Taken from Figure 7.2

$$u := \begin{pmatrix} 75.3 \\ 151.3 \\ 75.3 \end{pmatrix} \frac{\text{m}}{\text{s}}$$

Size of MgO Particle (assumed spherical)

$$d := 0.5 \cdot 10^{-6} \text{ m}$$

Equation 4.1

$$\sigma := \frac{3 \cdot \mu \cdot u}{d}$$
$$\sigma = \begin{pmatrix} 8.178 \times 10^3 \\ 1.643 \times 10^4 \\ 8.178 \times 10^3 \end{pmatrix} \text{ Pa}$$

11.4.2: Stresses Within A Spherical Particle In Shear Flow

$$\mu := 1.81 \cdot 10^{-5} \frac{\text{N} \cdot \text{s}}{\text{m}^2}$$

Max'm Strain Rates Taken from Figure 7.8

$$\gamma := \begin{pmatrix} 1.2 \cdot 10^5 \\ 1.5 \cdot 10^5 \\ 1.4 \cdot 10^5 \end{pmatrix} \frac{1}{\text{s}}$$

Equation 4.2

$$\sigma := 5 \cdot \mu \cdot \gamma$$
$$\sigma = \begin{pmatrix} 10.86 \\ 13.575 \\ 12.67 \end{pmatrix} \text{ Pa}$$

Equation 4.3

$$\tau := 8.5 \cdot \mu \cdot \gamma$$

$$\tau = \begin{pmatrix} 18.462 \\ 23.078 \\ 21.539 \end{pmatrix} \text{ Pa}$$

11.4.3: Stress in a Single Spherical Particle in Accelerating Flow (Newton's Second Law)

Assume Solid Spherical Particle

$$\rho := 3200 \frac{\text{kg}}{\text{m}^3}$$

$$\text{mass} := \frac{\pi \cdot \rho \cdot \text{dpb}^3}{6}$$

$$\text{mass} = 2.094 \times 10^{-16} \text{ kg}$$

Accelerations taken from Figure 7.4

$$a := \begin{pmatrix} 6.6 \cdot 10^6 \\ 10.5 \cdot 10^6 \\ 1.15 \cdot 10^6 \end{pmatrix} \frac{\text{m}}{\text{s}^2}$$

$$F := \text{mass} \cdot a$$

$$F = \begin{pmatrix} 1.382 \times 10^{-9} \\ 2.199 \times 10^{-9} \\ 2.409 \times 10^{-10} \end{pmatrix} \text{ N}$$

Theoretical area acted on by force

$$A := \frac{\pi}{4} \cdot \text{dpb}^2$$

$$A = 1.963 \times 10^{-13} \text{ m}^2$$

$$\sigma := \frac{F}{A}$$

$$\sigma = \begin{pmatrix} 7.04 \times 10^3 \\ 1.12 \times 10^4 \\ 1.227 \times 10^3 \end{pmatrix} \text{ Pa}$$

11.4.4: Stresses within a Spherical Particle in Turbulent Flow

From Figure 7.9

$$\varepsilon := \begin{pmatrix} 3 \cdot 10^6 \\ 7 \cdot 10^6 \\ 5 \cdot 10^6 \end{pmatrix} \frac{\text{m}^2}{\text{s}^3}$$

Constants

$$v := 1.5 \cdot 10^{-5} \frac{\text{m}^2}{\text{s}}$$

$$\rho_f := 1.2 \frac{\text{kg}}{\text{m}^3}$$

$$d_{pb} := 0.5 \cdot 10^{-6} \text{ m}$$

Equation 4.10

$$\tau := \frac{\rho_f \cdot \varepsilon^{\frac{2}{3}}}{10} \cdot d_{pb}^{\frac{2}{3}}$$

$$\tau = \begin{pmatrix} 0.157 \\ 0.277 \\ 0.221 \end{pmatrix} \text{ Pa}$$

Equation 4.11

$$\tau := 3.1 \cdot \rho_f \cdot \sqrt{\varepsilon \cdot v}$$

$$\tau = \begin{pmatrix} 24.955 \\ 38.119 \\ 32.216 \end{pmatrix} \text{ Pa}$$

Equation 4.12

$$\sigma := \frac{10.8 \rho_f \sqrt{\varepsilon \cdot v}}{c_1^3}$$

$$\sigma = \begin{pmatrix} 86.938 \\ 132.8 \\ 112.237 \end{pmatrix} \text{ Pa}$$

11.5.1: Stresses Within an Aggregate in Uniform Flow

Max'm Velocities taken from Figure 7.2

$$u = \begin{pmatrix} 75.3 \\ 151.3 \\ 75.3 \end{pmatrix} \frac{\text{m}}{\text{s}}$$

$$dpb := 0.5 \cdot 10^{-6} \text{ m}$$

$$dpa := 0.25 \cdot 10^{-6} \text{ m}$$

Equation 4.5

$$F := 3 \cdot \pi \cdot u \cdot \mu \cdot dpa \cdot dpb \cdot \frac{(dpb - dpa)}{dpa^2 - dpa \cdot dpb + dpb^2}$$

$$F = \begin{pmatrix} 2.141 \times 10^{-9} \\ 4.302 \times 10^{-9} \\ 2.141 \times 10^{-9} \end{pmatrix} \text{ N}$$

Equation 4.6

$$\tau := \frac{4 \cdot F}{\pi \cdot (c1 \cdot dpa)^2}$$
$$\tau = \begin{pmatrix} 4.361 \times 10^4 \\ 8.763 \times 10^4 \\ 4.361 \times 10^4 \end{pmatrix} \text{ Pa}$$

Equation 4.7

$$\sigma := \frac{16 \cdot F}{\pi \cdot c1 \cdot (c1 \cdot dpa)^2}$$
$$\sigma = \begin{pmatrix} 1.745 \times 10^5 \\ 3.505 \times 10^5 \\ 1.745 \times 10^5 \end{pmatrix} \text{ Pa}$$

11.5.2: Stresses Within an Aggregate in Simple Shear Flow

Constant that gives minimum stress

$$c1 := 1$$

Equation 4.8

$$\sigma := \frac{93 \cdot \mu \cdot \gamma}{\pi \cdot c1^3}$$

$$\sigma = \begin{pmatrix} 64.297 \\ 80.372 \\ 75.014 \end{pmatrix} \text{ Pa}$$

Equation 4.7

$$\sigma := \frac{16 \cdot F}{\pi \cdot c1 \cdot (c1 \cdot dpa)^2}$$

$$\sigma = \begin{pmatrix} 1.745 \times 10^5 \\ 3.505 \times 10^5 \\ 1.745 \times 10^5 \end{pmatrix} \text{ Pa}$$

11.6: Intermolecular Surface Energies and Forces

$$D := 2.1 \cdot 10^{-10} \text{ m}$$

$$N := 5.35 \cdot 10^{28} \frac{1}{\text{m}^3}$$

$$C := 116 \cdot 10^{-79} \text{ J} \cdot \text{m}^6$$

$$d := 0.5 \cdot 10^{-6} \text{ m}$$

$$R := \frac{d}{2}$$

$$R = 2.5 \times 10^{-7} \text{ m}$$

11.6.2.1: Spherical Particle Interacting with an Infinite Plane

Equation 3.7: Energy of interaction for a sphere of Radius R with an infinite planar surface

$$W := \frac{-\pi^2 \cdot C \cdot N^2 \cdot R}{6 \cdot D}$$

$$W = -6.502 \times 10^{-17} \text{ J}$$

11.6.2.2: Planar area Interacting with an Infinite Plane

Equation 3.8: Energy of interaction for a plane of unit area with an infinite planar surface

$$W_{\text{planes}} := \frac{-\pi \cdot C \cdot N^2}{12 \cdot D^2}$$

$$W_{\text{planes}} = -0.197 \frac{\text{kg}}{\text{s}^2}$$

Area of Interaction for a square plane of dimension d

$$A := d \cdot d$$

$$A = 2.5 \times 10^{-13} \text{ m}^2$$

Energy of Interaction for a plane of dimension d with an infinite planar surface

$$W := W_{\text{planes}} \cdot A$$

$$W = -4.928 \times 10^{-14} \text{ J}$$

11.6.2.3: Derjaguin Approximation for Force between two Spheres

Equation 3.9: Derjaguin Approximation: Force of Interaction between two spheres of unequal radii

$$R1 := 0.25 \cdot 10^{-6} \text{ m}$$

$$R2 := 0.125 \cdot 10^{-6} \text{ m}$$

$$F := 2\pi \cdot \left(\frac{R1 \cdot R2}{R1 + R2} \right) \cdot W_{\text{planes}}$$

$$F = -1.032 \times 10^{-7} \text{ N}$$

Equation 3.10: Force of Interaction between two spheres of equal radii

$$R := 0.25 \cdot 10^{-6} \text{ m}$$

$$F := \pi \cdot R \cdot W_{\text{planes}}$$

$$F = -1.548 \times 10^{-7} \text{ N}$$

Theoretical area of interaction (mid-plane)

$$A := \pi \cdot R^2$$

$$A = 1.963 \times 10^{-13} \text{ m}^2$$

Stress between 2 spheres of equal radius from Derjaguin Approximation and theoretical area of interaction

$$\sigma := \frac{F}{A}$$

$$\sigma = -7.884 \times 10^5 \text{ Pa}$$

11.8: Deaggregation as a Function of Particle Size and Structure

Stresses Within an MgO Aggregate in Uniform Flow

$$u = \begin{pmatrix} 75.3 \\ 151.3 \\ 75.3 \end{pmatrix} \frac{\text{m}}{\text{s}}$$

$$d_{pb} := 0.5 \cdot 10^{-6} \text{ m}$$

$$d_{pa} := 0.55 \cdot 10^{-6} \text{ m}$$

Equation 4.5

$$F := 3 \cdot \pi \cdot u \cdot \mu \cdot dpa \cdot dpb \cdot \frac{(dpb - dpa)}{dpa^2 - dpa \cdot dpb + dpb^2}$$

$$F = \begin{pmatrix} -6.365 \times 10^{-10} \\ -1.279 \times 10^{-9} \\ -6.365 \times 10^{-10} \end{pmatrix} \text{ N}$$

Equation 4.6

$$\tau := \frac{4F}{\pi \cdot (c1 \cdot dpa)^2}$$

$$\tau = \begin{pmatrix} -2.679 \times 10^3 \\ -5.383 \times 10^3 \\ -2.679 \times 10^3 \end{pmatrix} \text{ Pa}$$

Equation 4.7

$$\sigma := \frac{16F}{\pi \cdot c1 \cdot (c1 \cdot dpa)^2}$$

$$\sigma = \begin{pmatrix} -1.072 \times 10^4 \\ -2.153 \times 10^4 \\ -1.072 \times 10^4 \end{pmatrix} \text{ Pa}$$

Stresses Within an MgO Plus Aggregate in Uniform Flow

$$u = \begin{pmatrix} 75.3 \\ 151.3 \\ 75.3 \end{pmatrix} \frac{\text{m}}{\text{s}}$$

$$dpb := 5 \cdot 10^{-9} \text{ m}$$

$$dpa := 5.5 \cdot 10^{-9} \text{ m}$$

Equation 4.5

$$F := 3 \cdot \pi \cdot u \cdot \mu \cdot dpa \cdot dpb \cdot \frac{(dpb - dpa)}{dpa^2 - dpa \cdot dpb + dpb^2}$$

$$F = \begin{pmatrix} -6.365 \times 10^{-12} \\ -1.279 \times 10^{-11} \\ -6.365 \times 10^{-12} \end{pmatrix} \text{ N}$$

Equation 4.6

$$\tau := \frac{4 \cdot F}{\pi \cdot (c1 \cdot dpa)^2}$$

$$\tau = \begin{pmatrix} -2.679 \times 10^5 \\ -5.383 \times 10^5 \\ -2.679 \times 10^5 \end{pmatrix} \text{ Pa}$$

Equation 4.7

$$\sigma := \frac{16 \cdot F}{\pi \cdot c1 \cdot (c1 \cdot dpa)^2}$$

$$\sigma = \begin{pmatrix} -1.072 \times 10^6 \\ -2.153 \times 10^6 \\ -1.072 \times 10^6 \end{pmatrix} \text{ Pa}$$

Stresses Within a MgO Spherical Particle Due to Uniform Flow

Max'm Velocities Taken from Figure 7.2

$$u := \begin{pmatrix} 75.3 \\ 151.3 \\ 75.3 \end{pmatrix} \frac{\text{m}}{\text{s}}$$

Size of MgO Particle (assumed spherical)

$$d := 0.5 \cdot 10^{-6} \text{ m}$$

From Equation 4.3

$$\sigma := \frac{3 \cdot \mu \cdot u}{d}$$

$$\sigma = \begin{pmatrix} 8.178 \times 10^3 \\ 1.643 \times 10^4 \\ 8.178 \times 10^3 \end{pmatrix} \text{ Pa}$$

Stresses Within A MgO Plus Spherical Particle Due to Uniform Flow

Max'm Velocities Taken from Figure 7.2

$$u := \begin{pmatrix} 75.3 \\ 151.3 \\ 75.3 \end{pmatrix} \frac{\text{m}}{\text{s}}$$

Size of MgO Particle (assumed spherical)

$$d := 5 \cdot 10^{-9} \text{ m}$$

From Equation 4.3

$$\sigma := \frac{3 \cdot \mu \cdot u}{d}$$
$$\sigma = \begin{pmatrix} 8.178 \times 10^5 \\ 1.643 \times 10^6 \\ 8.178 \times 10^5 \end{pmatrix} \text{ Pa}$$

Stress in Accelerating MgO Particle from Newton's Second Law

Assume Solid Spherical Particle

$$\text{dpb} := 0.5 \cdot 10^{-6} \text{ m}$$

$$\rho := 3200 \frac{\text{kg}}{\text{m}^3}$$

$$\text{mass} := \frac{\pi \cdot \rho \cdot \text{dpb}^3}{6}$$

$$\text{mass} = 2.094 \times 10^{-16} \text{ kg}$$

$$a := \begin{pmatrix} 6.6 \cdot 10^6 \\ 10.5 \cdot 10^6 \\ 1.15 \cdot 10^6 \end{pmatrix} \frac{\text{m}}{\text{s}^2}$$

$$F := \text{mass} \cdot a$$

$$F = \begin{pmatrix} 1.382 \times 10^{-9} \\ 2.199 \times 10^{-9} \\ 2.409 \times 10^{-10} \end{pmatrix} \text{ N}$$

Area acted on by force

$$A := \frac{\pi}{4} \cdot \text{dpb}^2$$

$$A = 1.963 \times 10^{-13} \text{ m}^2$$

$$\sigma := \frac{F}{A}$$

$$\sigma = \begin{pmatrix} 7.04 \times 10^3 \\ 1.12 \times 10^4 \\ 1.227 \times 10^3 \end{pmatrix} \text{ Pa}$$

Stress in Accelerating MgO Plus Particle from Newton's Second Law

Assume Solid Spherical Particle

$$\text{dpb} := 5 \cdot 10^{-9} \text{ m}$$

$$\rho := 3200 \frac{\text{kg}}{\text{m}^3}$$

$$\text{mass} := \frac{\pi \cdot \rho \cdot \text{d}^3 \text{pb}^3}{6}$$

$$\text{mass} = 2.094 \times 10^{-22} \text{kg}$$

$$\mathbf{a} := \begin{pmatrix} 6.6 \cdot 10^6 \\ 10.5 \cdot 10^6 \\ 1.15 \cdot 10^6 \end{pmatrix} \frac{\text{m}}{\text{s}^2}$$

$$\mathbf{F} := \text{mass} \cdot \mathbf{a}$$

$$\mathbf{F} = \begin{pmatrix} 1.382 \times 10^{-15} \\ 2.199 \times 10^{-15} \\ 2.409 \times 10^{-16} \end{pmatrix} \text{N}$$

Area acted on by force

$$A := \frac{\pi}{4} \cdot \text{d}^2 \text{pb}^2$$

$$A = 1.963 \times 10^{-17} \text{m}^2$$

$$\sigma := \frac{\mathbf{F}}{A}$$

$$\sigma = \begin{pmatrix} 70.4 \\ 112 \\ 12.267 \end{pmatrix} \text{Pa}$$